DISTORTION REDUCTION AND SIGNAL ESTIMATION IN DOPPLER RADAR PHYSIOLOGICAL MONITORING SYSTEMS

DOCTOR OF PHILOSOPHY

IN
ELECTRICAL ENGINEERING

By
Ehsan Yavari

Dissertation Committee:

Olga Boric-Lubecke, Chairperson

Victor Lubecke

Aaron Ohta

Yi Zuo

Thomas Ernst

December 2015

ABSTRACT

Feasibility of microwave Doppler radar for non-contact physiological monitoring and detection is explored in this dissertation. Although there was significant progress during the last decade in this technology, there are still numerous challenges to be addressed. In this work several sources of signal distortion are investigated. Contributions to the field of electrical engineering include novel hardware and software techniques to overcome distortions and improve signal estimation in wireless vital sign monitoring. Channel imbalance in quadrature receivers is one of the distortion sources that has been systematically investigated, theoretically and experimentally. It has been demonstrated that imbalance can introduce error in displacement estimation, radar cross section, and even rate measurements. Innovative hardware approaches, including packet radar and pulse low-IF receiver architectures, were proposed to resolve AC coupling issues, channel imbalance, and position sensitivity. Signal estimation for single and multiple subject detection was explored. True human presence estimation is demonstrated with Doppler radar occupancy sensors based on heart and respiration rates to overcome the limitations of common occupancy sensors. Estimating direction of arrival in a single input multiple output system is explored for multiple subject detection. These new approaches may bring Doppler radar physiological monitoring devices one step closer for reliable system performance at low power and low cost.

Table of Contents

List of Figures

1. INTRODUCTION

Vital signs carry crucial information about a patient's health status. Abnormal respiratory rates and changes in respiratory rate are a broad indicator of major physiological instability, and in many cases, respiratory rate is one of the earliest indicators of this instability [1]. Furthermore, monitoring heart rate and heart rate variability (HRV), which refers to beat-to-beat alternation in heart rate, reflects the manner in which the cardiovascular system responds to demands, stress, and illness [2].

In 2010, cardiovascular, lung, and blood diseases accounted for 1,017,000 deaths and 41% of all deaths in the United States. The estimated economic cost in 2009 for these diseases was $424 billion, 23% of the total economic cost of illness, injuries, and death. Of all diseases, heart disease is the leading cause of death. Chronic lower respiratory diseases (CLRD), which include COPD and asthma, ranks third (behind cancer). Cardiovascular and lung diseases account for 3 of the 4 leading causes of death. Hypertension, asthma, CHD, and COPD are especially prevalent and account for substantial morbidity in Americans [3].

Measuring physiological signals is of significance importance for many diagnosis applications. Non-contact detection and monitoring of cardiopulmonary activity can provide substantial information and a tool for continuous monitoring of patients. It can

have many applications such as sleep monitoring [4, 5], home healthcare [6, 7], baby monitoring [8], post-surgery monitoring, tumor tracking [9], and search and rescue application [10]. In some cases, using wired electrodes is impossible, such as for burn injuries and sleep monitoring. The monitoring device itself can be obtrusive and can change the patient's behavior. Another promising application is occupancy detection [11, 12]. Since vital signs are monitored, true human presence can be detected by acquiring respiratory and cardiac information.

Microwave Doppler Radar can provide a promising tool for non-contact physiological monitoring. It has been used for measuring respiration signals in 1975 and in 1979 for heart measurement [13, 14]. First-time measurements were done with bulky, heavy, and expensive waveguide components.

During the past decades, research effort has been focused on lowering the cost, power, size, and weight, while increasing detection range and accuracy. There have been significant advancements in the hardware development of Doppler radar sensors from bench-top systems to CMOS/BiCOMS radar-on-chips. Although the hardware technologies are essential in realizing high detection sensors, advanced signal processing methods are equally important to solve various challenges. Issues such as motion artifacts, channel imbalance, DC offset, coupling issues, frequency band limitations, multiple reflections, and noise limit the ability of the sensor [15-20].

This work's focus is to develop new software and hardware solutions to address some of the challenges that Doppler radar physiological monitoring suffers from and bound practical applications. In particular, feasibility of a novel application of Doppler as an occupancy sensor is explored to overcome the current limitations of common occupancy

sensors. A sensor is developed to recognize level of activity, isolate individuals, acquire the direction of arrival, and its performance compared to conventional sensors. One of the main sources of distortion in quadrature receivers is channel imbalance. The effects on rate and displacement measurements are systematically studied and discussed. Novel System-on-Chip packet radar is proposed as a means of respiratory detection with emphasis on power saving. Coupling and DC offset issues are addressed. New advanced signal processing techniques are explored to enhance the performance of the receiver and improve vital sign detection and estimation. A novel single-channel pulse low-IF receiver is proposed that has the advantages of a quadrature receiver, better noise performance, and simplicity of a single-channel receiver.

Small motions induced by the heart and lungs on the chest surface can be measured by a Doppler radar physiological sensor aimed at the human subject [10, 13]. Continuous-wave, pulse, and packet radars are employed to transmit microwave signals toward the human body. The back scattered signal is captured by the receiver and compared with the transmitted or reference signal. The changes in the phase of the received signal are an indicator of physiological motion of the subject.

This chapter covers the basics of Doppler radar. Different radar topologies and essential equations governing the radar systems are discussed. Radar applications are introduced and an overview of the dissertation is given. More detailed explanations of Doppler radar for health-monitoring purposes are given in chapter 2.

1.1 Radar Fundamentals

Radar is an acronym for Radio Detection and Ranging. It describes a system that

transmits electromagnetic signals and senses the back-scattered signals from the target, thereby acquiring information such as velocity, altitude, direction, range, and size of the object, such as ships, aircrafts, and motor vehicles. The round-trip time delay between transmitted and received echo specifies the range or distance of the target. The Doppler frequency shift indicates the velocity or speed of the object, and the power of the reflected signal represent size, shape, and composition of the object.

A simple radar block diagram is shown in Fig. 1.1. It consists of a transmitter and a receiver. The transmitter section generates an intended radio frequency (RF) signal and the radar antenna illuminates the target with the generated microwave signal. Transmit power is dependent upon applications and required range. The reflected signal is captured by the receiving antenna and down-converted from transmission frequency to an intermediate or baseband frequency. Then the signal is filtered, amplified, and conditioned for digitization or display. Signal-processing algorithms are often used to extract velocity and range information.

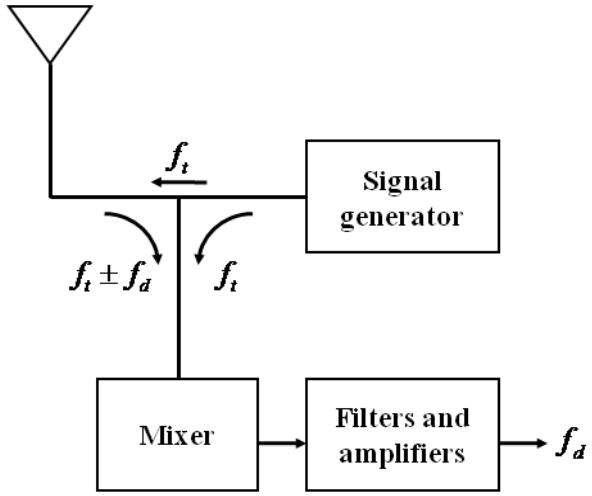

Fig. 1.1 CW Doppler radar block diagram

1.1.1 Continuous-Wave, Frequency-modulated Continuous-Wave, and Pulse Radar

Different radar topologies are used for acquiring the desired information. Radars are usually named after the modulation technique which is used for the transmit signal. A simple configuration is pure continuous-wave (CW) system that can sense target motion based on the Doppler shift of the received signal. A CW radar constantly sends and receives a narrow bandwidth signal. Due to its narrow bandwidth, the design of filters and amplifiers are simpler, as well as the demodulation and signal processing. Although CW radar can measure velocity without any ambiguity, the main limitation is that pure CW radars cannot measure range.

Since CW radars transmit and receive at all times, leakage from transmitter to receiver either through the coupling or the antennas can produce a large signal in the receiver which is not reflected by the target. Furthermore, reflections from stationary targets (clutter) can add to the signal at the transmitted frequency. These unwanted signals produce DC offset and low-frequency noise in the receiver, which degrades the signal-to-noise ratio (SNR), saturates the baseband amplifiers, and reduces the dynamic range of the receiver.

In order to detect the target range with CW radar, the signal should have a type of timing marker to be able to measure the round-trip delay time. One solution to the range issue is using frequency-modulated continuous-wave (FMCW) radar. It can detect both range and velocity of the target [21]. The frequency modulation is usually triangular for FMCW systems, and frequency varies gradually. Altimeters and Doppler navigation devices use this type of radar.

On the other hand, pulse radar switches between transmitting and receiving, and the

signal has a wider bandwidth than CW radars. A pulse radar system usually transmits narrow pulses with a large peak power at a constant pulse-repetition frequency and analyzes the time-delayed received echoes reflected from target objects. Pulse radar that employs the Doppler shift for detecting moving targets is either an MTI (moving target indication) radar or a pulse Doppler radar [22]. Traditional pulse radar has the advantage of measuring range, in addition to velocity information. In this topology, transmission and reception happen at different times, and this time separation allows the round trip time and range information to be calculated. Fig. 1.2 shows a simple block diagram of a pulse radar system. Pulse modulator turns the transmitter on and off to generate a pulse waveform.

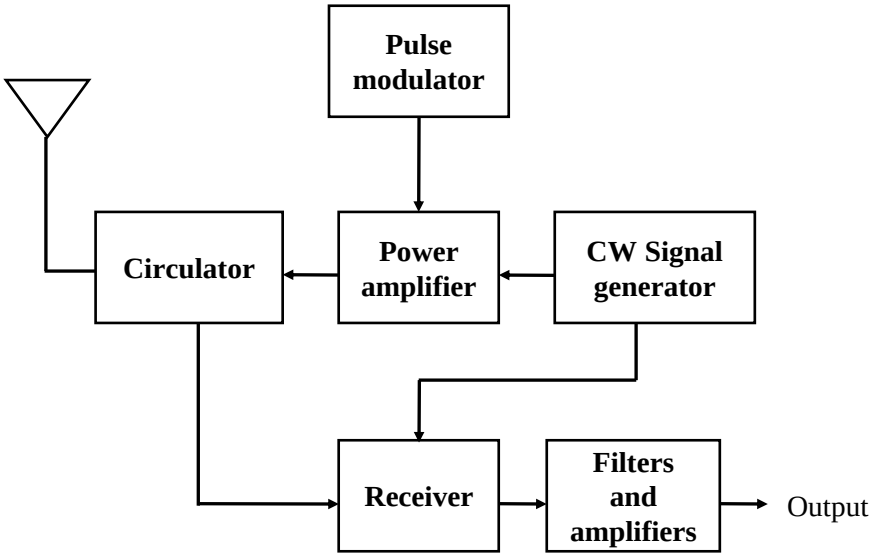

Fig. 1.2 Pulse Doppler radar block diagram

Although modulated continuous-wave systems and pulse radar can measure range in addition to velocity, there are ambiguities in both range and velocity measurements.

1.1.2 Radar Equations

Electromagnetic signals travel at the speed of light, therefore the round-trip time delay between transmission and reception of the pulses can be described by:

$$\tau = 2R/c \tag{1.1}$$

where R is the range of the target, c is the speed of light which is $3 \times 10^8\ m/s$3 x 10^8 m/s, and τ is the round trip travel time [23]. Doppler radar is a category of radars that sense the Doppler shift in the reflected signal in order to provide information about the moving object at further distances. By analyzing how the frequency of the returned signal is shifted, the object's motion can be detected due to relative motion between target and the radar. Doppler frequency shift can be illustrated by the following equation:

$$f_d = -\frac{v}{c} \tag{1.2}$$

where v is the target's speed with respect to the radar in m/s, c is the speed of light in m/s, and f_d is the Doppler frequency shift in Hz. Radar transmission power can be related to physical propagation through space. For a line-of-sight case, reflected power can be related to transmit power using the radar equation:

$$P_r = \frac{P_t G A_e \sigma}{(4\pi)^2 R^4} \tag{1.3}$$

where P_r is the received signal power in Watts, P_t is the transmit power, G is the antenna gain, A_e is the receiving antenna effective aperture, σ is the radar cross section (RCS) of the target, and R is the range to the target. It is interesting to note that the receiving power is related to the inverse fourth power of the distance between the transceiver and the target, and it is due to the round-trip signal travel path toward and from the object. The radar cross section is the property of the scattering object that

represents the magnitude of the echo signal reflected from the target to the radar. It depends upon the target's composition, size, shape, and orientation. Radar cross section can be expressed by the following equation:

$$\sigma = \frac{power\ \ reflected\ \ toward\ \ source\ /\ unit\ \ solid\ \ angle}{incident\ \ power\ \ density\ \ /\ 4\pi} \tag{1.4}$$

1.2 Applications of Radar

Radar has numerous applications in military, civilian, and scientific areas. It has been extensively used for air defense systems, vehicle speed monitoring, air traffic control, and weather forecasting. Military defense has been the major push for new radar technology developments. Military defense radars can detect aircraft and airborne weapons, track their course, position, and speed. Radar has been used for remote sensing to monitor the earth's surface, atmosphere, oceans, and even the moon and other planets. Intrusion detection is another application for security purposes.

It is used in law enforcement to measure the speed of moving vehicles on highways and also in professional sports for measuring the speed of pitched baseballs, runners, or tennis serves. It also received serious attention in the automotive industry for collision avoidance systems [24]. Weather surveillance radar is another application that is used to locate precipitation, calculate its motion, and estimate its type (rain, snow, and hail).

Air traffic control radar have been used to safely control air traffic in the vicinity of airports, and en route from departure to destination airports. It also maps precipitation zones, and airplanes are directed around them [23, 25]. Radar is also used for collision avoidance and navigation of ships and boats. Shore-based radar facilities are used for

monitoring harbors and river traffic.

1.3 Scope of the Dissertation

In addition to air traffic control and weather forecasting, the same principle for detecting frequency or phase shift in a reflected radar signal could be used for sensing small motions induced to the chest surface by lungs and heart. Non-contact vital sign detection can have many potential applications, such as sleep monitoring, healthcare monitoring, and occupancy detection. In this dissertation the focus is directed toward developing new hardware and software techniques to overcome noise and distortion issues, and to make the sensor more practical and feasible for real-life applications.

The first two chapters present the details of radar and Doppler radar theory for physiological monitoring applications. Different radar topologies, applications, receiver architectures, signal conditioning, and demodulation methods are discussed in depth. System trade-offs and performance limitations are presented.

Chapter 3 systematically studies the effects of amplitude and phase imbalance in quadrature receivers. Parametric simulations and experiments are performed to test the effects of amplitude imbalance, phase imbalance, and initial phase on Doppler radar-obtained pattern, displacement, and rate estimation.

In chapter 4, packet radar is explored as an innovative solution to DC offset and coupling distortion, which can limit the performance of the radar. Packet radar is a potential low-power alternative to continuous-wave radar that has the capability to extract physiological signals. New signal processing techniques are developed to tackle with the challenges that are faced in this type of radar.

In chapter 5, pulse low-IF Doppler radar single-channel receiver is introduced which improves signal-to-noise ratio of the receiver and better signal estimation. This architecture can take advantage of a quadrature receiver's benefits without having the complexity and issues of such a receiver.

Chapter 6 presents signal estimation for subject detection based on respiration and heart signals. It gives a thorough background about existing occupancy detection technologies and their limitations. The feasibility of true human presence detection is explored via Doppler radar. A microwave occupancy detector's performance is compared to conventional infrared and ultrasonic sensors. Direction of arrival and multiple subject classification are also investigated.

Chapter 7 provides a summary of the work done in this dissertation, and contributions of this dissertation to the art and science of electrical engineering are outlined. Future work and further possible expansions and improvements for non-contact wireless vital sign monitors are also included in this chapter.

2. CARDIOPULMONARY MONITORING WITH DOPPLER RADAR

Human cardiopulmonary activities can be detected by Doppler radar through clothing and bedding. Physical movements caused by respiration and heartbeat on the surface of the chest can be picked up by radar, and vital sign information can be extracted out of the radar signal. Non-contact vital sign monitoring can have many potential applications, such as search and rescue for survivors under rubble, infant monitoring [8], burn injury victims, sleep monitoring [4], tumor tracking [9], occupancy detection [11], and home healthcare monitoring [7]. It is a valuable alternative for situations where the use of electrodes is almost impossible, like on burn victims or neonates.

Several research studies have been done to address issues and challenges in this area [15-17, 26, 27]. Before dealing with the challenges that Doppler radar physiological sensing faces, a thorough understanding of the topic is needed. An in-depth explanation about the receiver topologies for radar vital signs sensing, coupling effects, signal conditioning, digitization, demodulation, rate calculations, receiver architectures and recent advances in physiological monitoring is provided in this chapter.

2.1 Doppler Radar Theory

Continuous-wave radar is a common method for measuring physiological information due to its inherent simplicity. The narrowband nature of this topology, unambiguous velocity detection, and filtering and amplifying simplification make it attractive for physiological sensing.

Based on Doppler theory, a target with a time-varying position but no net velocity will reflect the signal such that its phase is modulated in proportion to the time-varying position of the target. The phase difference is due to the variations in the roundtrip time travel of the signal reflected off the target. A stationary human subject's chest movements are a good example of periodic movements with no net velocity. Fig. 2.1 illustrates a human subject's chest motions and phase modulation caused by it. Demodulating the phase will provide information that is directly related to respiratory movements and heart contractions. The transmit signal can be expressed by the following equation:

$$T(t) = \cos(\omega_0 t + \Phi(t)) \tag{2.1}$$

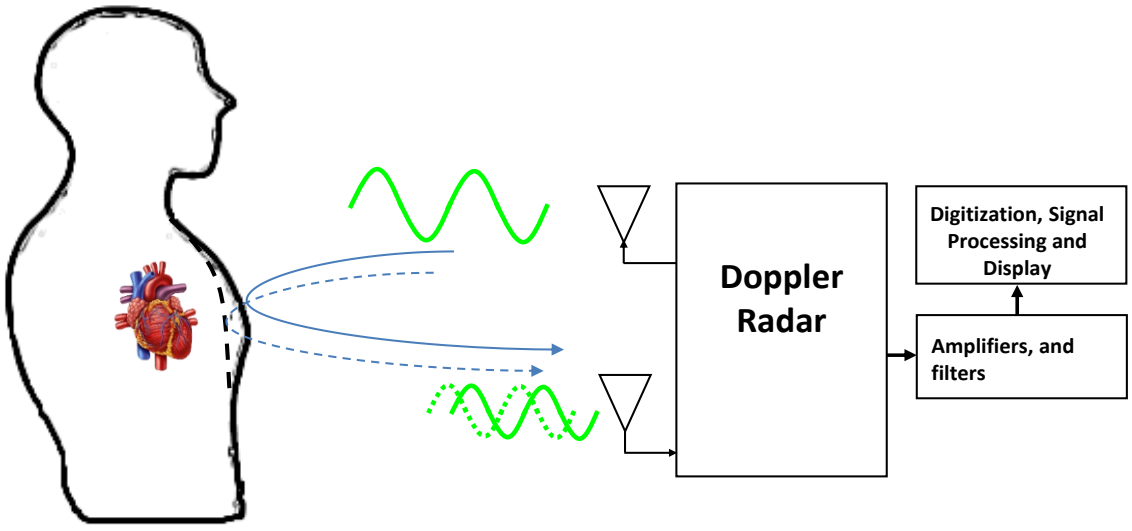

Fig. 2.1 Doppler radar principle of operation, phase modulation caused by the chest motion.

where ω_0 is the oscillation frequency of the transmitted signal, and $\Phi(t)$ is the oscillator phase noise. Phase noise is a characteristic of any signal source and it is due to random phase fluctuation within the oscillator. If the subject is at nominal distance d_0 with respect to the transmitting antenna, and has a time-varying chest displacement *x(t)*, the distance between the target and the radar will be:

$$d(t) = d_0 + x(t) \tag{2.2}$$

The transmitted microwave signal travels to the target and the back-scattered portion of the signal is captured by the receiving antenna. The received portion of the signal goes through a phase change due to path length variations and amplitude change. It can be best expressed by the following:

$$R(t) = A_r \cos(\omega_0 t + \frac{2\pi}{\lambda}(2d_0 + 2x(t)) + \Phi\left(t - \frac{2d_0}{c}\right) + \Theta_0) \tag{2.3}$$

where $R(t)$ is the time-delayed version of the transmitted signal, A_r is the received signal amplitude, λ is the wavelength of the signal, $\Phi\left(t - \frac{2d_0}{c}\right)$ is the time-delayed version of the phase noise, and Θ_0 is the constant phase shift which is caused by the reflection surface and time delay between transmitter and antenna and between the antenna and the mixer. It is apparent the phase of the received signal is modulated by the periodic chest motion *x(t)*. To detect the chest motion, the phase needs to be demodulated.

Since the target's motion information is buried in phase, phase noise of the oscillators is extremely important. When the same signal source is used for both transmitter and receiver, the phase noise of the reflected signal is correlated with the receiver local oscillator. The level of correlation depends upon the time delay between the two signals.

When the time delay is small, which is the case for vital sign monitoring, the phase noise effect is greatly reduced at the baseband. The phase noise reduction is called range correlation [28] and the radar system is called coherent radar [29].

Wavelength can be related to frequency with the following equation:

$$\lambda = \frac{c}{f} = 2\pi \frac{c}{\omega} \tag{2.4}$$

where c is the speed of light, since electromagnetic waves travel at the speed of light. Majority of the experiments that will be covered in the following sections are performed with f = 2.4 GHz signal, which has a wavelength of about 12.5 cm.

2.2 Receiver Architecture

2.2.1 Single-channel Receiver

A single-channel system is a simpler version of the Doppler radar receiver. Fig. 2.2 shows the block diagram of such a receiver. The transceiver is composed of a signal generator, mixer, splitter, antennas, filters, amplifiers, and a data acquisition device.

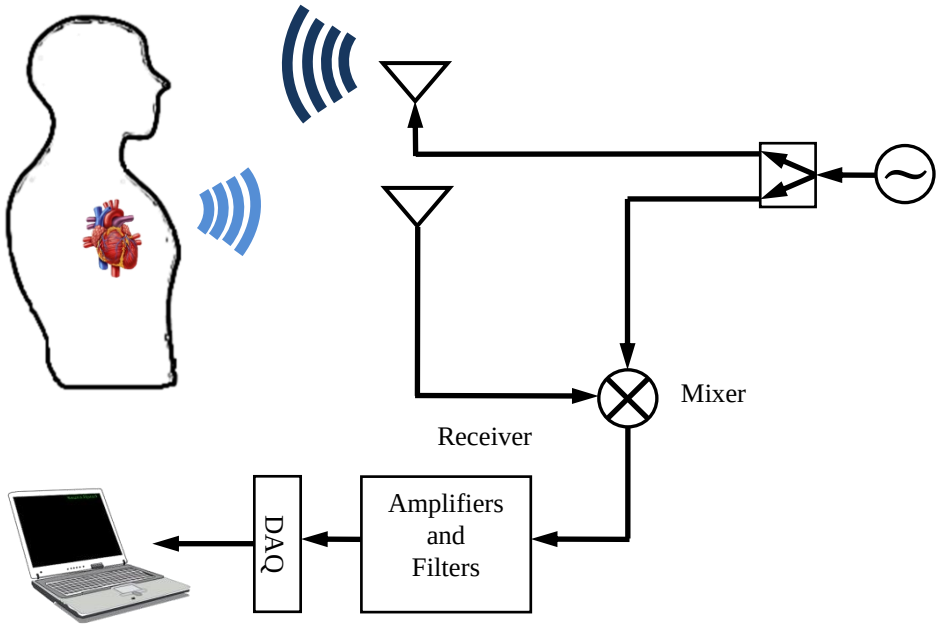

Fig. 2.2 Single-channel receiver block diagram

The frequency down conversion is performed by directly multiplying the delayed received signal with the transmitted signal. The mixer output is:

$$B(t) = T(t)R(t) \tag{2.5}$$

or

$$B(t) = A_r \cos\left(\omega_0 t + \Phi(t)\right) \cos(\omega_0 t + \frac{2\pi}{\lambda}(2d_0\varphi + 2x(t)) + \Phi\left(t - \frac{2d_0}{c}\right) + \Theta_0) \tag{2.6}$$

It can be rewritten as:

$$B(t) = \frac{1}{2}A_r \begin{Bmatrix} \cos\left(\frac{2\pi}{\lambda}\left(2d_0 + 2x(t)\right) + \Phi\left(t - \frac{2d_0}{c}\right) - \Phi(t) + \Theta_0\right) + \\ \cos(2\omega_0 t + \frac{2\pi}{\lambda}(2d_0 + 2x(t)) + \Phi(t) + \Phi\left(t - \frac{2d_0}{c}\right) + \Theta_0) \end{Bmatrix} \tag{2.7}$$

The second term of the equations in the bracket has the doubled radial frequency $2\omega_0$, which will be filtered out by baseband low-pass filters. Since it is a coherent receiver the phase noise difference is also small and can be eliminated. The output in baseband after

filtering is:

$$B(t) = \frac{1}{2}A_r \cos\left(\frac{2\pi}{\lambda}\left(2d_0 + 2x(t)\right) + \Theta_0\right) \tag{2.8}$$

The phase in the above equation has a constant part, which is:

$$\theta = \frac{4\pi d_0}{\lambda} + \Theta_0 \tag{2.9}$$

and a variable part that can be written in this form:

$$\phi(t) = \frac{4\pi x(t)}{\lambda} \tag{2.10}$$

Equation (2.10) shows the direct relationship between chest displacement and phase of the modulated signal in the receiver. For a 2.4 GHz case, 50 mm chest displacement will translate into 28.8° phase change. Since these receivers directly convert the RF band signal into baseband, they are called direct conversion or homodyne receivers as well. Simplicity is the main advantage of a single-channel receiver; however, the sensitivity of this type of receiver changes due to nominal distance (d_0) between the target and radar [30].

2.1.1.1. Position Sensitivity

To further explore that, two different scenarios are considered. First, d_0 is assumed to be a multiple integer of a quarter of the wavelength:

$$d_0 = n\frac{\lambda}{4} \tag{2.11}$$

By replacing d_0, the phase turns into:

$$\frac{2\pi}{\lambda}\left(2d_0 + 2x(t)\right) = n\pi + \phi(t) \tag{2.12}$$

By plugging it back into (2.8) and assuming $\Theta_0 = 0$ the result is:

$$B(t) = \frac{1}{2}A_r \cos\left(n\pi + \phi(t)\right) = \pm\frac{1}{2}A_r \cos(\phi(t)) \tag{2.13}$$

Since the motion is small, the resulting angle would also be small. For small varying phase, a Taylor series expansion can be written in the following form:

$$B(t) = \pm\frac{1}{2}A_r\cos\big(\phi(t)\big) \cong \pm\frac{1}{2}A_r \mp \frac{1}{2}A_r\frac{\phi(t)^2}{2!} \pm \frac{1}{2}A_r\frac{\phi(t)^4}{4!} \mp \cdots \cong \pm\frac{1}{2}A_r \qquad (2.14)$$

Since the cosine version of the phase is received, this equation illustrates the result of variable phase part is almost constant and not very sensitive to chest motions. This scenario is an unwanted one and called null point. In the second scenario it is assumed that the nominal distance are odd multiples of an eighth of the wavelength:

$$d_0 = \frac{2n+1}{8}\lambda \qquad (2.15)$$

After inserting (2.15) into (2.8) the resulting baseband signal would be:

$$B(t) = \frac{1}{2}A_r\cos\left((2n+1)\frac{\pi}{2} + \phi(t)\right) = \pm\frac{1}{2}A_r\sin(\phi(t)) \qquad (2.16)$$

Taylor series expansion of this equation is:

$$B(t) = \pm\frac{1}{2}A_r\sin\big(\phi(t)\big) = \pm\frac{1}{2}A_r\phi(t) \mp \frac{1}{2}A_r\frac{\phi(t)^3}{3!} \pm \frac{1}{2}A_r\frac{\phi(t)^5}{5!} \mp \cdots \cong \pm\frac{1}{2}A_r\phi(t) \qquad (2.17)$$

In this case, the baseband signal is directly related to the variable phase and is called the optimum case. Based on these calculations, there are distances at which the radar output closely follows the chest motions. On the other hand, at certain positions, the radar output is not proportional to the movements and these null and optimum points are an eighth of a wavelength apart. Although the simplicity of the design makes single-channel receiver attractive, it suffers from position sensitivity. To overcome this issue, one extra path is added to the receiver.

2.2.2 Quadrature receiver

Quadrature receivers are extensively used in communication systems to alleviate null and optimum issues. This architecture employs two channels in the receiver, called in-phase and quadrature to make sure that one channel output is always optimum. Fig. 2.3 shows a quadrature transceiver block diagram.

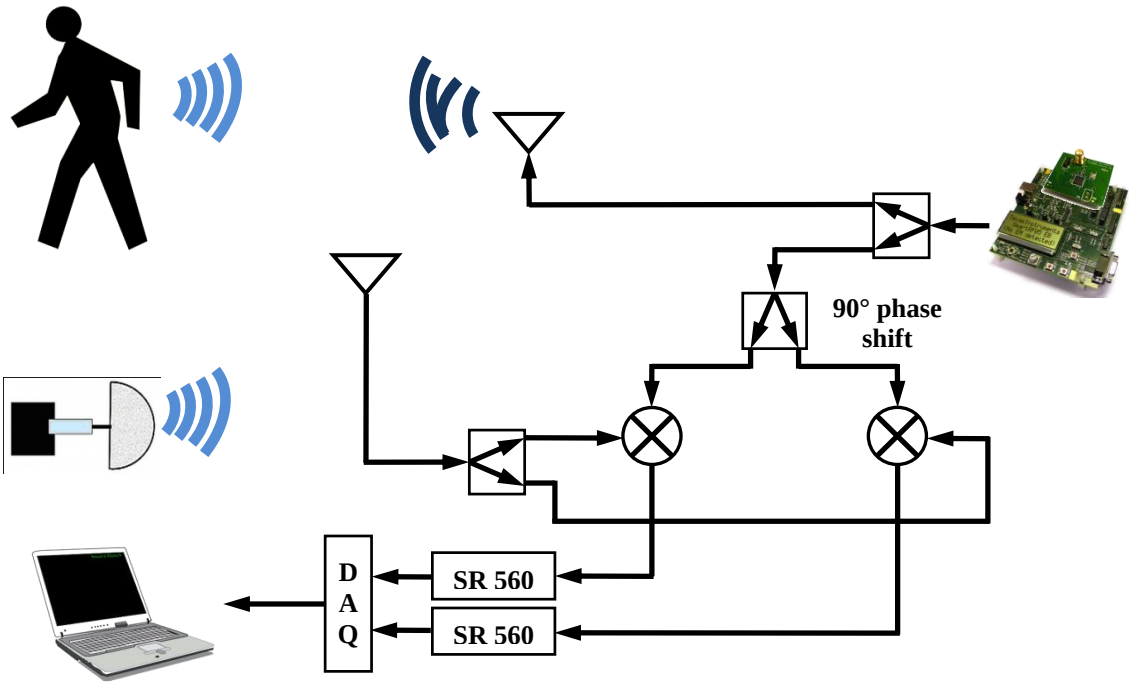

Fig. 2.3 A quadrature transceiver block diagram

The main difference with a single-channel receiver is that in addition to an in-phase channel, one extra path with a 90° phase shifted local oscillator exists. After mixing the in-phase (I) and quadrature (Q) channels, the output can best be described by:

$$B_I(t) = \frac{1}{2} A_r \cos\left(\frac{2\pi}{\lambda}\left(2d_0 + 2x(t)\right) + \Theta_0\right) \tag{2.18}$$

$$B_Q(t) = \frac{1}{2} A_r \sin\left(\frac{2\pi}{\lambda}\left(2d_0 + 2x(t)\right) + \Theta_0\right) \tag{2.19}$$

Since the two versions of the signal are in baseband and have a 90° phase difference,

whenever I channel is the null point ($d_0 = n\frac{\lambda}{4}$), Q channel would be in the optimum point and vice versa. Although quadrature receiver resolves the position sensitivity issue, it adds to the complexity of the system. Since there are two channels in baseband now, they should be combined in a way that select the optimum channel at any selected time [31]. There are two common linear and non-liner demodulation that will be discussed further in this chapter. Any phase and amplitude imbalance between these two channels can introduce error in rate, radar cross section, and displacement measurements [18, 20]. The effects of channel imbalance will be discussed thoroughly in chapter 3. The quadrature outputs can be directly represented in a complex plane in the form of (B_I+jB_Q). Fig. 2.4 illustrates the arc that IQ plot forms.

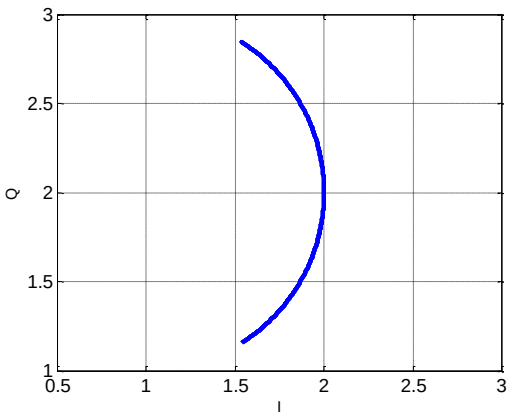

Fig. 2.4 Arc formed by and I and Q channel

2.2.3 CW and Pulse Radar for Physiological Monitoring

Homodyne CW radio architecture is commonly used for microwave Doppler radar non-contact cardiopulmonary monitoring [32-34]. Direct conversion radar receivers have the advantage of simplicity and reduced phase noise due to range correlation [34]. However, one of the challenges in these receivers is the large DC offset in the baseband, which

saturates the baseband amplifiers and reduces the dynamic range of the receiver.

In contrast to CW radar, pulsed radar systems transmit narrow pulses with a large peak power at a constant pulse repetition frequency (PRF) and analyzes the time-delayed received echoes reflected from target objects. Pulse radars that employ the Doppler shift for detecting moving targets are either MTI (moving target indication) radars or pulse Doppler radars [25]. Traditional pulse radar has the advantage of measuring range, in addition to velocity information. If the radar pulse width is long enough and if the target's Doppler frequency is high enough, it may be possible to detect the Doppler frequency shift on the basis of the frequency change within a single pulse. Fig. 2.5(a) represents the reflected RF pulse train, and Fig. 2.5(b) is the baseband demodulated signal when there is a recognizable Doppler frequency shift. Detecting a Doppler shift on the basis of a single pulse of width T generally requires that there be at least one cycle of the Doppler frequency f_d within the pulse; or that $f_d T > 1$. This condition, however, is not usually met when detecting respiration and heart rate since the Doppler frequency f_d (usually in the range of 0.1 Hz to 1.5 Hz) is generally much smaller than $1/T$. Thus, the Doppler effect cannot be observed within a single short pulse in this case. Fig. 2.5(c) is more representative of the Doppler frequency for pulse based physiological monitoring radar. The Doppler effect is shown sampled at the pulse repetition frequency (PRF).

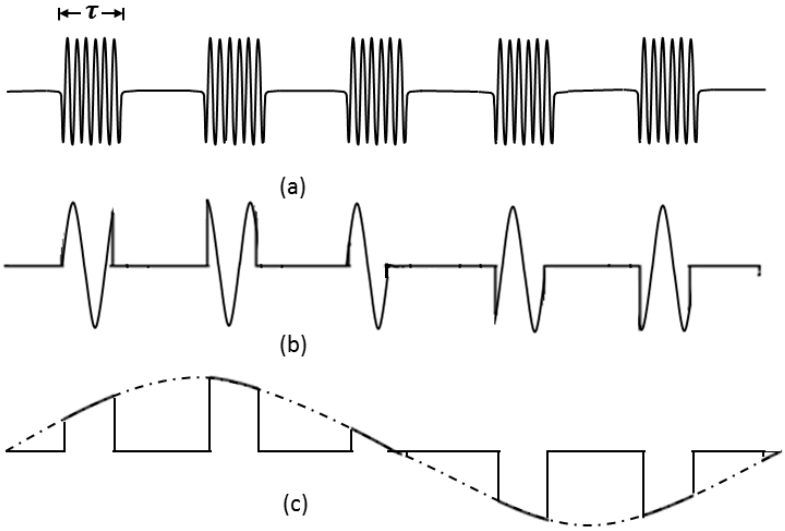

Fig. 2.5 RF back scattered pulse train (a); baseband demodulated signal when the Doppler frequency $f_d > 1/T$ (b); and baseband signal for the Doppler frequency $f_d < 1/T$, which is usually the case for physiological signals with frequencies less than 2 Hz (c). The Doppler frequency signal is shown dashed.

2.3 DC Offset and Coupling Effects

Homodyne CW radio architecture is commonly used for microwave Doppler radar non-contact cardiopulmonary monitoring [32-34]. Direct conversion radar receivers have the advantage of simplicity and reduced phase noise due to range correlation [34]. However, one of the challenges in these receivers is the large DC offset in the baseband which saturates the baseband amplifiers and reduces the dynamic range of the receiver.

CW radar can measure the instantaneous rate-of-change in the target's range. In a quadrature CW homodyne Doppler radar system, the I and Q channel outputs can be represented by:

$$B_I(t) = V_I + A_I \cos(2\pi f_d t + \varphi_I) \tag{2.20}$$

$$B_Q(t) = V_Q + A_Q \cos(2\pi f_d t + \varphi_Q) \tag{2.21}$$

Where V_I and V_Q are DC offsets, and A_I, A_Q, φ_I, and φ_Q are amplitudes and phases of

the respective channels, and f_d represents Doppler frequency.

There are two main sources for the DC offset in direct conversion receivers. One of the DC offset sources is due to self-mixing, which occurs when the RF output signal mixes with the LO, either through substrate coupling or from reflections at the antenna connection. The self-mixing can introduce large DC offsets at baseband at the IF port [33]. Clutter is another source of DC offset. It is assumed that the signal hits much of the body that is not moving, as well as the stationary objects in the background. Reflections from each of these objects will introduce DC offset in the baseband. The DC offset problem may not cause problems in communication systems, since the information is commonly far from DC. However, in the case of physiological signals, it could be around 0.1 Hz for respiration signals, which is very close to DC. The nature of the signals to be dealt with dictates a very good low-frequency response for baseband circuits. If DC coupling is employed, respiration and heart traces are preserved. However, due to the relatively large DC offset, the amount of gain which is needed to amplify weak received echo signals from the target will be limited and the signal cannot be amplified to the desired level for digitization.

AC coupling is one of the common methods for removing DC offset of the signal. However, since physiological signals occupy a very low frequency spectrum, including DC, high-pass filter cut-off frequencies must be very low (on the order of 0.01 Hz) to preserve most of the signal content. Thus, AC coupling will introduce large settling time and signal distortion. Fig. 2.6 illustrates the effects of AC/DC coupling. Fig. 2.6(a) is DC coupled and IQ plot forms an arc which is marked by $\varphi(t)$ and is part of a circle. However, the exaggerated AC coupling IQ plot is depicted in Fig. 2.6(b). The ribbon-

shaped arc is clearly the result of AC coupling distortion. Although the AC coupling removes the DC offset and there is more room for amplification, it distorts the signal shape and introduces error in displacement measurements.

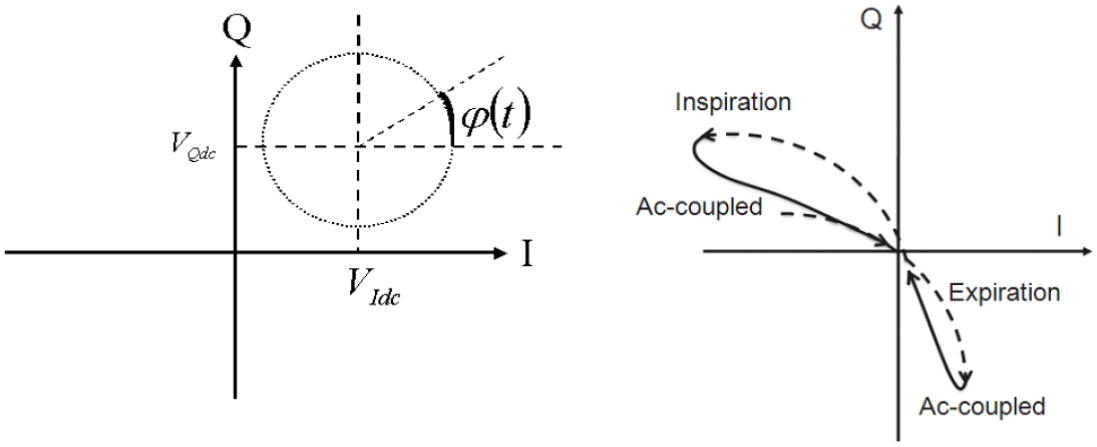

Fig. 2.6 In-phase and quadrature signals plotted on IQ complex plane; (a) DC coupled signal; the dotted line is the circle fitted to the available arc; (b) exaggerated AC coupled signal. Ribbon-shaped arc is the result of AC coupling distortion.

A DC offset reduction method is proposed by [35], using a mixer with high LO to RF port isolation, but the radar still suffers from DC offset. In [31], a DC cancellation method is introduced to alleviate the issue. However, this technique needs cumbersome calibration and continuous adjustment during measurement. In [33, 36] the DC offset was measured and cancelled using two stages of fixed and variable gain amplifiers, but it adds to system complexity.

As long as pulse frequency content is sufficiently high in the case of pulse radar, where the Doppler information is carried by the train of pulses, low frequency distortion due to AC coupling will not significantly affect the demodulated waveform.

2.4 Signal Conditioning and Data Acquisition

There are several noise sources that can affect the performance of the transceiver. Phase noise is significantly problematic, and by using a coherent receiver, it can be alleviated. Flicker noise or 1/f noise shows up as a low-frequency phenomenon, as higher frequencies are usually overshadowed by other noise sources. It causes signal-to-noise ratio (SNR) to be lower than at an intermediate frequencies [37, 38]. Thermal noise is the dominant RF noise and has a flat spectrum, which means it does not vary with frequency. Theses noise sources show that baseband signal conditioning circuitry's added noise should be minimized and the transmitted power must be high enough so that baseband signal power is well above the noise level. Thus low-noise amplifiers (LNA) and filters are used to condition the signal in baseband before digitization occurs. I and Q signals are low-pass filtered to avoid aliasing and reduce the out-of-band noise. Depending upon the type of signal, the low-pass corner frequency changes from a few Hz to 300 Hz. Respiratory activity is in the centimeter range and cardiac contractions can induce millimeter range movements to the chest surface. Physiological signals have a very low frequency signature, usually between 0.2 Hz~2 Hz. However, for pulse radar, the shape of the pulse has to be preserved and higher corner frequencies are employed.

Vital signs have a bandwidth between DC-8 Hz [15, 16]. According to the Nyquist sampling theorem, the minimum sampling rate should be twice the bandwidth of the signal. However, much higher sampling rates, between 100 Hz to 8 kHz, are used to minimize any out-of-band interference, lower the noise floor, and preserve the pulse shape in the case of pulse and packet radar [39-41]. In addition to the sampling rate,

resolution of the analog-to-digital convertor (ADC) is another key factor for acquiring the signal accurately. It dictates the amount of quantization noise added to the baseband signal. Because the resolution of ADCs is limited, quantization error is introduced when the signal sample value falls between two levels. Increasing the resolution decreases the quantization error. The minimum change in input of an ADC that makes a change in the output is known as the least significant bit. A 16-bit ADC is used for digitizing the signal, and has sufficient resolution for acquiring vital sign signals. A 16-bit ADC quantizes the input into 2^{16} = 65536 levels. The least significant bit for the 10v reference voltage would be:

$$\Delta = \frac{V_{Ref}}{2^n} = \frac{10}{2^{16}} = 0.15mV \tag{2.22}$$

2.5 Demodulation

Single-channel receiver has one output baseband signal. Since there is only one channel at the output, the baseband signal is proportional to the phase changes of the signal, assuming small-angle approximation. Therefore there is no need for any further demodulation. However, the single channel suffers from position sensitivity or null and optimum points. Quadrature receiver alleviates this issue, but there would be two channels in the baseband that should be properly combined. Combining I and Q channels and obtaining the optimum signal regardless of the nominal distance between target and receiver is called demodulation. There are two major methods, called linear and nonlinear demodulation, for combining I and Q signals and extracting phase information [17, 31].

2.5.1 Linear Demodulation

If the arc length of the IQ plot is small and small-angle approximation is valid, linear demodulation is a straightforward method to use. Linear demodulation combines the two signals by using linear operations. However, this method is unable to provide absolute displacement information. One of the procedures for linear demodulation is principle component analysis (PCA) [42]. PCA projects multi-dimensional data into single dimension, suppressing redundant information, and maximizing the variance in data. PCA first removes any DC offset from the I and Q channels. Then, the covariance matrix of the I and Q channels is calculated, and finally, I and Q data are projected onto the eigenvector of the covariance matrix that has the largest eigen value. In the IQ plot illustrated in Fig. 2.7, PCA rotates the arc to be parallel with one of the axes, and projection of the arc would be maximized on one of the axes (Q-axis in Fig. 2.7), providing optimum demodulation.

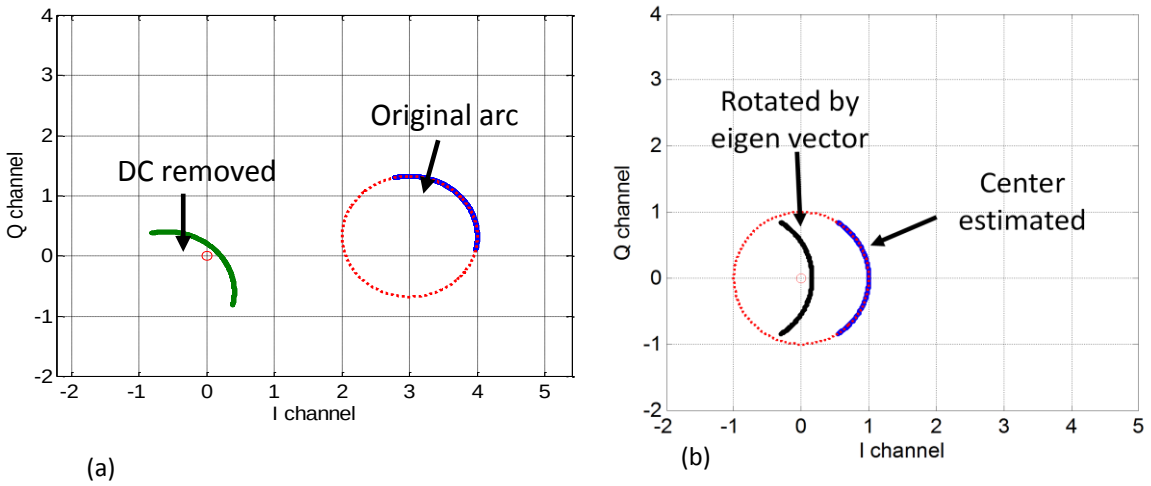

Fig. 2.7 (a) Original arc before and after DC removal, (b) Rotating the arc to be parallel to the Q channel.

2.5.2 Non Linear Demodulation

Small-angle approximation may not be valid if the arc in the IQ plot becomes large due to large displacement or higher frequencies. A 2.4 GHz signal is accurate up to 46.8° phase changes or 0.81 cm corresponding displacement [31]. Linear demodulation performance deteriorates for phase variations larger than that and nonlinear demodulation should be employed. However, the nonlinear method is more prone to noise and distortion. Arctangent demodulation is a nonlinear method for extracting phase information. If the I and Q signals where pure sine and cosine signals, the phase could be extracted by simply dividing those two channels and taking the arctangent:

$$\varphi(t) = \frac{B_Q(t)}{B_I(t)} = \arctan\left[\frac{\frac{1}{2}A_r \sin\left(\frac{2\pi}{\lambda}(2d_0+2x(t))+\Theta_0\right)}{\frac{1}{2}A_r \cos\left(\frac{2\pi}{\lambda}(2d_0+2x(t))+\Theta_0\right)}\right] = \theta + \phi(t) \tag{2.23}$$

which directly gives the phase and displacement information. However, any imbalance between the quadrature channels and DC offset modifies (2.23) into:

$$\varphi(t) = \frac{B_Q(t)}{B_I(t)} = \arctan\left[\frac{V_Q+A_E A_r \sin\left(\frac{2\pi}{\lambda}(2d_0+2x(t))+\Theta_0+\varphi_E\right)}{V_I+A_r \cos\left(\frac{2\pi}{\lambda}(2d_0+2x(t))+\Theta_0\right)}\right] \tag{2.24}$$

where V_I and V_Q are the DC offset of each channel, A_E is the amplitude imbalance, and φ_E is the phase imbalance between the channels. As (2.24) illustrates, the phase cannot be estimated correctly, unless DC offset and imbalance between the channels are resolved. The channel imbalance can be corrected for known phase and amplitude imbalance with Gram-Schmidt or ellipse correction methods, which are common in communication systems. If there is no imbalance between the two receiving paths in the receiver, the IQ plot would consist of an arc, which is part of the circle. Any imbalance between these two channels converts the circle into an ellipse, as illustrated in Fig. 2.8 with 20° phase imbalance and no amplitude imbalance.

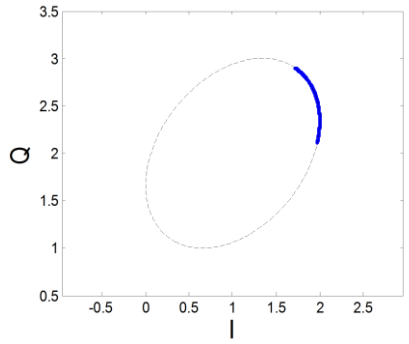

Fig. 2.8 IQ plot deformed into an ellipse due to imbalance. The imbalance values are 20° phase and 0 amplitude imbalance

For a Doppler radar system, the arc is usually small, as opposed to a complete ellipse or circle, which makes the estimation of imbalance values harder. There are different methods for extracting correction coefficients for the Gram-Schmidt technique [18, 43]. A data-based best-fit ellipse method does not involve any hardware modification [18]. This method is an algebraic ellipse-fitting method for getting the imbalance values as illustrated in Fig. 2.9. It also shows the corrected circle after applying the Gram-Schmidt orthonormalization method for extracted amplitude and phase mismatch.

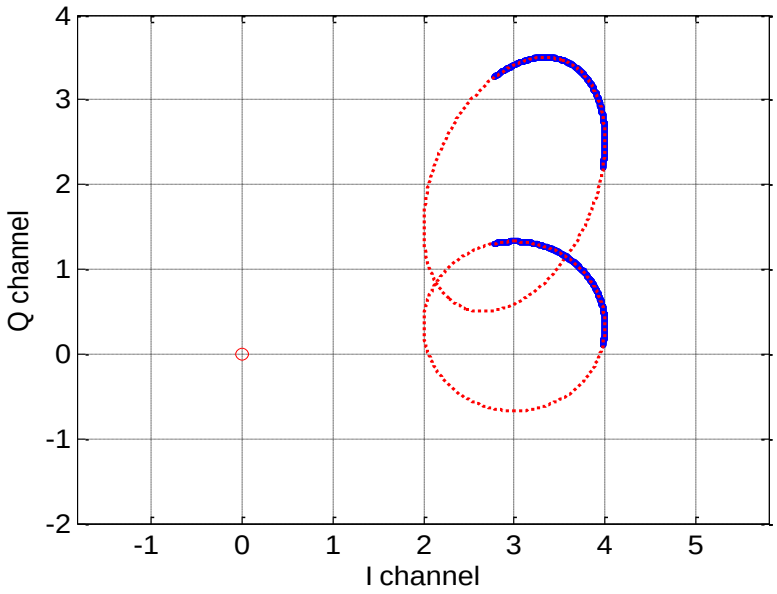

Fig. 2.9 IQ plot with imbalance which is part of an ellipse, and corrected version using Gram Schmidt technique.

Once the arc is corrected, the center of the circle should be found to estimate the correct value of the phase. There are algebraic and geometric fitting methods for estimating the center of the circle and correcting the DC offset value [20]. Steps of center estimation with DC correction in [17] are displayed in Fig. 2.7.

1- The DC value of the signal is removed.
2- The arc is rotated to be parallel to Q axis (similar to PCA)
3- A heuristic estimator is used to find the center of the circle. For two points A and B on a circle, any line though the middle point of the chord connecting A and B goes through the center of the circle.
4- The center of the arc is shifted to the center and arctangent is applied to get the phase.

For larger arcs or displacement, arc tangent demodulation has superior performance, but arc length and SNR of the signal can affect the performance of arctangent demodulation [18, 44].

2.6 Rate Calculations

Heart and respiration rate information are of significance importance in the diagnosis of numerous health problems. Heart rate variability or beat-to-beat interval measurements reflect the functionality of the cardiovascular system [45-48]. There is a need for a time-dependent rate analysis tool. There are three methods for estimating the heart and respiration rate from Doppler radar signals: peak finding, Fourier transform, and autocorrelation.

2.6.1 Peak Finding

The peak finding method calculates the time between two consecutive peaks, and by inverting the average time in a window, the rate is estimated. This method works for electrocardiogram (ECG) signals that have a high signal-to-noise ratio and sharp peaks at the R-wave in each period. It may not be the best option for Doppler radar, where the peaks are not as well defined as ECG signals.

2.6.2 Fourier Transform

Fourier transform is extensively used for frequency-domain analysis of a signal. Since an instantaneous rate is desired, the data is divided into different chunks depending upon the window length. Then, the Fast Fourier Transform (FFT) is calculated for each window. FFT is a very efficient algorithm for calculating the Fourier transform for discrete signals. The peak of the FFT is found for each segment of data, which represents rate in that specific window. Then, the window moves to the next chunk of data based on predefined steps. The window length is determined by FFT resolution, as well as the degree of averaging for instantaneous rate. Depending on the application, the window should be long enough to contain several periods of the signal. A typical window size for a heart signal is 6-10s. Respiratory signals have lower frequencies (around 0.2 Hz). Consequently, larger windows, usually 10-18 seconds, should be selected [15, 16]. Usually, bell-shaped windows such as Hamming, Hanning, and Kaiser windows, are used instead of rectangular windows to shape the data in time domain, which provides more control over sidelobes in spectral domain. In other words, a windowing function

minimizes the effect of leakage to better represent the frequency spectrum of the data.

Fig. 2.10 shows the block diagram for getting the Doppler radar signals' rate. First, the I and Q signals are filtered by analog filters in baseband. Then, the two signals are combined into one by either linear or nonlinear demodulation. After demodulation, the signals are again digitally filtered to eliminate as much noise as possible. Window functions shape the window for minimal spectral leakage. Finally, Fourier transform is applied and the rate is calculated. Fig. 2.11 shows a subject's heart rate extracted using the Fourier transform method with radar.

Fig. 2.10 Fourier transform rate extraction method for Doppler radar signals

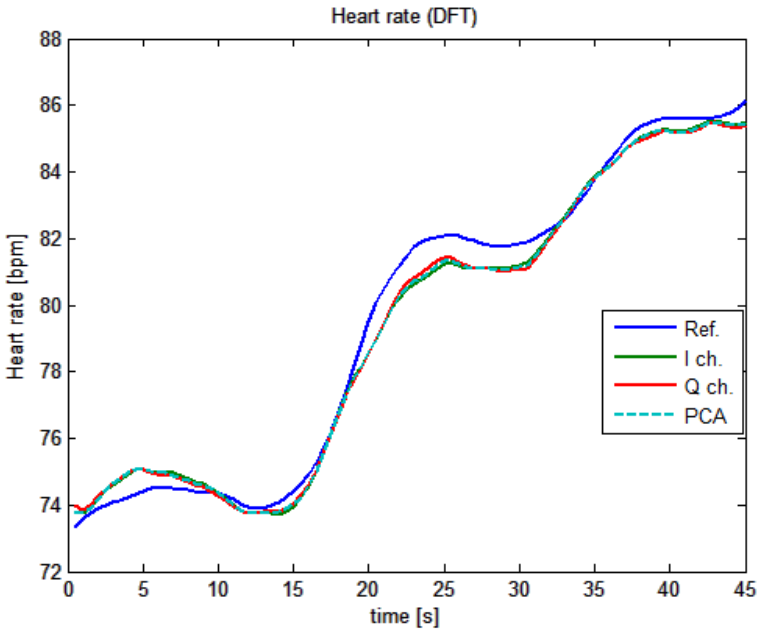

Fig. 2.11 Rates extracted using Fourier transform. Reference chest belt signal is illustrated versus in-phase and quadrature channels from radar and linear demodulated output (PCA). Subject was holding his breath during this experiment, and the rise of heart rate is due to that.

A reference chest belt signal is illustrated versus in-phase and quadrature channels from the radar and linear demodulated output (PCA). The subject was holding his breath during this experiment, and the rise of heart rate is due to that.

2.6.3 Autocorrelation method

In this method, the signal is multiplied by a delayed version of itself, and the results would be added together. It is performed for all possible delays. This function emphasizes the periodic pattern in a signal [49]. The autocorrelation for discrete windowed signals with length *N* can be defined:

$$R_{xx}[m] = \frac{1}{N}\sum_{n=0}^{N-m-1} x[n]w[n]\cdot x[n+m]w[n+m] \tag{2.25}$$

where $R_{xx}[m]$ is the autocorrelation function, *N* is the number of samples, *m* is the delay, and $w[n]$ is the windowing function. The result would be a function of the time delay, and it shows a prominent peak at the signal's fundamental period. A nonlinear method, called center clipping, is used to flatten the autocorrelation spectrum. It is used to remove unwanted peaks from the signal. The center clipper function is defined as below:

$$C(n) = \begin{cases} 0 & if\ |B(n)| \le k.a_{\max} \\ B(n) & if\ |B(n)| \ge k.a_{\max} \end{cases} \tag{2.26}$$

where c(n) is the center clipper output, *B(n)* is the windowed baseband data, and a_{max} is the maximum amplitude of the signal in the specified window [50, 51]. The block diagram of the autocorrelation method is shown in Fig. 2.12.

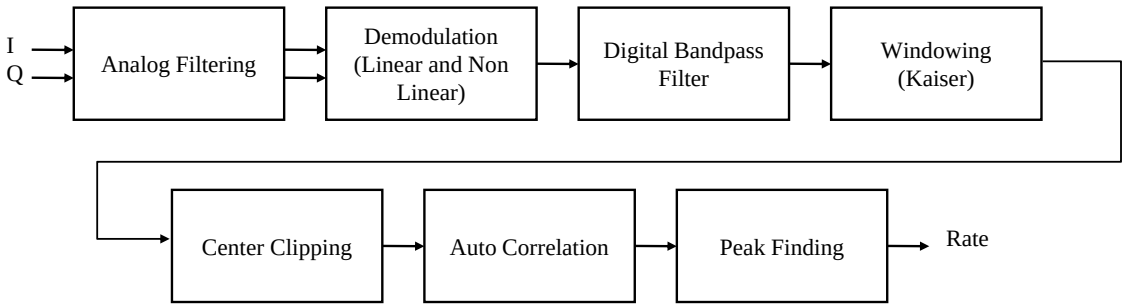

Fig. 2.12 Autocorrelation function rate extraction method for Doppler radar signals.

Fig. 2.13(a) shows the baseband I and Q signals after filtering. It shows that one channel is in optimum and the other is in null point (doubled frequency). Fig. 2.13(b) illustrates the result of linear demodulation, which is in this case is essentially the Q channel.

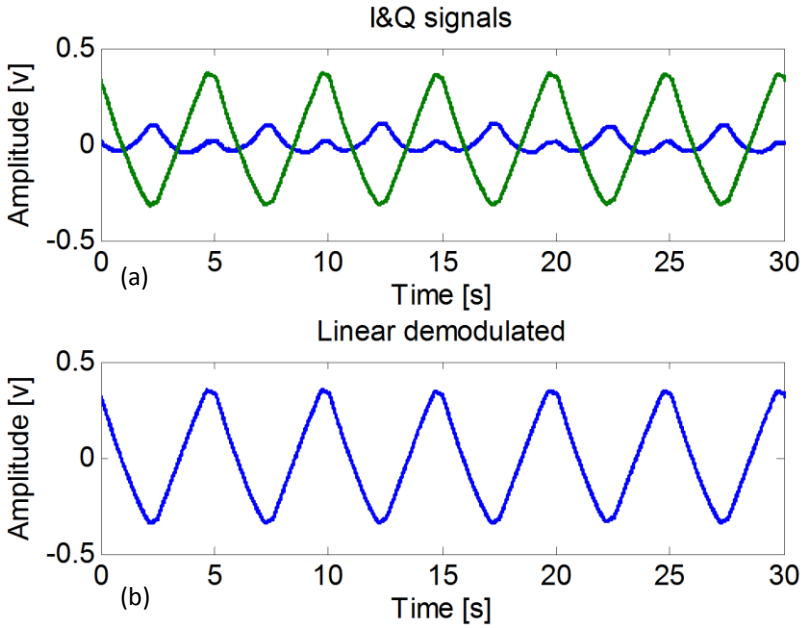

Fig. 2.13 (a) I and Q baseband signals after filtering; (b) linearly demodulated signal.

Fig. 2.14(a) depicts the windowed signal with the Kaiser function applied to the signal in Fig. 2.13(b). Fig. 2.14(b) is the center clipped version of the windowed signal, and

Fig. 2.14(c) illustrates the autocorrelation function output with detected peaks.

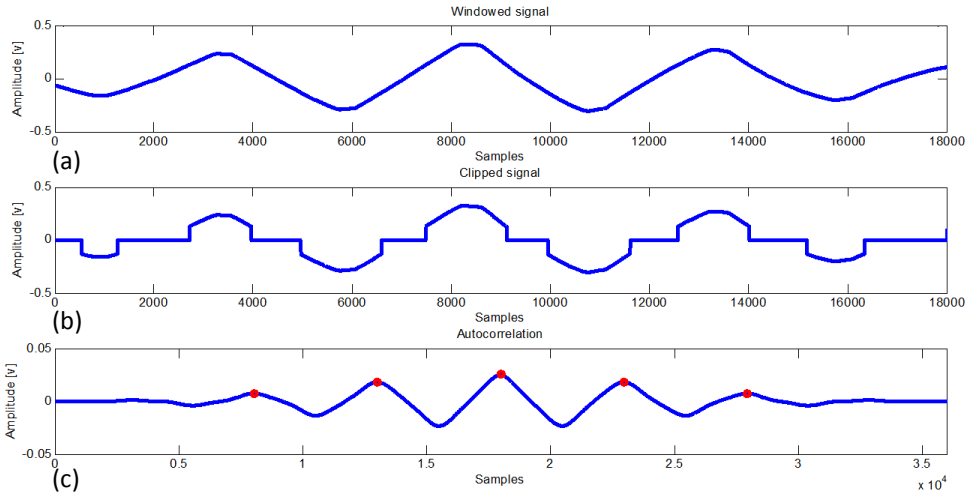

Fig. 2.14 (a) Windowed received signal shaped by 18 seconds Kaiser window; (b) center clipped signal, (c) Autocorrelation output with peaks detected.

2.7 Homodyne, Heterodyne, and Low-IF receivers

The receivers discussed so far directly convert RF signals into baseband. These type of receiver architectures have a simpler design, and are called homodyne or direct conversion receivers. Homodyne receivers do not have the conventional image problem of heterodyne receivers, and do not require image reject filters. It is a straightforward architecture for phase detection. The issues with homodyne receivers are DC offset, coupling, and low-frequency noise [44, 52, 53]. An alternative to homodyne receivers are heterodyne receivers. Heterodyne receivers mix the RF signal with a different frequency from the local oscillator of the transmitter, and the signal is down-converted to an intermediate frequency instead of being directly converted to baseband. A heterodyne receiver architecture is depicted in Fig. 2.15. The signal is amplified with an LNA and filtered at the RF stage by a band pass filter for image rejection. The LNA improves the

receiver noise figure by boosting the signal power. The signal is then down-converted to an intermediate frequency by a mixer. The IF bandpass filter isolates the desired channel and is usually a high-quality filter. The IF amplifier is typically a programmable-gain amplifier adjusted to the level of the signal. Based on the modulation scheme, the detector could be a down converter to baseband, quadrature receiver, differentiator, or an envelope detector.

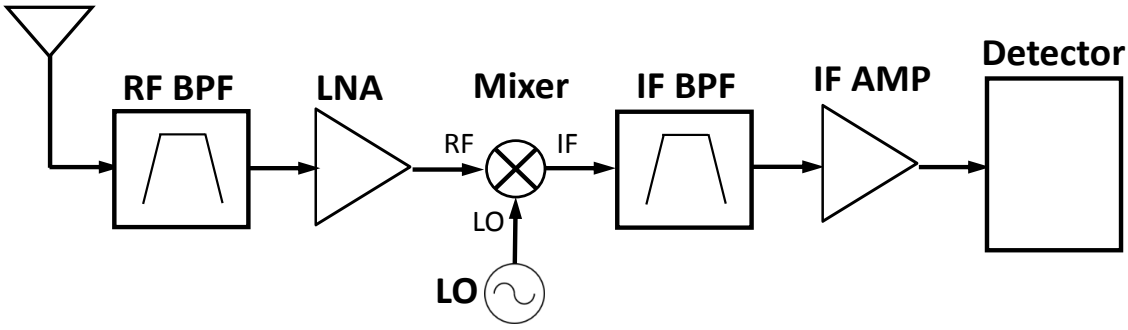

Fig. 2.15 Heterodyne receiver architecture

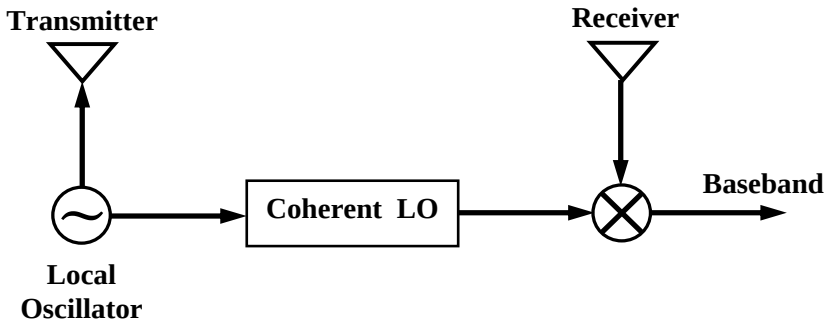

Fig. 2.16 A coherent low-IF receiver

Low-IF is another receiver architecture that is used in wireless communication [54]. It is a type of heterodyne receiver with an IF frequency low enough to be digitized directly. It avoids the DC offset issue, and has less flicker noise due to being further away from DC. Unlike communication low-IF receivers, local oscillators are derived from the same

source to take advantage of coherent reception. Fig. 2.16 shows a low-IF architecture for physiological sensing.

2.8 Recent Advances in Physiological Monitoring

Doppler radar was first used for measuring respiration rate in 1975 with big and bulky microwave equipment [13]. It wasn't until 2002 that the first integrated vital sign monitor was fabricated using silicon CMOS technology [55] onto a single chip that integrated all RF circuits including local oscillators [34]. Despite the early start, many of the advancements have been made during the last decade.

A thorough study of Doppler radar for physiological monitoring is presented in [15] including design requirements and tradeoffs, transceiver architecture, noise sources, and integrated circuit implementation (2006). In [17], single-channel limitations, quadrature receivers, linear and nonlinear demodulations have been investigated. Motion artifacts are a major challenge for vital sign sensing, and novel techniques to alleviate this problem was introduced in [56, 57]. Ka-band millimeter wave radar was employed in [58] for measuring respiration and heart rate (2005). A heterodyne receiver was tested using low-power double-sideband transmission and frequency tuning techniques to avoid detection null points [41] (2006). Separating multiple subjects' vital signs is one of the challenges that Doppler radar faces. [59] shows the feasibility of such a task using multiple-input multiple-output systems and signal processing techniques such as blind source separation [60, 61]. Subject isolation and identification are also examined in [62] using passive RF tags. This system allows for independent tracking and monitoring moving sources with tags, and identifies and rejects the clutter.

A baby monitoring device is introduced in [8] as an innovative application for Doppler radar (2007). Heart beat and respiration signals are detected from four sides of the body in [63]. Sleep monitoring is another emerging application of radar, which alleviates the use of obtrusive devices, such as spirometers, that can change the sleeping pattern. A clinical study was performed to monitor patients with sleep apnea problems using radar sensors in conjunction with traditional sensors [5] (2014). In fact, sleep monitoring devices are the first commercial devices that recently received FDA approval for commercial use in United States. An analog linear demodulator and CW coherent low-IF are introduced in [64, 65] to improve noise performance of the radar. A novel signal processing technique is used to eliminate unwanted signal interference in [66, 67]. Long-term vital signs measurements are performed in [2], where various health-related parameters such as heart rate variability (HRV), respiratory tidal volume, and respiratory sinus arrhythmia (RSA) are measured on twenty subjects. Radar has also been used to monitor the health and behavior of land and sea animals such as lizards and fish [68-70].

Although there was a huge progress in Doppler radar physiological sensing systems during the last decade, there is still a lot of room for improvement. Some of the issues that have not been addressed in previous work include the effects of distortion, noise, and interference on system performance. In this work, it will be shown that distortion can severely limit the effectiveness of non-contact vital sign measurements. Thus, it is crucial to develop methods to eliminate distortion and make the system more robust to noise. In addition, new and more effective signal estimation methods are sought to improve the system's performance.

3. QUADRATURE CHANNEL IMBALANCE

Respiratory rate, heart rate, pulse pressure, and volumetric measurement are important indicators of human health status [71, 72]. Doppler radar physiological monitoring has shown promise for such health monitoring [13, 73-75]. However, distortions such as quadrature channel imbalance, local oscillator leakage, DC offset, and flicker noise limit the sensitivity and accuracy of the radar system [31, 76, 77]. Small motions induced by heart contractions cause average skin surface displacements on the order of 100 μm. Although this displacement falls within the range of Doppler radar resolution, it requires careful calibration and measurement.

Quadrature receivers are used to avoid the phase demodulation null points problem in Doppler radar transceivers [31]. However, one additional path in the receiver architecture typically causes amplitude and phase imbalance between the in-phase and quadrature outputs of the receiver. Another factor that impacts Doppler radar measurements under channel imbalance is the nominal distance between the transmitter antenna and the subject. Since the nominal distance is directly related to the initial phase, it has been taken into consideration, in addition to phase and amplitude imbalance.

Channel imbalance distorts baseband spectrum, decreases SNR, and increases bit error

rate in communications systems [76, 78-80]. In this chapter, it is demonstrated that in Doppler radar physiological monitoring, channel imbalance can distort shape of physiological signals, introduce significant errors in displacement, effective radar cross section [81], and heart rate estimation.

In [76], Doppler radar quadrature imbalance effects on displacement were examined for a complex demodulation method. However, this method provides only peak-to-peak displacement information and not displacement versus time, thus obscuring distortion effects. In [18] a data-based method for finding imbalance values was investigated and possible corrections were explored. Different imbalance estimation methods and their accuracies were compared in [20]. In this section, the severity of channel imbalance itself is examined without any corrections. Due to technology advancement in integrated devices, the imbalance values are limited to less than 15° phase imbalance and 2 dB amplitude imbalance [].

Arctangent demodulation with center estimation and radius adjustment is used to show amplitude imbalance, phase imbalance and initial phase effects on radius, pattern, displacement, and rate. A precision linear stage is programmed to emulate complex physiological motions. Experimental data for displacement error with a varying initial phase is in close agreement with simulation data. Experiments also support simulations that heart rate detection can be affected by channel imbalance.

In this chapter, a displacement estimation method based on varying the initial angle is proposed, which does not require any correction. In addition, a new imbalance values estimation method is proposed using data points with varying initial angles. This method does not require using any additional calibration targets, and can be used with any

measurable arc length.

3.1 Doppler Radar Imbalance Factors

Wireless detection of small physiological movements using Doppler radar is based on a Doppler shift caused by body movements during respiratory and circulatory contractions and expansions. When a microwave signal illuminates the subject, the reflected signal is phase modulated by the subject's motion. A phase demodulation technique of mixing the received signal with a portion of the transmitted signal results in a baseband signal that can be processed to yield the movements of the human subject [74].

Phase variations could be demodulated using linear or nonlinear (arctangent) demodulation to obtain an output signal with a low frequency component that is directly proportional to the object displacement [31]. Radar baseband signals can be described by:

$$B_I(t) = V_I + A\cos\left(\frac{4\pi d_0}{\lambda} + \frac{4\pi x(t)}{\lambda} - \theta_0 + \Delta\varphi(t)\right) \tag{3.1}$$

$$B_Q(t) = V_Q + A\ \sin\left(\frac{4\pi d_0}{\lambda} + \frac{4\pi x(t)}{\lambda} - \theta_0 + \Delta\varphi(t)\right) \tag{3.2}$$

where V_I and V_Q are the in-phase and quadrature baseband DC offsets, A is the baseband signal amplitude, d_0 is the nominal distance between radar antenna and the subject, θ_0 is the constant phase shift, and $\Delta\varphi(t)$ is the residual phase noise. The initial phase, θ is:

$$\theta = \frac{4\pi d_0}{\lambda} - \theta_0 \tag{3.3}$$

and is one of the parameters that affect measurement accuracy. When there is an imbalance between in-phase and quadrature paths, it can be modeled as:

$$B_I(t) = V_I + A\cos\left(\theta + \frac{4\pi x(t)}{\lambda} + \Delta\varphi(t)\right)$$
$$B_Q(t) = V_Q + AA_E \sin\left(\theta + \frac{4\pi x(t)}{\lambda} + \Delta\varphi(t) + \varphi_E\right) \quad (3.4\text{-}5)$$

where A_E is the amplitude imbalance, and φ_E is the phase imbalance.

3.2 Radar Signal Modeling

To show the effects of imbalance on physiological signals, a model is needed for radar-detected heart and respiration signals. An idealized chest motion can be modeled with a half-cycle of a sinusoid raised to the *pth* power [82]:

$$P_R(t) = \sin^P \pi f_R t \quad (3.6)$$

where *p* controls the rounding of the cusp and the general shape of the signal. Modeling respiratory signals with raised sinusoids has prolonged and narrow halves which are closer to real respiratory signals detected by radar [83]. f_R is the respiratory frequency and the respiration pulse is repeated at $1/f_R$ intervals. Discharging heart ventricles during the systolic phase generates impulsive motion that is subsequently filtered by the bone and tissue in the chest wall where radar senses the motion [82]. Thus, for modeling the heart signal, an exponential term $e^{-t/\tau}$ is filtered by a critically-damped second-order Butterworth filter with a cutoff frequency f_0 and time constant τ. Then, the pulse shape repeats at $1/f_H$ where f_H is the heartbeat frequency.

$$P_H(t) = e^{-t/\tau} + \left[\left(\frac{\sqrt{2}}{\omega_0\tau} - 1\right)\sin\frac{\omega_0 t}{\sqrt{2}} - \cos\frac{\omega_0 t}{\sqrt{2}}\right] e^{-\omega_0 t/\sqrt{2}} \quad (3.7)$$

40s of data is generated for both heart and respiration signals, with a sampling rate of *fs* =100 Hz. The heart signal amplitude is 3% of the respiration signal amplitude. The heart rate is f_H = 1.25 Hz (75 bpm) and respiration rate is f_R = 0.25 Hz (15 bpm). The other

factors are empirically adjusted to best represent Doppler physiological signals. Fig. 3.1(a) shows the generated respiratory signal with p = 3. Heart signal parameters in Fig. 3.1(b) are τ = 0.05 and f_0 = 1 Hz, where repeated Butterworth-like pulse shapes are evident. Finally, the combination of heart and respiration signals is illustrated in Fig. 3.1(c).

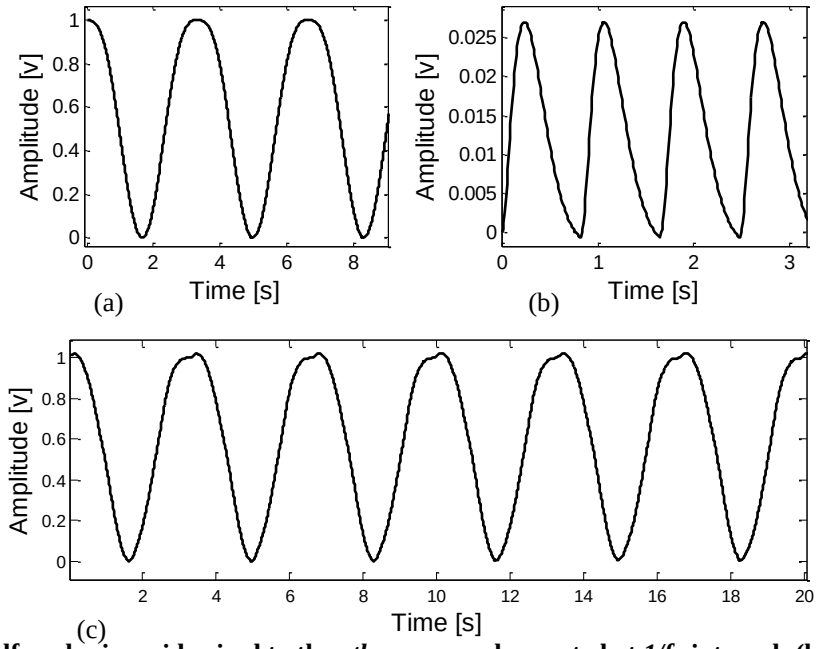

Fig. 3.1 (a) Half-cycle sinusoid raised to the *pth* power and repeated at $1/f_R$ interval; (b) repeated Butterworth-like pulse shape at $1/f_H$ intervals representing heart signal; (c) combined heart and respiration signal.

3.3 Simulation Results

Simulations were done in MATLAB to show the effects of imbalance on physiological measurements. Equations (3.4) and (3.5) were used to represent baseband radar signals and *x(t)* was replaced by a combination of complex movements representing respiratory and heart radar signals according to (3.6) and (3.7). The three parameters 1) amplitude imbalance A_E, 2) phase imbalance φ_E, and 3) initial phase θ, were varied in these simulations and the effects of each one were individually investigated. Nonlinear or

arctangent demodulation was used to extract the phase and displacement information of the simulated radar data [31].

For a successful arctangent demodulation, the center of the arc should be estimated. The heuristic center estimator method was used, and has three steps. The first step is removing the DC offset of the signal. Then the data is multiplied by the transposed matrix of eigenvectors of the covariance matrix V^{T} to rotate the arc and make it parallel to the Q-axis. This is similar to Principle Component Analysis (PCA) which is used in linear demodulation for combining I and Q signals [42]. The final step is to find the center which helps to extract phase and displacement information. When the arc is orthogonal to the I-axis, the center of the circle will be somewhere on the I-axis (k, 0), where k is:

$$\hat{k}(i,j) = \frac{\left|\begin{matrix} B_I[i] \\ B_Q[i] \end{matrix}\right|^2 - \left|\begin{matrix} B_I[j] \\ B_Q[j] \end{matrix}\right|^2}{2.(B_I[i] - B_I[j])} \tag{3.8}$$

$$\hat{k} = \underset{i \neq j}{median}\{\hat{k}(i,j)\}. \tag{3.9}$$

The center of original data is found by multiplying (k, 0) with the inverse transform V^{-1}. Imbalance values change the shape of the circle into an ellipse, distort the arc, and introduce error in finding the center of the circle and hence displacement [84]. Fig. 3.2(a) illustrates the IQ plot and undistorted arc, which is part of a circle. The circle converts into an ellipse once the imbalance values are introduced. In Fig. 3.2(b), the phase imbalance is set to 20° with 15° initial phase, and no amplitude imbalance.

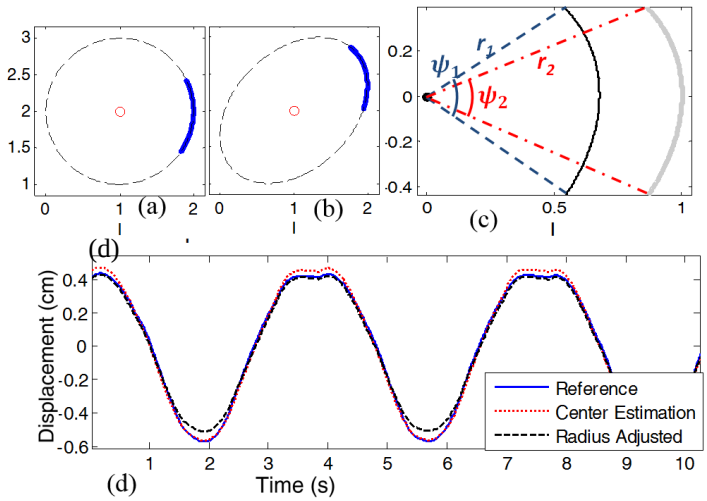

Fig. 3.2 (a) IQ plot for undistorted arc; (b) ellipse in the IQ plane is a clear indication of imbalance between in-phase and quadrature paths; arc length is 16% of the ellipse with 20° phase imbalance, no amplitude imbalance, and initial phase of 15°; (c) different radii detected for center estimation and radius adjusted which translate to different phases; (d) displacement versus time under 20° phase imbalance and 15° initial phase for arctangent demodulation with center estimation and radius adjusted methods.

3.3.1 Amplitude Imbalance

Fig. 3.3(a) shows the effects of amplitude imbalance on displacement. Doppler radar simulated data is a combined complex motion with 1 cm displacement. Imbalance values are varied from -6 dB to 6 dB. The amplitude imbalance can introduce an error as large as 98% for -6 dB imbalance or an estimated displacement of 1.98 cm. To emphasize the importance of the imbalance values, an extreme case is presented with the imbalance value of one channel being half the value of the other (-6 dB). However, with only 1 dB amplitude imbalance, it can introduce up to 12% error in displacement estimation.

Fig. 3.3(b) depicts errors introduced in displacement by amplitude imbalances versus imbalance values. Values are varied from 0.5 to 2 with 0.01 steps, corresponding to -6 dB to 6 dB amplitude imbalance. When imbalance values are larger than 0 dB, the estimated radius would be bigger than one, which results in a displacement smaller than 1 cm.

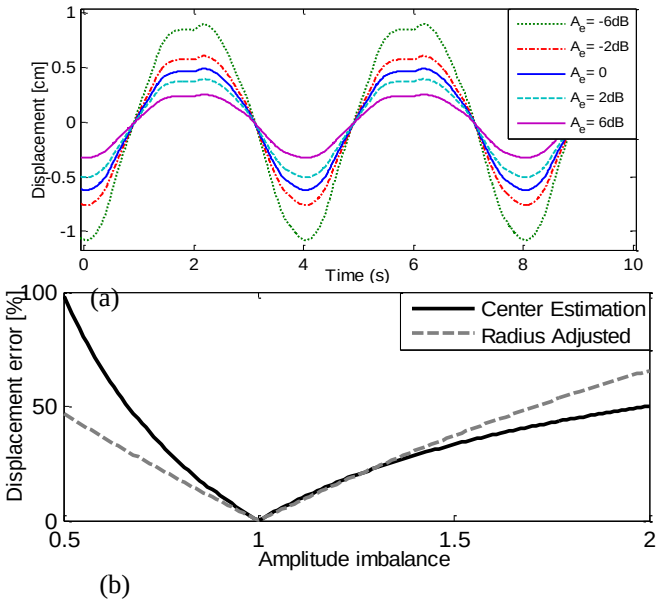

Fig. 3.3 Amplitude imbalance effects on displacement; (a) 1 cm displacement with combined complex shape; amplitude imbalance varied between -6 to 6 dB while phase imbalance and initial angle are kept 0; (b) arctangent demodulation with center estimation and radius adjusted, amplitude imbalance values are varied between 0.5 to 2 linearly with 0.01 steps corresponding to -6dB to 6dB amplitude imbalance.

However, the error is larger even if the radius is adjusted for the known radius. The difference between the arctangent with center estimation method and the arctangent with radius adjustment shows the effects of center estimation. For imbalance values smaller than 0 dB, the effects are reversed and error is larger for center estimation than adjusting the radius for known values.

3.3.2 Phase Imbalance

Phase imbalance is another source of error for absolute displacement measurement. Fig. 3.4(a) shows the effects of phase imbalance on displacement for imbalance values varied from 0° to 40°. The displacement shape is distorted and effects are not symmetrical for positive and negative peaks.

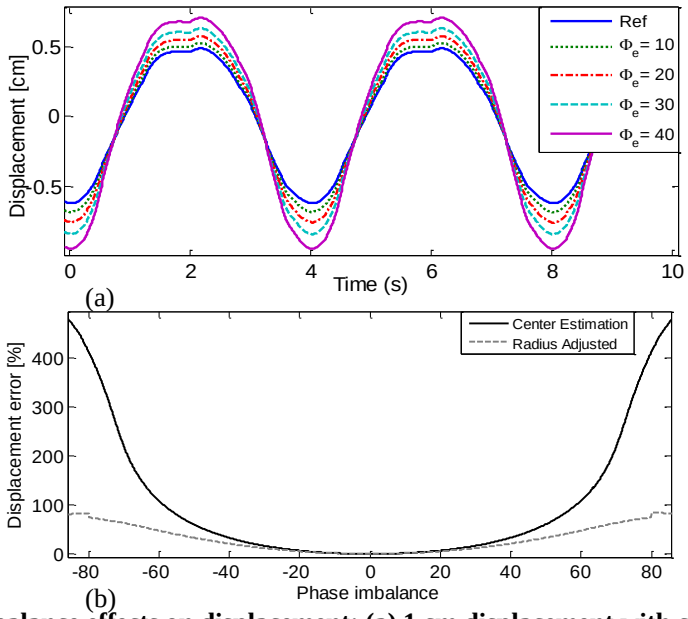

Fig. 3.4 Phase imbalance effects on displacement; (a) 1 cm displacement with combined complex motion; phase imbalance varied from 0° to 40° while amplitude imbalance is kept 0 dB; the displacement shape is distorted and effects are not symmetrical for high and low peaks; (b) arctangent demodulation with center estimation and radius adjusted, phase imbalance values are varied from -90° to 90° linearly with 0.1° steps.

Fig. 3.4(b) illustrates errors introduced in displacement by phase imbalance versus imbalance values changing from -90° to 90° with 0.1° steps. The error increases as the phase imbalance increases. It is interesting to note if the radius is adjusted to a known value, the error will be limited to 85% for extreme values and is always lower than with the center estimation method. However, in the center estimation case, the error can be larger and the shape of displacement can be heavily distorted. Once again, the difference between center estimation and radius adjusted methods shows pure center estimation error.

3.3.3 Initial Phase

Another important factor that affects the physiological measurements is initial or residual phase in the presence of phase or amplitude imbalance. Since the nominal distance is

directly related to the initial phase, the error changes based on the location of the target. Fig. 3.5(a) illustrates displacement for initial phase values of 0°, 29°, and 75°, while the phase imbalance is kept 20°. For θ = 0°, the error in displacement with center estimation is 6.9%. When θ = 29°, the error reaches its peak around 43.4%. However, with θ = 75° the error is almost 0% and it overlaps with the reference displacement even when there is a 20° phase imbalance. Fig. 3.5(b) shows the location of the arc on the ellipse for different initial phase values. In contrast with communication systems, the arc is small and is not a complete circle, which makes the displacement estimation much harder. It is interesting to note when the arc is at any of the two vertices, it introduces the largest error.

Fig. 3.5(c) shows the effects of initial phase on displacement. In this simulation, amplitude imbalance is 0 dB and phase imbalance is adjusted to be 20°, while initial phase changes from 0° to 360° with 1° steps. There are certain phases that, even in the presence of imbalance, the error in displacement measurement can be zero. The reason for that is because the center estimation algorithm estimates the closest radius based on the location of the arc on the ellipse. The radius-adjusted method presents smaller error with a larger zero crossing phase compared to the center estimation method.

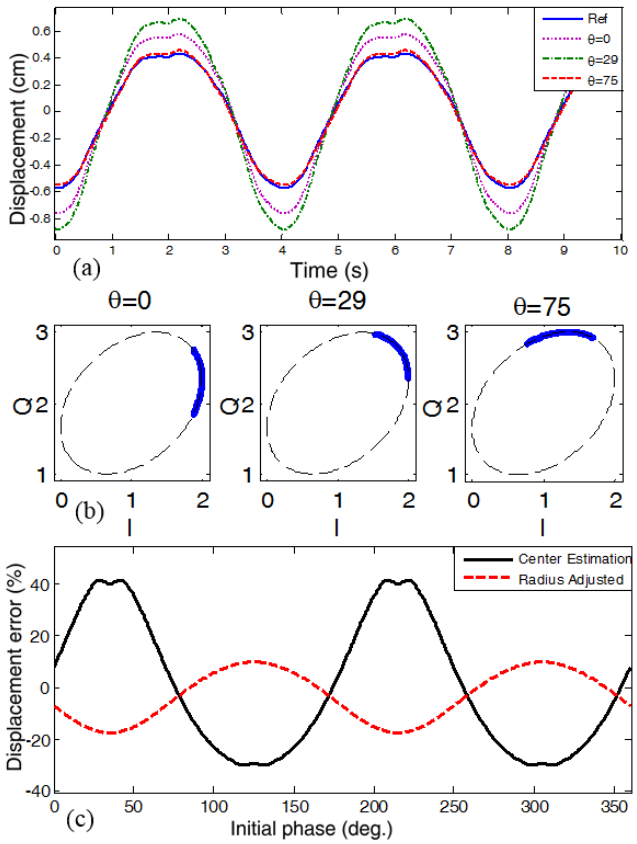

Fig. 3.5 Displacement for different initial phases; (a) the error in displacement with center estimation drops from 43.4% to 0 by changing only the initial phase or the nominal distance between receiver and subject; amplitude imbalance is kept 0 dB and phase imbalance is 20°; (b) Different initial angles spread the arc at different locations over the ellipse; (c) absolute value of error in displacement measurement when initial phase changes from 0° to 360°; amplitude imbalance is 0 dB and phase imbalance is adjusted to be 20°; zero crossing points show, even in the presence of imbalance the error in displacement measurement can be zero.

3.4 Effects of the Imbalance on Rate

The imbalance values are of great importance in measuring the displacement, especially for high accuracy measurements. In Doppler radar physiological sensing, respiratory rate and heart rate are also of interest. To show the effects of imbalance on rate estimation, the model introduced in section 3.2 is employed. In this model, second and third respiration harmonics are lower than the heart signal amplitude. After modeling the signal, phase and amplitude imbalance are added to observe the effects of imbalance on rate.

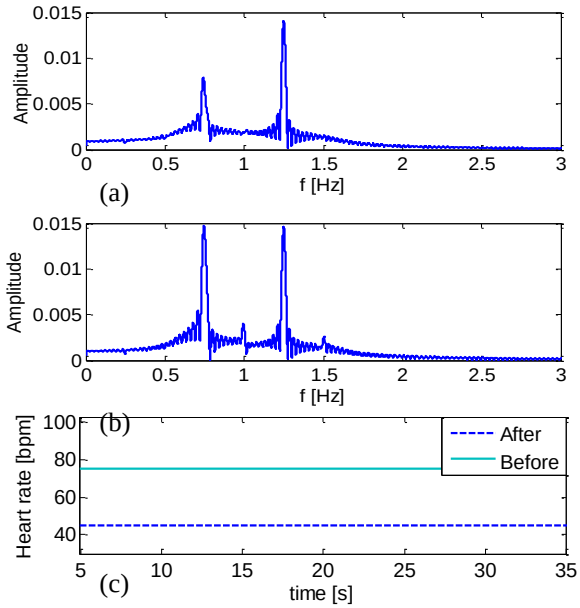

Fig. 3.6 Filtered heart spectrum without imbalance (a), filtered heart spectrum with 2 dB amplitude imbalance and 60° phase imbalance (b), calculated heart rate before (75 bpm) and after (45 bpm) introducing imbalance values.

Fig. 3.6(a) shows filtered heart signal spectrum before adding imbalance values. Fig. 3.6(b) depicts heart spectrum when 2 dB amplitude imbalance and 60° phase imbalance are introduced to the signal. The amplitude of the second harmonic of respiration is larger than the heart signal amplitude. This is clearly due to imbalance effects. To further examine the heart signal, heart rate is calculated over 40s of data. First, the DC part of the signal is removed for heart rate estimation.

After DC cancellation, the signal is filtered using an FIR filter with corner frequencies of 0.7 Hz to 1.5 Hz, where the normal heart rate falls. Then, an 8 second Kaiser window is used to slide over the data. Fast Fourier transform is computed and the peak of the frequency response is selected as the rate for each particular window. Then, the window slides with 0.5s steps. Calculated heart rate with and without imbalance values are shown in Fig. 3.6(c). Before adding imbalance values, the radar signal and reference heart rate is measured at 75 bpm. However, when the imbalance values are added the second

harmonic of the respiration (45 bpm) is mistakenly detected.

3.5 Ellipse Fitting

In simulations, the imbalance values that are introduced were known. However, for practical applications, it should be measured. A method for measurement of amplitude imbalance and phase imbalance for a single antenna quadrature Doppler radar system using the GS method has been described in [43]. This method requires adding phase shifters to simulate a moving target in front of the radar and produce a more complete phase cycle. However, it may not always be practical or desirable to make a modification to an existing radar system for such measurements. Another method of imbalance measurement involves using two synchronized oscillators to feed in RF and LO signals at slightly different frequencies and use time-domain analysis to measure the imbalance factors. However, this method is not suitable for single antenna systems involving a circulator. The imbalance measurement method should be such that it could be used without any modification with different Doppler radar system architectures, at the user's convenience.

In this chapter, a data-based method is used that can provide imbalance values without any hardware modifications. A mechanical target is also employed to produce a sufficient arc length to be able to perform the best-fit ellipse method for calibration.

An ellipse can be defined by an equation:

$$\frac{\breve{x}^2}{a^2}+\frac{\breve{y}^2}{b^2}-1=0, \tag{3.10}$$

where $\breve{x}=(x-c_1)\cos\theta-(y-c_2)\sin\theta$ and $\breve{y}=(x-c_1)\sin\theta+(y-c_2)\cos\theta.$ The ellipse parameters are Θ_1 = (a, b, c_1, c_2, θ), where (c_1, c_2) is the center, a, and b are the semiaxes,

and θ is the angle of tilt of the ellipse [85]. Another equation for an ellipse is:

$$Q(x, y) = Ax^2 + Bxy + Cy^2 + Dx + Ey + F = 0, \tag{3.11}$$

where the parameters Θ_2 = (A, B, C, D, E, F) define the ellipse. These two parameter spaces are directly convertible. Furthermore, the conversion from Θ_2 parameter space to imbalance factors is trivial, as shown in [86].

Two common ellipse-fitting methods are geometric and algebraic fittings. The classical least squares fit minimizes the geometric distances d_i's from data points to the fitting ellipse:

$$F = \sum_{i=1}^{n} d_i^2 \quad . \tag{3.12}$$

The equation (3.12) has no closed-form solution, but it can be solved either iteratively or approximately [85].

On the other hand, in the algebraic fitting method, the algebraic ellipse equation (3.11) is used as an objective function for minimization [87, 88]. This minimizes the algebraic distance Qi. The main advantages of algebraic methods are their fast and simple operations. In addition, they do not require an initial guess. To further analyze the algebraic method and derive the objective function, the signals in the I and Q channel can be represented by:

$$I = A_I \cos(\frac{4\pi x(t)}{\lambda} + \phi_I) + B_I \tag{3.13}$$

$$Q = A_Q \sin(\frac{4\pi x(t)}{\lambda} + \phi_Q) + B_Q \tag{3.14}$$

where B_I and B_Q represent DC offsets, $x(t)$ is the time varying displacement of the target, λ is the radar wavelength, $A_e = \frac{A_Q}{A_I}$ is the amplitude imbalance, and the phase imbalance is $\phi_e = \phi_Q - \phi_I$ $\phi_e = \phi_Q - \phi_I$. Expanding (3.14) and combining with (3.13)

results in:

$$\left(\frac{Q}{A_Q}-\frac{B_Q}{A_Q}\right)^2+\left(\frac{I}{A_I}-\frac{B_I}{A_I}\right)^2-2\left(\frac{Q}{A_Q}-\frac{B_Q}{A_Q}\right)\left(\frac{I}{A_I}-\frac{B_I}{A_I}\right)\sin(\phi_e) \\ -\cos^2(\phi_e)=0 \tag{3.15}$$

After expanding (3.15) and substituting $A_e=\frac{A_Q}{A_I}$, the coefficients of the Q^2, I^2 and IQ terms that are of interest are given by $\frac{1}{A_e^2}$, 1, and $\frac{2\sin(\phi_e)}{A_e^2}$ respectively.

$Q^2, I^2 and IQ terms;$afterexpanding(3),wehave:The normalized standard equation of an ellipse (I is the horizontal axis, and Q is the vertical axis) could be written as:

$$I^2+A\times Q^2+B\times IQ+C\times I+D\times Q+E=0 \tag{3.16}$$

Comparing the coefficients of (3.15) and (3.16), amplitude imbalance and phase imbalance can be determined as:

$$A_e=\sqrt{\frac{1}{A}} \text{ and } \phi_e=\sin^{-1}\left(\frac{B}{2\sqrt{A}}\right). \tag{3.17}$$

$A_e=\sqrt{\frac{1}{A}}, and \phi_e=\sin^{-1}\left(\frac{B}{2\sqrt{A}}\right)$.Assuming we have measured N (N>>5) samples of data (I_1, Q_1), (I_2, Q_2).....(I_N, Q_N), in an ideal situation, all of these N points would satisfy the ellipse equation, as following:

$$A\times {Q_N}^2+B\times I_NQ_N+C\times I_N+D\times Q_N+E=-{I_N}^2 \tag{3.18}$$

Let the coefficient matrix of the above linear system be an N by 5 matrix:

$$M=\begin{bmatrix} Q_1^2 & I_1Q_1 & I_1 & Q_1 & 1 \\ \vdots & \vdots & \vdots & \ddots & \vdots \\ Q_N^2 & I_NQ_N & I_N & \cdots & 1 \end{bmatrix} \tag{3.19}$$

and let the right hand side of the linear system be:

$$b=\begin{bmatrix} -I_1^2 \\ \vdots \\ -I_N^2 \end{bmatrix} \tag{3.20}$$

The best solution for A, B, C, D, E can be found in [89]:

$$\begin{bmatrix} A' \\ B' \\ C' \\ D' \\ E' \end{bmatrix} = \left(M^T M\right)^{-1} M^T b \tag{3.21}$$

Once the coefficients have been estimated, the imbalance factors can be computed using (3.17).

3.6 Experimental Results

A set of experiments were designed to evaluate the simulation results. A Galil precision linear stage is employed to produce a combined heart and respiration complex motion described by (3.6) and (3.7). Respiration signal amplitude is 1cm and heart signal amplitude is 3% of the respiration signal amplitude. The block diagram of the system is depicted in Fig. 3.7. In this experiment, a rectanglular metallic object with a length of 20 cm a width of 15 cm is attached to the linear stage and used as the target. The target is placed one meter away from the antenna. An HP 83640B signal generator operates at 2.4 GHz with 7 dBm output power. The reference signal is divided into in-phase and quadrature channels by a 90° splitter on the receiver side. Two identical Minicircuits ZFM4212 mixers are used to down-convert the received signal into baseband. A 0° divider splits the received RF signal into two channel signals with the same phase and amplitude. A Pulsar ST-21-444A variable phase shifter and Broadwave 751-00-030 variable attenuator are inserted in one of the LO lines to introduce an intended amount of mismatch between the two channels. Down-converted signals are then filtered and amplified with Stanford Research SR560 low noise amplifiers. The received baseband signals are recorded by a data acquisition device with a 100 Hz sampling rate.

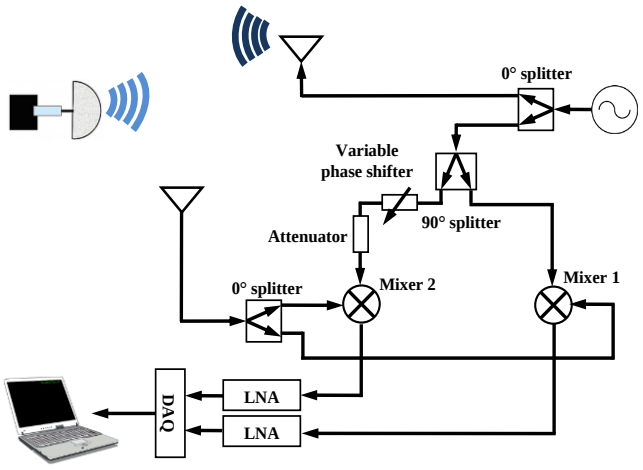

Fig. 3.7 Block diagram of the experimental setup with phase shifter and attenuator inserted in one of the quadrature channels.

3.6.1 Effects of the Imbalance on Rate

The amount of amplitude mismatch is set 2 dB and measured with a spectrum analyzer. After inserting the attenuator, the control voltage of the phase shifter is adjusted to achieve the intended phase difference between the I and Q channels. The phase mismatch is evaluated by measuring the phase of S_{21} insertion loss parameter of the phase shifter. The ellipse-fitting method as previously described is used to measure the phase mismatch. The fitted ellipse shows a total -27° phase shift between the two channels. It is worth noting that the measured phase imbalance value is the sum of externally introduced imbalance and inherent phase imbalance between the two channels. Since the initial angle depends on the starting distance between the target and antenna, simulations are adjusted to match the initial angle to the experimental set-up.

Fig. 3.8(a) shows the baseband signal captured from the radar when there is -27° phase and 2 dB amplitude mismatch between the channels compared with the ideal simulated signal. The mechanical target is programmed to generate two superimposed complex motions according to (3.6) and (3.7). Error in displacement between ideal and

experimental values due to channel imbalance is clearly visible in this figure. Spectrum of the heart signal with no external imbalance is depicted in Fig. 3.8(b). Amplitude and phase imbalance values are then introduced through attenuator and phase shifter. Fig. 3.8(c) shows the spectrum with imbalance values. As predicted in simulations, the amplitude of the second harmonic of respiration became larger than the heart signal amplitude, due to mismatch between the channels. The same setting and processing methods described for simulations are used in experiments. The experiments support the simulation results, in that imbalance values can change the estimated rate. The second harmonic of respiration (45 bpm) is mistakenly detected as opposed to actual heart rate (75 bpm).

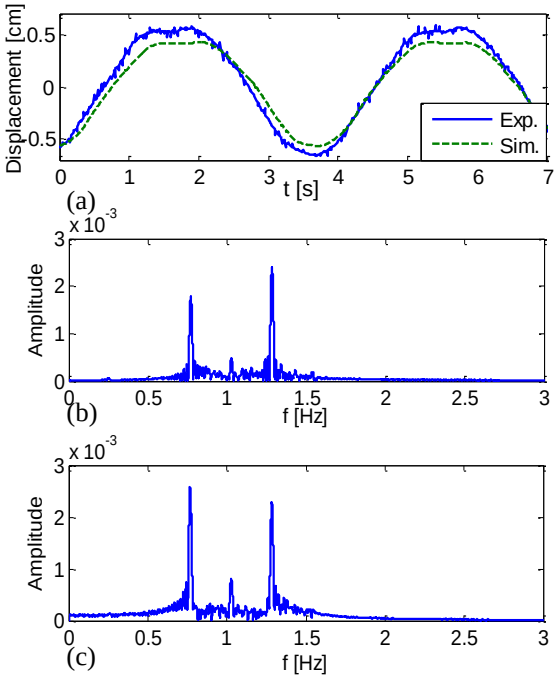

Fig. 3.8 Experimental and simulated radar signals. (a) The inserted phase shifter and attenuator caused overall -27° phase and 2dB amplitude mismatch; simulation represents the ideal case without any imbalance; (b) filtered heart spectrum before introducing attenuator and phase shifter; (c) heart spectrum after imbalance values are introduced; second harmonic of the respiration signal becomes larger than the heart signal amplitude.

3.6.2 Effects of the Imbalance on Displacement Measurements

An experiment is conducted to evaluate displacement errors for fixed imbalance and varying initial phase. First, the channel imbalance parameters are measured to extract phase and amplitude imbalance. Those values are needed to be implemented in the simulation. The measured values are 11.9° phase imbalance and 0.96 amplitude imbalance. In these measurements, a mechanical target is used for measuring imbalance values and investigating initial phase effects on radar data.

Fig. 3.9(a) shows the IQ plot when the mechanical target moves with 3 cm displacement and frequency f=0.2 Hz in front of the radar. At 2.4 GHz, the IQ plot forms an arc corresponding to 48% of the ellipse. A larger arc is used for more accurate imbalance measurement based on the ellipse-fitting method. The measured imbalance values based on the data-based method [18] are 11.9° for phase and 0.96 for amplitude.

To change the initial phase in the experiment, the initial distance should be changed, according to (3.3). For this measurement, precise control is needed over the movement of the mechanical target. Otherwise, slight changes in initial distance could have drastic effects on initial phase and the center of the IQ plot. For this purpose, a precise linear stage mover with 5 μm accuracy is employed. The experiment consists of 21 stages; in each stage, a mechanical target used to simulate respiration signal with a sinusoidal motion of 1 cm displacement and f=0.2 Hz. Each stage is recorded for 60s with a 100 Hz sampling rate, and the displacement error is calculated as well. Then, the mover reference point is moved 2mm toward the radar in each stage and sinusoidal motion is repeated with the same displacement and frequency. At the last step, the mover's reference point was 40 mm closer to radar receiver antenna than the first stage, replicating a respiratory

signal corresponding to a 230° phase difference of the receiving signal. Fig. 3.9(b) illustrates arcs for all 21 stages in one plot. The alternating colors show different arcs; each arc corresponds to 1 cm displacement, 57.6°, or 16% of the circle. The arcs move around the ellipse due to 2mm reference point change at each stage, which translate to 11.5°.

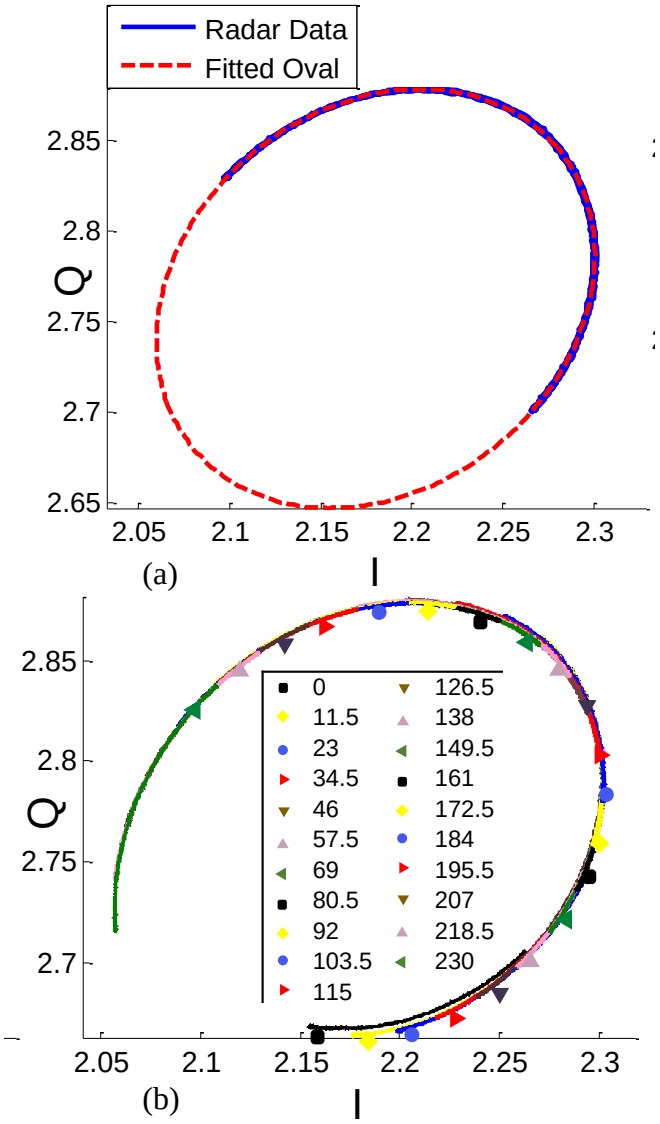

Fig. 3.9 IQ plot for measuring imbalance values; (a) the arc is 48% of the ellipse corresponding to 3 cm displacement for 2.4 GHz radar; the dotted line shows fitted ellipse for measuring imbalance values; phase and amplitude imbalance are 11.9° and 0.96 respectively; (b) 21 sets of experimental data with 1 cm displacement and 2 mm steps between stages; the legend shows the relative initial phase for each step, zero relative initial phase starts form the bottom right.

Simulations were done with the same imbalance parameters, movement shape,

displacement, and frequency as the experiment in Fig. 3.9(b). Initial phase is varied with 1˚ steps, compared to 2 mm steps in the previous experiment, which translate to 11.5˚. The result of the experiment is depicted versus simulations in Fig. 3.10(b). In this figure, actual peak-to-peak displacement is shown versus different initial phases for different scenarios. The solid line is the simulation result and the square dotted lines are the experimental values without any correction.

Based on the pattern of displacement error as initial phase changes, the median value of the maximum and minimum experimental peak-to-peak displacement deviation values would give the optimum initial angle. A simple calibration step can be added to find the optimum initial angle for displacement measurement. The mechanical target can start from one initial point, and then the center of the movement is shifted step by step in one direction either toward the receiver or away from it. The steps are selected to be even; therefore, finding the optimum point would be easier. The measurements are continued until maximum and minimum displacement deviation points are reached. The median value of all those points would be the optimum point.

For the case of 21 step measurements, 9 points would be between two adjacent extrema (Fig. 3.10b), corresponding to distances of 0.14 of the wavelength or 104˚. If the middle point is chosen, the error in displacement would be less than 1.2% for the first median and 0.6% for the second one. The worst case scenario for finding the median would be when the starting point is right after one of the extrema. In this case, 17 steps would be required to find the correct median. However, the steps chosen for this experiment are fairly small. For a faster result with larger acceptable error, larger steps could be chosen.

The actual measurements are then carried out at the optimum initial angle. This

technique would eliminate the need for imbalance correction, and significantly reduces the error due to IQ imbalance.

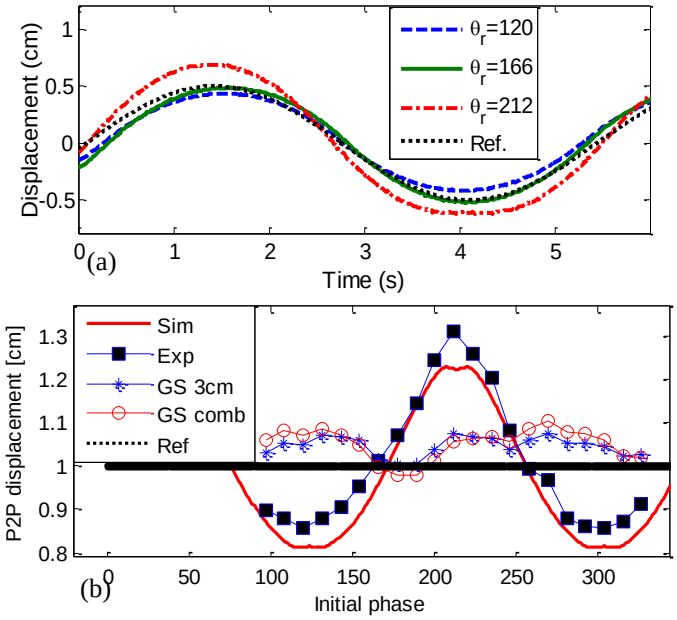

Fig. 3.10 (a) Time-domain signals with relative initial phase of 120˚, 166˚, and 212˚; (b) Peak to peak displacement for various initial phases comprises of simulations (Sim), experimental values (Exp), experimental values corrected with Gram-Schmidt method employing 3 cm imbalance information (GS 3 cm), experimental values corrected with Gram-Schmidt method employing combined arcs resembling 3 cm imbalance information (GS comb), and the reference (Ref) displacement;

3.7 Imbalance Estimation/Compensation

For imbalance measurement, 3 cm or quarter-wavelength displacement is used, which covers 172.8˚ or 48% of the ellipse. Since long arcs are needed for a more accurate imbalance estimation, a set of short arcs (1 cm displacement) with different initial angles are combined. Initial 1 cm displacement and 10 shifted arcs, 2 mm apart, are combined to produce the equivalent of 3 cm displacement. The imbalance values obtained from the combined arcs are 12.68˚ phase and -0.54 dB amplitude imbalance, which are within the 0.78˚ and 0.19 dB of imbalance values obtained from the continuous 3 cm displacement arc.

The known phase and amplitude mismatch can be corrected using Gram-Schmidt (GS) method. GS orthonormalization is used with imbalance values obtained from the best ellipse fit of the large 3 cm displacement, and from the combined 3 cm arc. Fig. 3.10(b) shows the peak-to-peak displacement results when GS compensation method is used versus reference.

Table 3.2 summarizes the errors introduced in displacement measurement before correction and after correction with the Gram-Schmidt method. The correction values are derived from the 3 cm large displacement and the combined arc with 1 cm displacement. When no correction is made, average displacement error estimation is 12.5%, and can reach up to 31.3%. However, if the optimum initial angle is chosen, the error can be as low as 0.6%. If the GS correction method is used the average error would be about 5%. The results of GS correction using 48% of the arc (3 cm), and combined arc are very similar, with the largest difference of 3% for the maximum displacement error.

Error / Method	Average displacement error (%)	Maximum displacement error (%)	Minimum displacement error (%)
No correction	12.5	31.3	0.6
GS corrected using 3 cm displacement	4.8	7.7	0.5
GS corrected using combined arcs	5.2	10.6	0.4

Table 3.2. Average, maximum, and minimum errors introduced in displacement estimation before and after correction. Gram-Schmidt method is used for correction with 3 cm large displacement imbalance values and combined arcs from 1 cm displacement.

3.8 Discussion

This chapter presented a systematic study of Doppler radar channel imbalance distortion effects on physiological signals and proposed two new methods for accurate displacement estimation. The effects of amplitude imbalance, phase imbalance, and initial phase on physiological patterns, effective radar cross section estimation, displacement, and rate measurements are investigated through parametric simulations and experiments. Arctangent demodulation with center estimation was used to estimate the displacement. Radius adjustment was also explored to demonstrate how displacement accuracy is affected by radius estimation errors. It is demonstrated that amplitude imbalances of 2 dB or phase imbalances of 32° causes 20% displacement error, and that displacement error is sensitive to initial phase. The error has a periodic pattern for varying initial phase, and can be reduced to below 1% for optimum initial angle. Gram-Schmidt compensation method is also used to compensate the imbalance and the results are compared with initial phase measurements with no compensation. Similar small arcs which are used for initial angle measurements can be combined to accurately determine imbalance values. The difference between imbalance values obtained using this technique versus single long arc method has less than 1˚ phase and fraction of a dB amplitude deviation. Furthermore, it is demonstrated that heart rate errors as high as 25% can result for imbalances of 2 dB and 60°. Experimental data obtained using a high precision mechanical target confirms simulation results.

4. PACKET DOPPLER RADAR

Doppler radar motion sensing systems have been used to detect physiological movement since the 1970s [13]. Over the past decade, the falling cost and reduced size of electronic components required to create Doppler radar sensors have enabled numerous technological advances, including single-chip integration [34] and novel applications, such as wearable [90], contact [91], and non-contact physiological monitoring [4]. In addition, the advent of integrated low-power microprocessor/RF-transceivers provides a new platform for a combination of sensing, processing and communications [34] which can form the core of a wireless smart sensor network for applications such as "smart building" systems.

Detection of human subjects using Doppler radar based on heart signals was proposed in [92]. This chapter explores the feasibility of Doppler radar detecting respiratory signals using packet radar. Packet radar can be employed as a promising solution for coupling and channel imbalance distortion. The system was tested with both a mechanical target and a human subject, demonstrating that periodic motion can be accurately detected using this low-cost, low-power system.

4.1 System-On-Chip

Non-invasive detection of vital signs, such as heart rate and respiration rate, is possible using a radar microwave system, due to a Doppler shift caused by body movements during respiratory and circulatory contractions and expansions. According to Doppler theory, the received signal from an object with a periodic movement contains the same frequency, but with a time varying phase $\emptyset(t)$.

Doppler radar motion sensing systems typically send a continuous-wave signal, which is reflected off a target and then demodulated in the receiver. To lower the power consumption for the system, the signal is sent intermittently rather than using continuous-wave transmission. As long as the signal repetition rate is significantly higher than the rate of measured periodic motion, periodic motion can be recovered with sufficient accuracy.

A system-on-chip is an integrated circuit (IC) that is composed of all the elements of computer or other electronic systems into a single chip. It may have analog, digital, mixed-signal, and radio frequency functions in one chip substrate. SoCs are popular in low-power system design systems such as mobile electronics.

An alternative to SoC is a system-in-package (SiP), SiPs consist of a number of chips in a single package [93]. A typical SoC contains:

- A microcontroller, microprocessor, or digital signal processor (DSP) core(s).
- Memory blocks
- Timing sources such as oscillators and phase-locked loops
- Peripherals such as counter-timers, real-time timers and power-on reset generators.

- External interfaces including industry standards such as USB, FireWire, Ethernet, USART, or SPI.
- Analog interfaces including ADCs and DACs.
- Voltage regulators and power management circuits.
- May include radio frequency circuits for wireless capability

For this project a SoC was chosen that has an RF transceiver integrated for the purpose of physiological monitoring. Since power consumption for portable devices and cost for wide adaption of the device are key factors, the CC2530 SoC from Texas Instruments was selected.

4.1.1 CC2530

The SoC CC2530 IEEE 802.15.4 compliant RF transceiver was employed as a signal source for radar. TI CC2530 uses ZigBee technology, which is a short-range, low-power, low data rate, low-cost wireless network technology. It combines the performance of a leading RF transceiver with an industry-standard enhanced 8051 microcontroller unit, in system programmable flash memory, and 8-KB RAM. This chip has different operating modes, making it suitable for systems where low power consumption is considered [94]. Fig. 4.1 shows the block diagram of the chip. The modules can be roughly divided into one of three categories: CPU- and memory-related modules, modules related to peripherals, clocks, and power management, and radio-related modules.

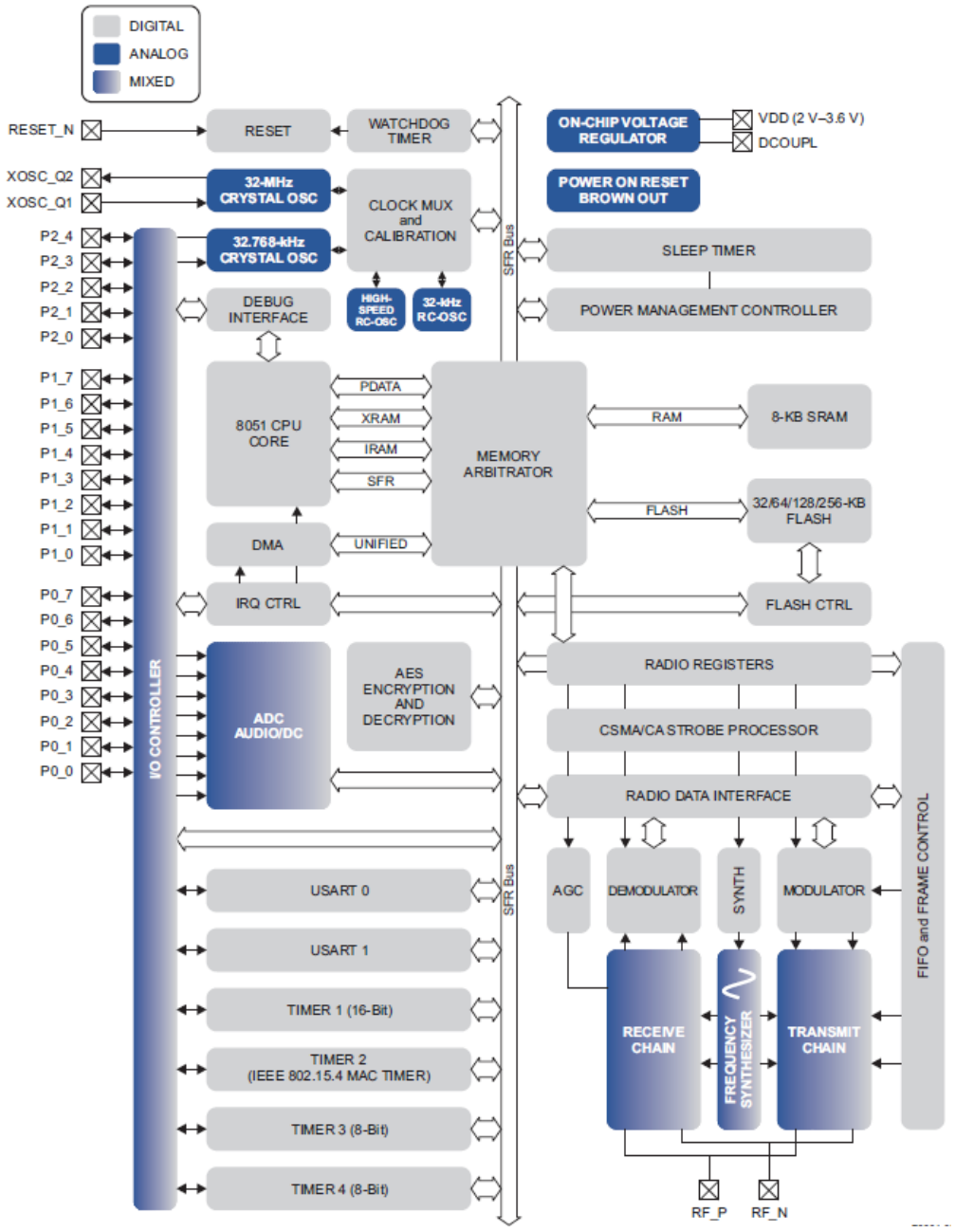

Fig. 4.1 CC2530 block diagram

The modulation format for the TI chip CC2530 is offset – quadrature phase shift keying (O-QPSK) with half-sine chip shaping. This is equivalent to MSK modulation. Each byte is divided into two symbols, 4 bits each. Each symbol is mapped to 1 out of 16 pseudorandom sequences, 32 chips each. The chip period is 1μs. Finally, the chip

sequence is transmitted at 2 Mchips/s. The chip has multiple-access capability and uses carrier sense multiple-access with collision avoidance [94].

The CC2530 chip is packed with features and has been used for home/building automation, lighting systems, industrial control and monitoring, low-power wireless sensor networks, consumer electronics and health care. However, this is the first time it is being used for wireless physiological sensing.

4.1.2 System Setup

Fig. 4.2 shows the block diagram of the system. A Minicircuits ZFSC-2-2500 coupler was used to split the signal source output into the transmitter antenna and local oscillator paths with a 90° phase difference. The Antenna Specialist (ASPPT2988) antenna was used with 8 dBi gain and 60° E-plane beamwidth for the transmitting and receiving antenna. Both a human subject and a mechanical moving object with periodic movements were used as targets for measurements. The frequency of the mechanical object's periodic movement was 0.13 Hz, and had a linear periodic mechanical movement of about 17 mm. Fig. 4.3 shows the artificial moving target simulating respiratory motion, which is used for measurements. The usable range depends on several factors, such as transmitting power, antenna characteristics, and oscillator phase noise. In both cases the target was placed one meter away from the antennas. The human subject was in the seated position.

The received signal, which is scattered form the target, is fed into a Minicircuits ZFM4212 mixer. It was mixed down to baseband, using a small portion of the transmitted signal as a local oscillator. A Stanford Research System Model SR560 Low-Noise Amplifier is used for amplification and filtering. The mixer's output is amplified by a

factor of 200, and subjected to 6 dB/octave high-pass filtering at 0.03 Hz to remove DC offset. Then, 6 dB/octave low-pass filtering with a 30 Hz cutoff frequency is applied. Finally, the signal is recorded by a TI DAQ9801 data acquisition device to the PC with a sampling rate of 1 kHz. Measurements for both the mechanical stage and human subject were made in an anechoic chamber. Measurements on human subjects were done under IRB protocol number CHS 14884.

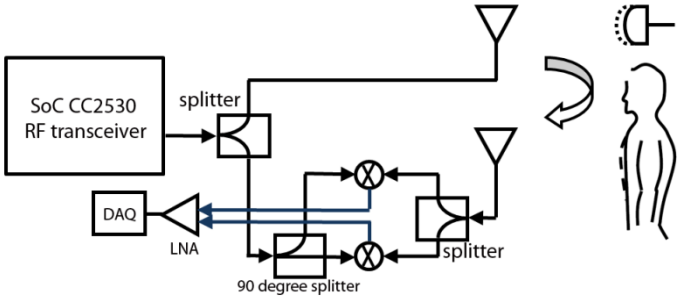

Fig. 4.2 Block diagram of the Doppler radar system using TI CC2530 SoC.

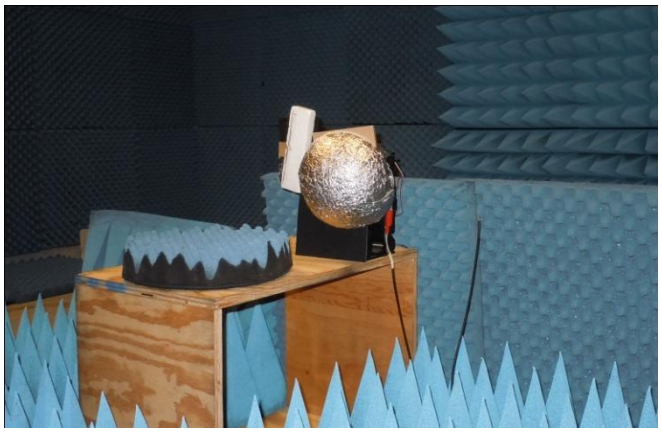

Fig. 4.3 Mechanical target with periodic motion simulating respiratory movements.

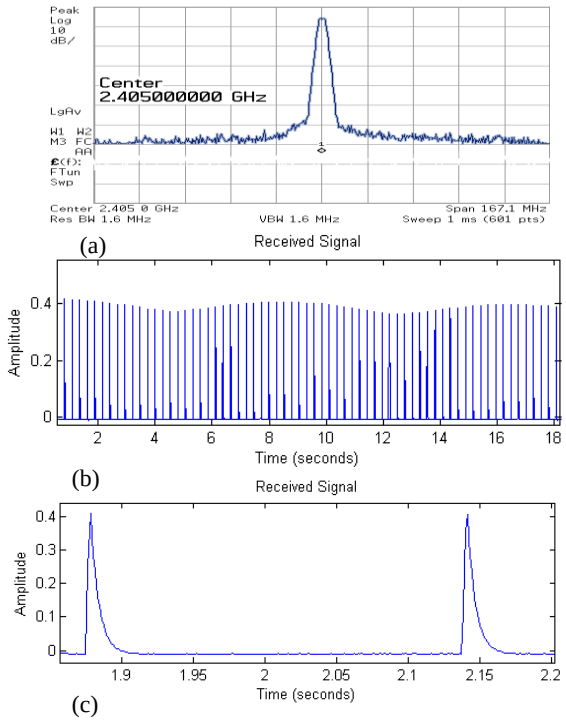

Fig. 4.4 (a) Transmitted signal spectrum, IEEE 802.15.4 channel 11 with 2.405 GHz center frequency (b) Received signal modulated by the respiratory motion (c) Two consecutive pulses of received signal.

4.1.3 Experimental Results and Discussion

The frequency spectrum of the transmitted signal is shown in Fig. 4.4(a). The center frequencies for the 16 channels, which are defined by IEEE Standard 802.15.04, begins at 2.405 GHz and ends at 2.480 GHz. Channel 11 has been used in measurements with a center frequency of 2.405 GHz. The power of the transmitted signal is -4 dBm. The average power consumption of the chip with its evaluation board is 17 mW.

Reflections from moving targets will results in phase/frequency shifts, while reflections from stationary clutter only result in DC offset. Phase shifts at the reflection surface also cause DC offset. RF interference is not phase correlated with the signal; thus, it only increases the DC offset of the output signal. Fig. 4.4(b) shows the LNA's output in which the amplitude of the signal is modulated by respiratory motion. Two consecutive

pulses are depicted in Fig. 4.4(c). The pulse period is about 256 ms, corresponding to a pulse repetition frequency of 3.77 Hz. Output signals are post-processed using MATLAB to extract the envelope and perform frequency-domain analysis for finding the target's periodic movement rate.

Due to the pulsed nature of the received signal, common methods of envelope detection such as Hilbert transform, and squaring and low pass filtering were not successful. Fig. 4.5 shows the nature of signals received in baseband. The block diagram for finding the target periodic movement is shown in Fig. 4.6. Filtered respiration signals are fed into the local maximum algorithm with a neighborhood threshold, which is selected based on signal amplitude. A point is considered a maximum peak if it has the maximal value, and was preceded by a value lower by Δ. The time instances when peaks are greater than their neighborhood by the threshold are stored in an array. The peak values and the time at which they occur are stored in separate arrays.

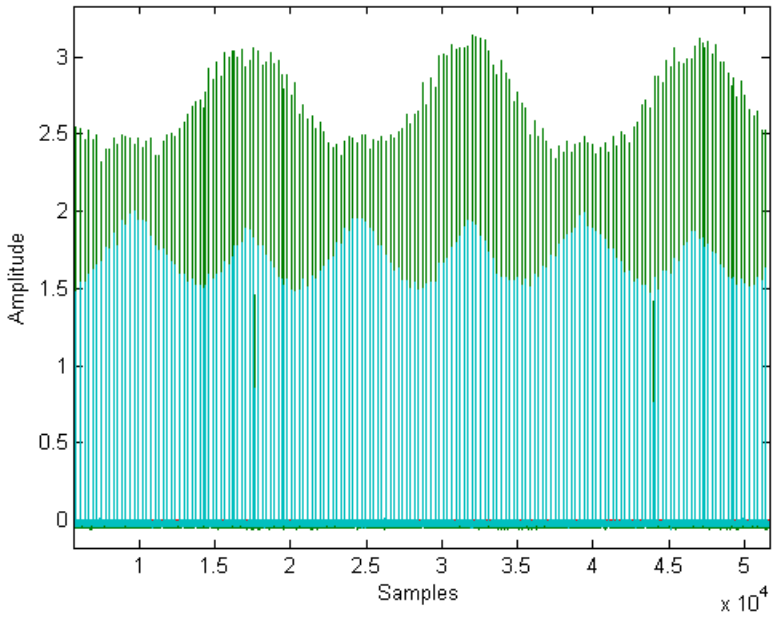

Fig. 4.5 I and Q signals received in baseband of packet radar.

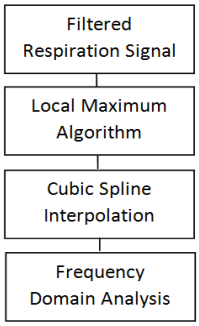

Fig. 4.6 Block diagram of the algorithm for extracting the target movement rate.

Fig. 4.8(a) shows the peaks which are detected by the algorithm. As the peak signals are not equally spaced, the envelope is not uniformly sampled by the peaks. Fig. 4.7 shows the deviation from the average sampling point. In this figure the worst sampling deviation in an 18-second window could be as high as 90 samples. Therefore, it is necessary to perform an interpolation to achieve a uniformly sampled signal before carrying out frequency-domain analysis. There are different interpolation methods, such as piecewise constant interpolation, linear interpolation, polynomial interpolation, and spline interpolation. Cubic spline interpolation technique is used for this purpose, which gives a smoother waveform than linear interpolation, and does not suffer from Runge's phenomenon associated with high degree polynomials. Fig. 4.8(b) illustrates the result of the interpolation. After reconstructing the signal, FFT was applied to calculate the subject's movement rate during the measurement interval. Fig. 4.8(c) shows periodic movement rate of the mechanical target (f = 0.13 Hz).

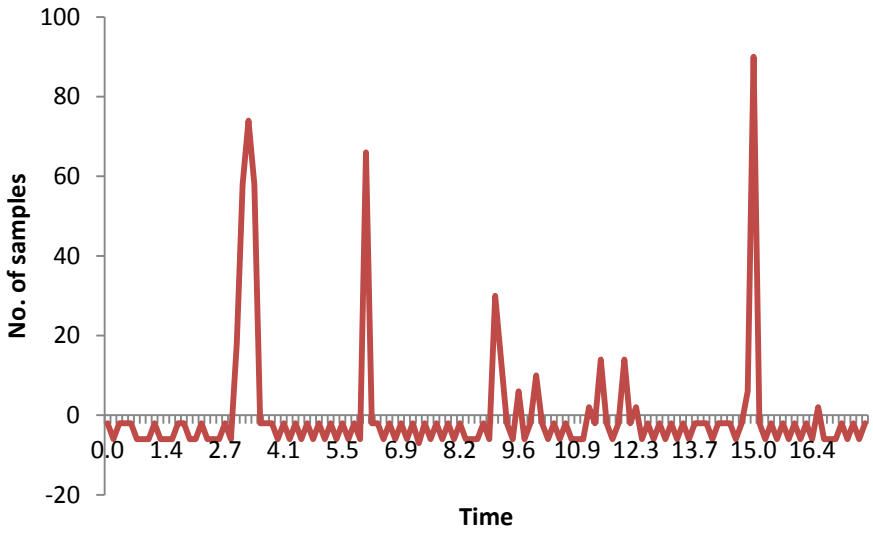

Fig. 4.7 Sampling uncertainty in packet radar; in this particular recording the shift from the average sampling point could be as high as 90 samples.

Fig. 4.9 depicts results of the experiment with a human subject. The upper trace shows the recorded respiration effort signal using a piezoelectric sensor as a reference. The traces in Fig. 4.9(b) and (c) are the envelope and interpolated version of the demodulated received signal. DC drift in Fig. 4.9(b) and (c) may be due to a slow moving clutter in the background. The bottom traces illustrate the respiration rate of a human subject (f = 0.29 Hz). Respiration rate is successfully extracted, and is in accordance with the reference signal.

The main advantage of the system is lower power consumption by intermittent transmission rather than continuous-wave transmission. It is interesting to note that the transmitted data are packets of information, instead of a single-tone sinusoidal signal. Although the data content is not extracted and only the amplitude modulation on data is of importance in this application, the other RF sources in the environment, such as WiFi sources which are readily available, can be employed as a signal source regardless of what information is transmitted. Another benefit is using low-cost off-the-shelf RFICs for

wireless respiratory measurements, and occupancy detection. The cost of the off-the-shelf System-on-Chip is on the order of $10.

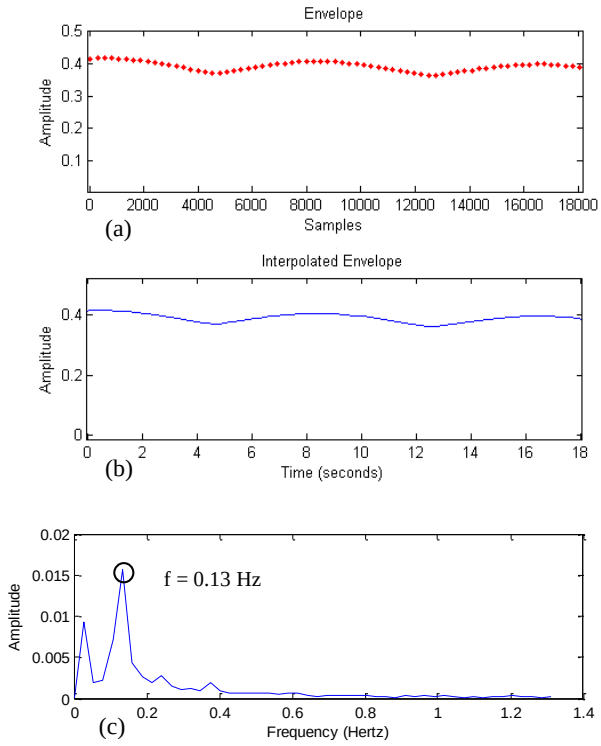

Fig. 4.8 (a) Envelope of the received signal reflected from the mechanical target (b) interpolated version of the peaks which are not evenly distributed (c) frequency-domain analysis, mechanical subject periodic movement's rate (f = 0.13 Hz).

Respiratory motion was selected for occupancy sensor subject detection for two reasons. It is an order of magnitude larger than chest motion due to heartbeat and thus possible to detect with lower power and lower system complexity. It also enables detection of stationary human subjects. On the other hand, reliable stationary subject detection is the main limitation of current occupancy detection systems based on ultrasonic or infrared sensors.

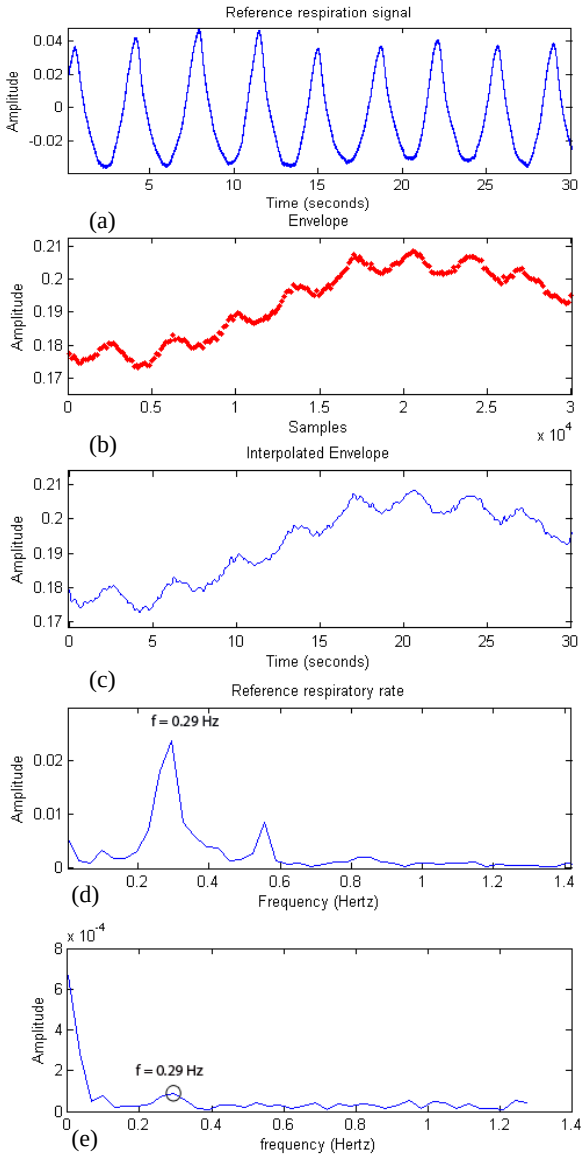

Fig. 4.9 (a) Respiration effort signal recorded using piezo-electric sensor (b) envelope of the demodulated radar signal containing chest periodic motion (c) interpolated version (d) spectrum of the piezo-electric reference;(e) spectrum of the interpolated Doppler radar respiratory signal. The respiratory rate is successfully extracted from interpolated received signal (f = 0.29 Hz).

4.2 AC/DC Coupling Effect on CW and Packet Radar

AC coupling is another significant distortion source for Doppler radar signals. In this section, the effects of AC/DC coupling are examined for CW and pulse radar. Radar performance is compared using a mechanical target that simulates respiratory motion.

While both systems can extract the rate of motion with high accuracy, it is demonstrated that pulse radar performance is not affected by AC coupling, which causes distortion in a CW system.

Fig. 4.10 shows the block diagram of a quadrature Doppler radar used to make measurements. The SoC CC2530 IEEE 802.15.4 compliant RF transceiver was employed as signal source for radar. A Minicircuits power splitter, part ZFSC-2-2500, provided 17 dB of isolation between input and output signals and was used to split the signal source output into the transmitter antenna and local oscillator paths with a 90° phase difference. It is necessary to use the same signal source for the transmitter and receiver's local oscillator to benefit from coherent reception and range correlation.

A commercially available Antenna Specialists ASPPT2988 2400 MHz antenna was used with 8 dBi gain and 60° E-plane beamwidth for transmitting and receiving. A mechanical moving object with periodic movements is used as a target for the measurements. The motion was sinusoidal with a frequency of 0.2 Hz and trapezoidal with 0.1 Hz frequency, and the amplitude was approximately 10 mm. The target was placed two meters away from the antennas. These measurements were performed in an anechoic chamber at University of Hawaii Laboratories.

TI CC2530 is used as a signal source. For emphasis, it should be noted that the transmitted data are packets of information instead of single-tone sinusoidal signal. Although the data content is not extracted, and only the amplitude modulation on data is of importance in this application, it shows a promising approach for employing readily available RF sources in the environment.

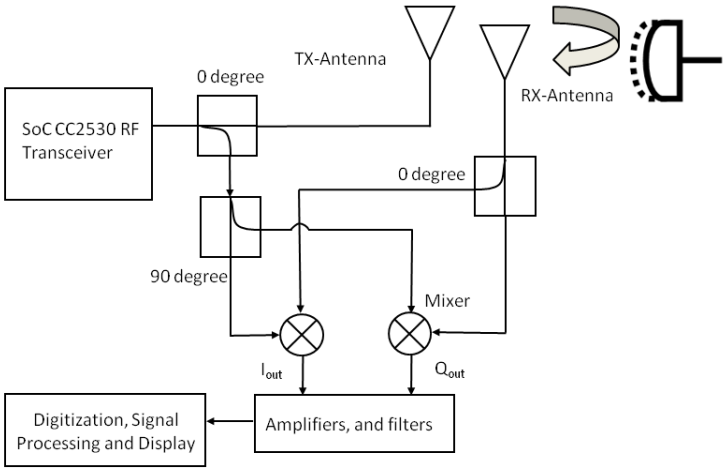

Fig. 4.10 Block diagram of a quadrature Doppler radar system. The LO signal is divided by a two-way 90 power splitter to get two orthonormal baseband signals (I and Q), which can be combined by linear demodulation.

The received backscattered signal from the target is fed into a Minicircuits ZFM4212 mixer. It was mixed down to baseband, using a small portion of the transmitted signal as a local oscillator. The baseband signals were filtered, and amplified with a series of Stanford Research Systems SR560 Low Noise Amplifiers. The baseband signal for AC coupling mode was initially filtered with a 6 dB/octave high-pass filter with a 0.03 Hz cutoff frequency, and was then filtered with a 6 dB/octave low-pass filter with a cutoff frequency of 10 Hz for continuous mode, and 1 kHz for intermittent transmission to remove the DC component and minimize out-of-band noise and aliasing error. Then, the signal was amplified by a factor of 100. The initial high-pass filtering is omitted for DC coupling mode. Therefore, the DC content of the signal is preserved in the output signal.

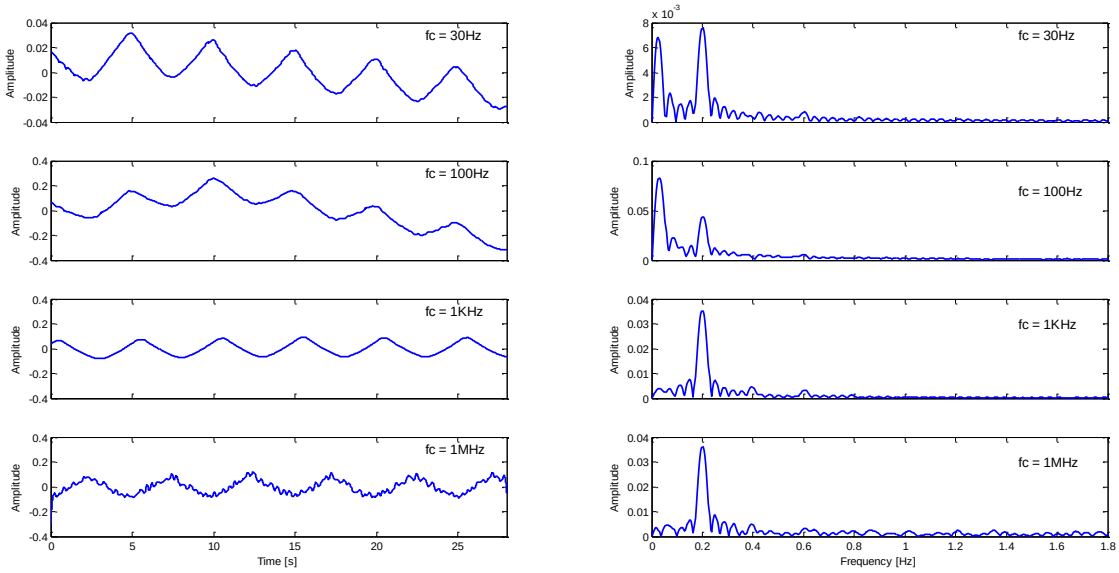

Fig. 4.11 Nonlinear effects of the cutoff frequency on the signal in the packet mode. Time-domain representation of the signal (left) for 30, 100, 1 kHz, and 1 MHz cutoff frequencies. Corresponding frequency spectrums are illustrated on the right.

Different cutoff frequencies were used for low-pass filtering in continuous mode and packet mode. Due to the pulsed nature of the received signal in intermittent transmission, cutoff frequency is increased. Otherwise, nonlinear distortions will be introduced. Fig. 4.11 shows nonlinear distortions for different cutoff frequencies. In these measurements, target motion was sinusoidal with a frequency of 0.2 Hz. As illustrated in Fig. 4.11(a) and Fig. 4.11(b), for 30 Hz and 100 Hz cutoff frequencies, DC drift is obvious in the baseband signal, which introduces a low-frequency peak in the frequency spectrum. However, as shown in Fig. 4.11(c) and Fig. 4.11(d), the problem is resolved. 1 MHz sampling is very large and it introduces only more noise due to the higher bandwidth. To alleviate this problem, a 1 kHz cutoff frequency was chosen (Fig. 4.11(c)). Finally, the signal is recorded by a TI DAQ9801 data acquisition device to the PC with a sampling rate of 4 kHz for the pulse mode and 1 kHz for continuous mode.

The center frequencies for the 16 channels, which are defined by IEEE Standard

802.15.04, begins at 2.405 GHz and ends at 2.480 GHz. Channel 11 has been used in our measurements with a center frequency of 2.405 GHz. The pulse period for the packet mode is about 256 ms with 1% duty cycle.

The target periodic movement was clearly visible after the filtering stage, but it could be better resolved with an additional digital filtering stage to attenuate high frequency components due to high cutoff frequency for the pulse mode.

4.2.1 Experimental Results

The effects of AC coupling were tested in CW and pulse modes using the trapezoidal target motion at a frequency of 0.1 Hz. The average transmitted power was 4 dBm in both modes, and the distance to the target was 2 meters. The I and Q received signals, before demodulation, for different transmission modes are depicted in Fig. 4. The main difference for DC coupling is the omission of an initial high-pass filter with a 0.03 Hz cutoff frequency for removing the DC portion of the signal. Therefore, the DC content of the signal is preserved. Fig. 4.12(a) and (b) show continuous-wave I and Q channels for different coupling modes, while Fig. 4.12(c) and (d) shows the I channel of the AC/DC coupled received signal in pulse mode. For the pulse mode, filtered received signals are fed into the local maximum algorithm as described in [39] to find peaks. Since the respiration rate is much lower than the pulse repetition frequency, the signal is essentially sampled with PRF as shown in Fig. 4.12(c) and (d). Then, interpolation is performed to achieve a uniform signal before demodulation and carrying out frequency-domain analysis [39].

Principal Component Analysis (PCA) was used to perform linear demodulation of the

quadrature channels. Linearly demodulated received signals in time domain with AC/DC coupling for two different modes are shown in **Error! Not a valid bookmark self-reference.**. The DC portion is removed digitally for better illustration in **Error! Not a valid bookmark self-reference.**(a), which shows the AC and DC coupled output for CW mode. As expected, AC coupling distorted the received signal and caused a longer response time. For a high-pass filter with a single pole at 0.03 Hz, the settling time will be 12 seconds, which means it will take 12 seconds before the system can produce meaningful output.

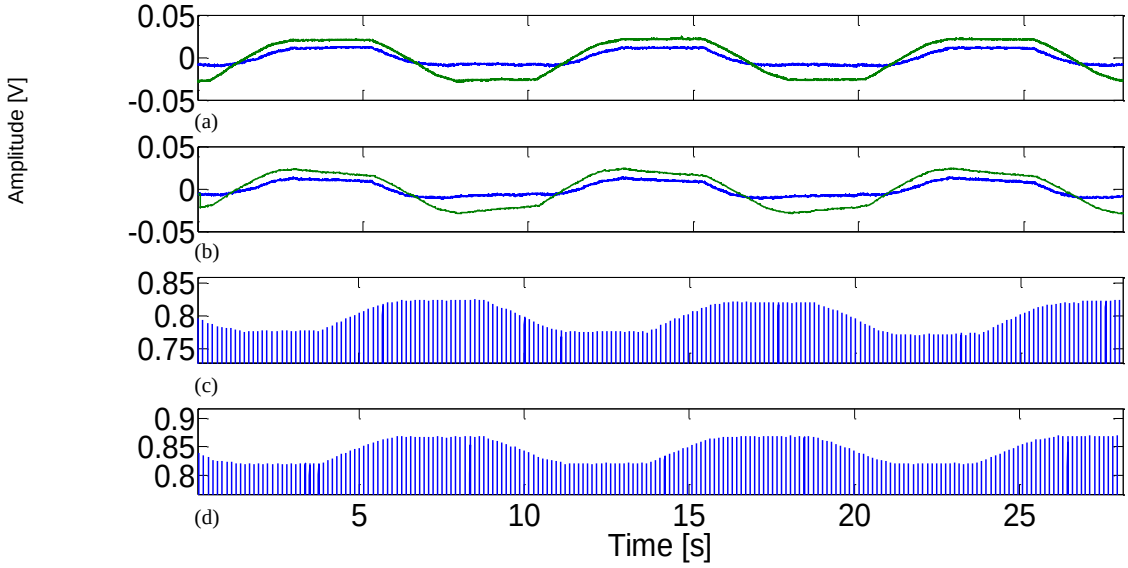

Fig. 4.12 Received signals before demodulation: (a) DC-coupled CW I and Q signals, (b) AC-coupled CW I and Q signals, (c) DC-coupled I channel in pulse mode, and (d) AC-coupled I channel AC in pulse mode.

Fig. 4.13(b) shows the AC and DC coupled outputs for packet radar. The reason that packet radar is not affected by coupling is illustrated in Fig. 4.14. Each individual pulse is affected by AC coupling. However, only one sample of each pulse (largest value) is considered in signal reconstruction. Therefore, the overall envelope of the signal is not affected by AC coupling.

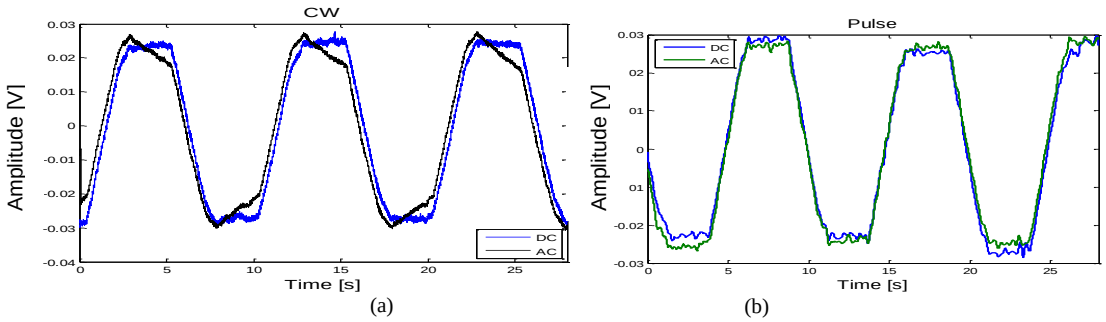

(a) (b)

Fig. 4.13 AC and DC coupled outputs for CW radar (a), and pulse radar (b).

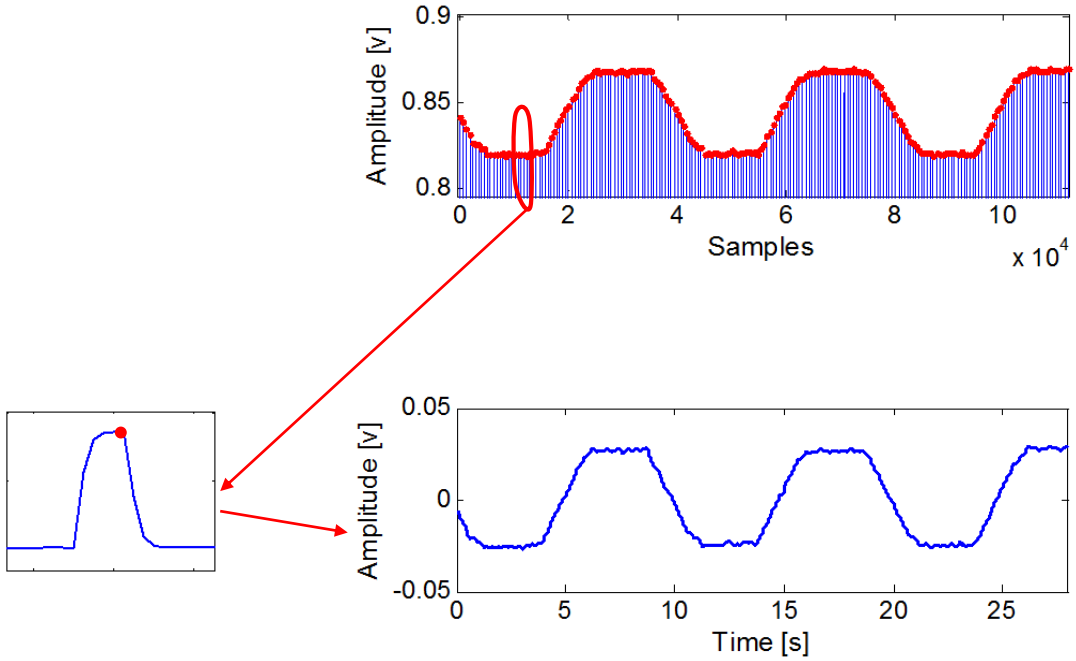

Fig. 4.14 AC coupling effect on packet radar

4.3 Packet Radar Spectrum Recovery for Physiological Signals

Continuous-wave (CW) radar systems transmit electromagnetic radiation at all instances while a pulsed radar system transmits signals intermittently and has wider bandwidth because of the pulses. CW radar can measure the instantaneous rate-of-change in the target's range and has a simpler topology; the narrow-band nature of the CW radar

alleviates the requirements for the filters at each stage of the receiver and signal processing is straightforward for calculating velocity or displacement.

However, constant transmitting and receiving makes the separation of reflections impossible and increases power consumption. Leakage and clutter add unwanted DC offset and low-frequency noise [52]. Pulse radar can discriminate temporal leakage and echoes. Another advantage of pulsed radar is the ability to measure target range in addition to velocity [22]. Packet radar is employed to get respiratory rate in the previous section. However, due to the non-uniform sampling rate of the receiver, a computationally intensive method is used to reconstruct the signal and extract the rate.

In this section, the use of pulse radar and using packet data transmission is explored for detection of periodic motion using an alternative method with less computational cost. A frequency-domain method based on subtraction of the clutter is proposed which is more straightforward and alleviates the signal processing part in the receiver. This method is used for recovering the periodic motion of the target, which is buried in noise. Both the simulations and experimental results using the mechanical target simulating respiratory and heart movements demonstrate the proof of concept.

4.3.1 System Setup

A block diagram of a quadrature Doppler radar which is used to make measurements is shown in Fig. 4.15. A CC2530 RF transceiver from Texas Instruments was employed to transmit a signal at 2.405 GHz using ZigBee technology.

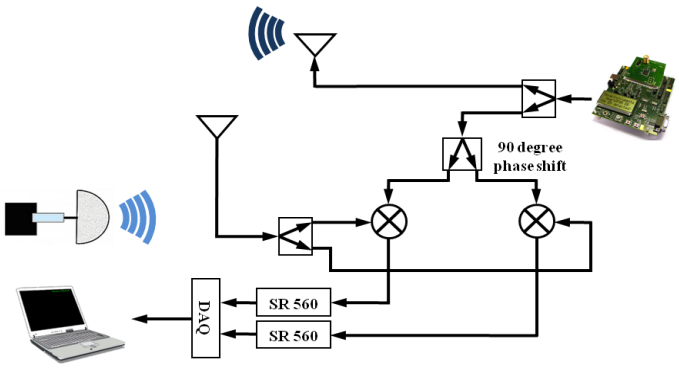

Fig. 4.15 Block diagram of a quadrature Doppler radar system. The LO signal is divided by a two-way 90 power splitter to get two orthonormal baseband signals (I and Q).

A Minicircuits power splitter, part ZFSC-2-2500, provided 17 dB of isolation between input and output signals and was used to split the signal source output into the transmitter antenna and local oscillator paths with a 90° phase difference. For reducing baseband residual phase noise, the same signal source is used for the transmitter and receiver's local oscillator. The Antenna Specialist (ASPPT2988) antenna was used with 8 dBi gain and 60° E-plane beamwidth for transmitting and receiving.

The received signal is mixed down with a Minicircuits ZFM4212 mixer. After down conversion, the baseband signals are filtered and amplified with a Stanford research low-noise amplifier SR-560. The physiological signals' frequency is fairly low, around 0.1 to 2 Hz. However, the filter bandwidth is set to 1 kHz, due the large bandwidth of received pulses. Then, the data is recorded by a data acquisition device with a 4 kHz sampling frequency.

A mechanical target with periodic movements simulating heart signal has been employed as a target for measurements. The precision single-axis linear stage is from Galil motion control (CDS-3310) [95] with a pulse-width modulation (PWM) driver. The frequency of the mechanical object periodic movement was 1 Hz. The radar usable range

depends on several factors, such as transmitting power, antenna characteristics, and oscillator phase noise. For the measurements, the target was placed one meter away from the antennas.

4.3.2 Simulation Results

Reflections from moving targets will results in phase/frequency shifts. Depending on the radar pulse width and target's Doppler frequency, it may be possible to detect the Doppler frequency shift within a single pulse or multiple pulses as discussed in Chapter 2. Since vital signs are low frequency in nature, multiple pulses are needed to detect the Doppler shift.

First, a respiratory signal with 0.2 Hz frequency is simulated. Since the Doppler frequency is much smaller than the pulse repetition frequency of the pulse radar, the Doppler is actually sampled at the pulse repetition frequency (PRF) according to the following equations:

$$b_{Ie}[n] = b_I(\frac{n}{prf}) \tag{4.1}$$

$$b_{Qe}[n] = b_Q(\frac{n}{prf}) \tag{4.2}$$

where b_I and b_Q are the in-phase and quadrature components of the baseband signals; and b_{Ie} and b_{Qe} are the in-phase and quadrature samples of the envelope. As shown in Fig. 4.16(a), the envelope of the signal carries the Doppler frequency shift. The spectrum of the received signal is depicted in Fig. 4.16(b). The spikes in the spectrum are due to the pulse repetition frequency. However, the Doppler frequency is detectable close to DC (0.2 Hz), or even close to the first couple of harmonics, which are moved from 4 Hz

(PRF) to 3.8 Hz and 4.2 Hz due to the Doppler effect.

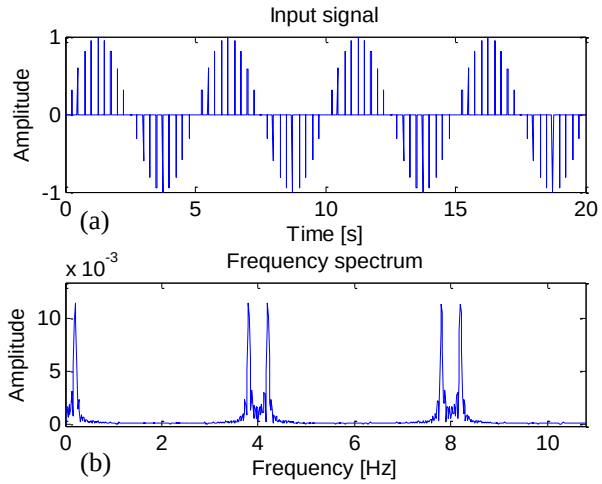

Fig. 4.16 (a) Simulated received signal modulated by respiratory signal; simulated respiratory rate is 0.2 Hz (b) spectrum of the received signal, pulse repetition frequency is 4 Hz and Doppler frequency shift is 0.2 Hz.

4.3.3 Experimental Results and Discussion

Fig. 4.17(a) shows the received signal after amplification, filtering, and digitization. The amplitude of the signal is modulated by the mechanical target motion. The pulse repetition frequency is 7.4 Hz, which is large enough for detecting the target's frequency of 1 Hz, in this case. After amplification, band-pass filtering, and digitalization, the output signals are post-processed using MATLAB to extract the target's periodic movement rate. Fig. 4.17(b) shows the spectrum of the received signal when the mechanical target is in motion. Fig. 4.17(c) shows the recorded spectrum when there is no movement in the room.

The Doppler effect can be observed in the envelope of the signal, as amplitude modulation on the pulses. The multiple access scheme of the chip causes the non-uniform distribution of the peaks. To reconstruct the signal envelope, computationally intensive interpolation is needed [39]. After reconstructing the signal, FFT is applied to calculate

the target's movement rate during the measurement interval. Fig. 4.18(a) shows the reconstructed envelope, according to the method which is described at the beginning of this chapter, and Fig. 4.18(b) shows the spectrum of the signal. Doppler frequency at 1 Hz is noticeable.

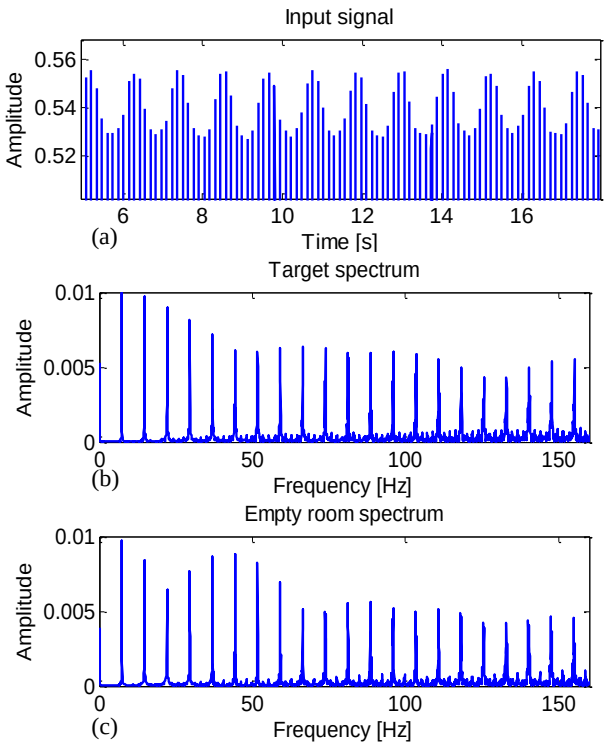

Fig. 4.17 (a) Baseband received signal in time domain; periodic movement of the mechanical target modulated the amplitude of the received signal (b) spectrum of the received signal; pulse repetition frequency is 7.4 Hz. (c) recorded spectrum of the empty room with no target motion

However, an alternative method for detecting the target's periodic motion is to investigate the spectrum of the raw received signal before reconstructing the envelope, which is computationally more effective. As opposed to simulation, due to jitter in the receiver or non-uniform sampling, the target rate is buried in noise and cannot be extracted directly.

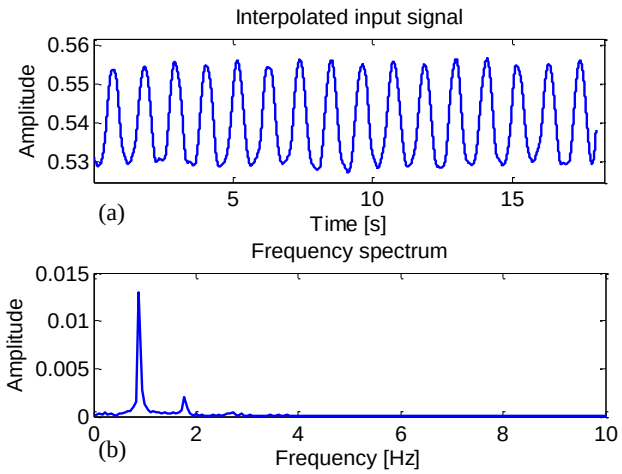

Fig. 4.18 (a) Envelope of the received signal reflected which contains the target's rate (b) spectrum of the reconstructed signal (f = 1 Hz).

To resolve this issue, Fourier Spectral Subtraction is employed, which is an effective method for additive noise reduction [96]. First, the Fourier spectrum without the target has been recorded, as shown in Fig. 4.17(c). Then, the experiment is conducted with the target in the range of the radar (Fig. 4.17(b)). Finally, Fourier spectrum of the moving subject is subtracted from the Fourier spectrum of the empty room. The baseband signals in time and frequency domain can be represented by:

$$b_T[n] \xleftrightarrow{DFT} B_T(e^{j\omega}) \tag{4.3}$$

$$b_E[n] \xleftrightarrow{DFT} B_E(e^{j\omega}) \tag{4.4}$$

$$B_{SS}(e^{j\omega}) = B_T(e^{j\omega}) - B_E(e^{j\omega}) \tag{4.5}$$

where $B_T(e^{j\omega})$ is the Discrete Fourier Transform (DFT) of the target, $B_E(e^{j\omega})$ is the DFT of the empty room's baseband signal, and $B_{SS}(e^{j\omega})$ is the spectral subtraction output. Fig. 4.19 shows the spectral subtraction which shows the target's periodic motion at 1 Hz (1st marker), which was buried in noise before subtraction. The periodic motion is also detectable at both sides of the pulse repetition frequency at 6.4 and 8.4 Hz, which are illustrated with the 2nd and 3rd markers.

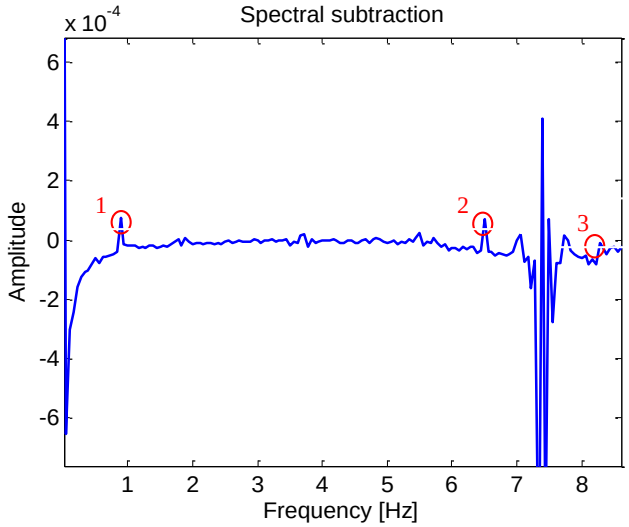

Fig. 4.19 The spectrum of the received signal is subtracted from the spectrum with no target in the environment. Target's rate is visible at 1 Hz (1st marker), as well as, around pulse repetition frequency at 6.4 Hz and 8.4 Hz (2nd and 3rd markers).

4.4 Conclusion

Low-cost, low-power, packet Doppler radar was demonstrated using an off-the-shelf SoC CC2530 as a vital sign sensor. It has been shown that periodic motion can be extracted using intermittent data transmission instead of sending a CW signal which consumes more power. Digital signal processing techniques have been employed to process baseband signals. One of the challenges in homodyne CW Doppler radar physiological monitoring systems is a large DC offset in baseband outputs. AC coupling is a common solution; however, it distorts the baseband signal. Packet radar is investigated to overcome this issue. The performance of the packet radar is affected by receiver bandwidth, and the minimum-required bandwidth is used to eliminate DC drift and the associated low-frequency component in the output spectrum. The performance of CW and packet radar is compared for AC and DC coupling. While the AC coupled signals in CW mode are significantly distorted, the effects of AC coupling on the pulse

radar were demonstrated to be negligible. Frequency-domain analysis is also an important part of the physiological Doppler radar for estimating the heart and respiratory rate. The spectrum subtraction method is investigated for estimating the rate. This approach reduces computation complexity as compared to the interpolation method, and provides accurate frequency estimation of periodic target motion.

5. PULSE LOW-IF DEMODULATOR

Recent advances in Doppler radar physiological monitoring has taken this technology from a research-only tool to a commercially available device [97]. Continuous-wave (CW) Doppler radar homodyne receiver architecture is the common method for detecting physiological motion [74]. However, two categories of artifacts degrade the system performance. Interference that is induced due to antenna shaking or caused by subjects' fidgeting are environmentally-related artifacts which are discussed in [67] and [98], where solutions have been introduced to enhance the signal quality in these circumstances. Low-frequency noise, null and optimum point, DC offset, and coupling effects are electrically-related degradations [31, 74]. The fact that vital signs are low-frequency in nature (usually in the range of 0.1 Hz to 1.5 Hz) makes it even harder to extract the respiratory and heart information for such a receiver. Pulse radar can overcome some of the limitations of conventional CW receiver, such as DC offset and the coupling issue, as demonstrated in chapter 4 [19]. Traditional pulse radar, with transceiver architecture similar to that shown in Fig. 5.1, is typically used for vehicular and weather forecast applications to measure range in addition to velocity [99].

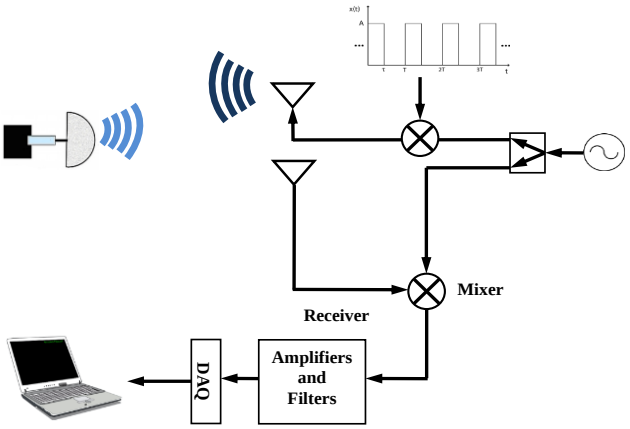

Fig. 5.1 Block diagram of a single-channel Doppler radar system. The CW source signal is mixed with a train of pulses to produce the required pulse signal. Portion of the CW source signal is used for receiver LO.

A low-intermediate frequency (IF) receiver is used in communication systems to avoid DC offset [100, 101]. CW Low-IF is a type of heterodyne receiver with an IF frequency low enough to be digitized by an ADC. This architecture is also suitable for detecting low frequency physiological signals, since it eliminates the DC offset and coupling issues, while lowering the noise floor which increases the SNR. Low-IF receivers also have the advantage of being single-channel without position sensitivity issues. Therefore, there would be no mismatch problem between the channels like with quadrature receivers. In [101], the benefits of the coherent Low-IF system, which includes an increase in range while reducing the emitted power, is discussed. However, the system will be more complex due to the addition of coherent reception to the system [64].

In this chapter, we combine benefits of pulse radar and low-IF demodulation techniques to demonstrate a simple, low-cost and effective hardware architecture which uses a computationally efficient physiological signal extraction that can yield vital signals [102]. Various pulse repetition frequencies, harmonics, signal shapes, and system architecture are investigated. By multiplying the CW source signal with a pulse signal

with pulse repetition frequency (PRF), the received down-converted spectrum is shifted from baseband to the PRF. Thus, pulse radar architecture with low-IF demodulation technique overcomes limitations of quadrature receiver architecture.

5.1 Simulation Results

Simulations were conducted in Matlab to test the feasibility of the proposed method. Fig. 5.1 illustrates the block diagram of the system for simulations and experiments. A train of pulses with a PRF of 4 Hz modulates the 2.4 GHz CW signal at the transmitting path. The backscattered signal is down-converted in the receiver side using the same 2.4 GHz CW signal for the local oscillator.

If the radar pulse width is long enough and if the target's Doppler frequency is high enough, it may be possible to detect the Doppler frequency shift on the basis of the frequency change within a single pulse. To be able to detect a Doppler shift within a single pulse width T, at least one cycle of the Doppler frequency f_d should fall within the pulse or $f_dT > 1$. However, this condition is not usually met when detecting respiration and heart signals, since the Doppler frequency f_d is generally much smaller than l/T. Thus, the Doppler effect cannot be observed within a single short pulse in this case [25]. Fig. 5.2(a) is more representative of the Doppler frequency for pulse-based physiological monitoring radar. The respiratory signal is modeled with a sinusoidal signal with 0.2 Hz frequency.

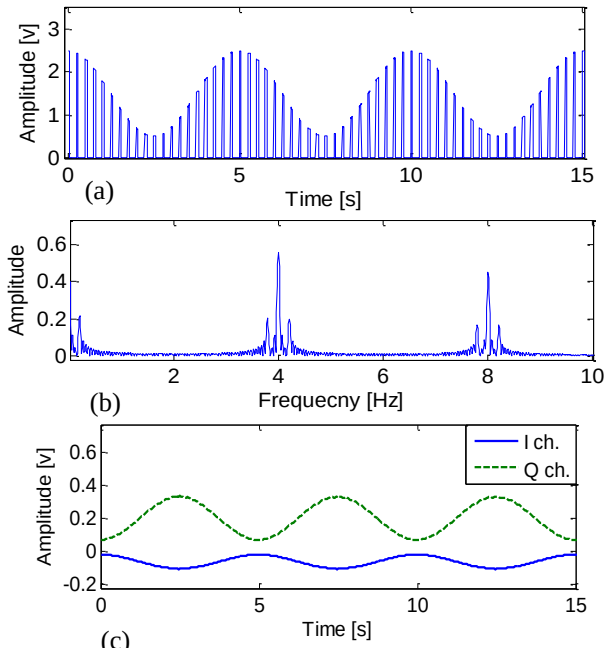

Fig. 5.2 (a) Sampled signal with a train of pulses with pulse repetition frequency of 4 Hz and twenty percent duty cycle; The Doppler shift is 0.2 Hz (b) spectrum of the signal; (c) Reconstructed I and Q components by using quasi low-IF method.

The envelope of the received baseband signal carries the Doppler frequency shift. There are multiple ways to demodulate the envelope. Due to the pulsed nature of the received signal, common methods of envelope detection like Hilbert transform or squaring and low pass filtering do not produce satisfactory results. One way is to detect the peaks of the pulses that are gone through amplitude demodulation. Since the peaks of the pulses are not equally spaced, it is necessary to do an interpolation before carrying out any frequency-domain analysis due to non-uniform distribution of samples in the time domain as explained in Chapter 4 [39]. Envelope extraction is essentially investigating amplitude modulation on the pulses, and also suffers from position sensitivity like single-channel receivers.

Another less computationally complex method is to use frequency-domain analysis without reconstructing the envelope. Fig. 5.2(b) depicts the spectrum of the pulse train.

The large peaks are due to the pulse repetition frequency. However, the smaller peaks, which are visible close to DC at 0.2 Hz or with a 0.2 Hz offset at harmonics, are clearly showing the Doppler effect. The block diagram for extracting the Doppler shift by investigating the spectrum is shown in Fig. 5.3. The down-converted signal is band-pass filtered with a sharp linear phase FIR filter. The pass-band of the filter is between 2 Hz to 6 Hz to pass only the first harmonic of the signal. Then, the filtered signal is multiplied by $e^{-j\omega t}$,where ω is $2\pi \times$PRF to bring the intermediate frequency, which is shifted from DC by PRF, back to the origin. After this multiplication, the signal would be a complex number. The signal is low-pass filtered to remove the unwanted portion of the spectrum. The real and imaginary parts of the complex signal, which represent the in-phase and quadrature components of the quadrature receiver, are illustrated in Fig. 5.2(c). It is interesting to note that the receiver in this design is single-channel. However, by using the low-intermediate frequency demodulation method, the advantages of a quadrature receiver are gained without having the associated complexity and issues, as explained in previous chapters.

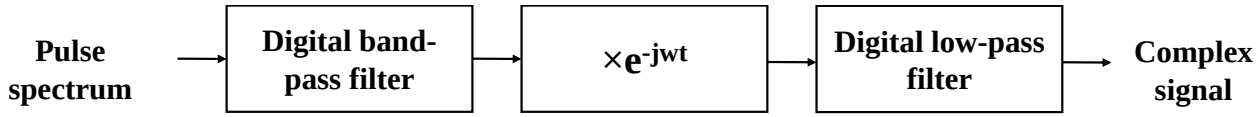

Fig. 5.3 Block diagram of Low-IF method for extracting Doppler information.

5.2 Measurement Setup

As illustrated in Fig. 5.1, an HP 83640B signal generator is employed as the signal source for radar, generating a continuous-wave 2.4 GHz signal with 10 dBm output power. The source signal is split by a Minicircuits ZFSC-2-2500 coupler between the

transmitter and receiver section. On the transmitter side, the signal is mixed with a train of pulses generated with an HP 33120A arbitrary waveform generator with variable constant pulse repetition frequency. The pulse train duty cycle is 20%. The pulse signal is connected to the IF port of the Minicircuit ZFM4212, which has a more suitable frequency response (DC-1300 MHz) for the pulse train. The RF port of the mixer is coupled to an Antenna Specialist (ASPPT2988) antenna with 8 dBi gain and 60° E-plane beamwidth.

On the receiver side, the backscattered signal is mixed down with the same LO. The down-converted signal is then filtered and amplified with a Stanford Research low-noise amplifier Model SR-560. The filter cutoff frequency is DC - 300 Hz. The Doppler shift for physiological signals is small, around 0.2 Hz - 2 Hz. However, due to the larger bandwidth of pulses, the corner frequencies are selected to be much larger (0.03 Hz - 3 kHz). The received baseband signals are recorded by a data acquisition device with an 8 kHz sampling rate.

A linear stage from Griffin Motion is programmed to have complex respiration and heart movement, as described in chapter 3, and trapezoidal motion. Both the mechanical target and human subject are 1 m away from the radar antenna and the frequency of the target is 0.15 Hz ~ 0.2 Hz for respiration and 1.25 Hz for heart signals produced by the mechanical mover.

5.3 Experimental results

A set of experiments were conducted to confirm the simulation results. Testing was done both with a mechanical target moving periodically, and with a human subject

breathing normally. The reflected 2.4 GHz signal is modulated by a train of pulses with PRFs ranging from 10 Hz to 100 Hz. The signals are down-converted and digitized after amplification and filtering. Fig. 5.4(a) shows the baseband signal recorded by ADC, obtained with a human subject. The amplitude of pulses is clearly modulated by the respiration signal. After digitization, the output signals are processed using MATLAB to extract target movement and rate.

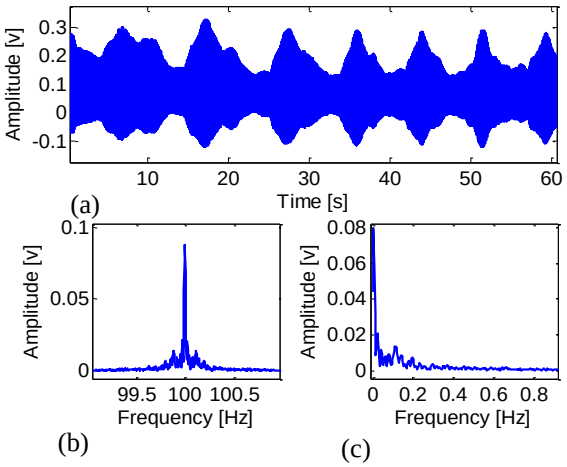

Fig. 5.4 (a) Received baseband signal. Amplitude modulation by the respiration signal is clearly visible; (b) Pulse repetition frequency with respiration information content around the PRF; (c) Filtered signal multiplied by $e^{-j\omega t}$

Since the PRF was 100 Hz in Fig. 5.4 and high enough compared to Doppler frequency, the pass-band filter corner frequencies are tuned for 50 Hz to 150 Hz to isolate the first harmonic of the signal and preserve the frequency content, as shown in Fig. 5.4(b). A 100 Hz PRF shifts the signal content from DC where flicker noise is at its maximum and thus helps to increase signal-to-noise ratio. Fig. 5.4(c) depicts the filtered signal multiplied by $e^{-j\omega t}$ and the respiration spectrum information.

Different movements are investigated to evaluate the setup. Fig. 5.5(a) illustrates complex motion representing heart and respiration signals. A low-IF signal is depicted versus a reference signal and the envelope of the pulses. The mechanical target with

trapezoidal motion was also tested to demonstrate the full spectrum preservation of a low-IF system as seen in Fig. 5.5(b). It is interesting to note that AC coupling does not distort the signal in low-IF architecture. However, the coupling effect is clearly visible for the envelope of the signals due to amplitude modulation. Fig. 5.5(c) shows the low-IF human respiration signal versus the envelope detector output and reference piezoelectric chest belt.

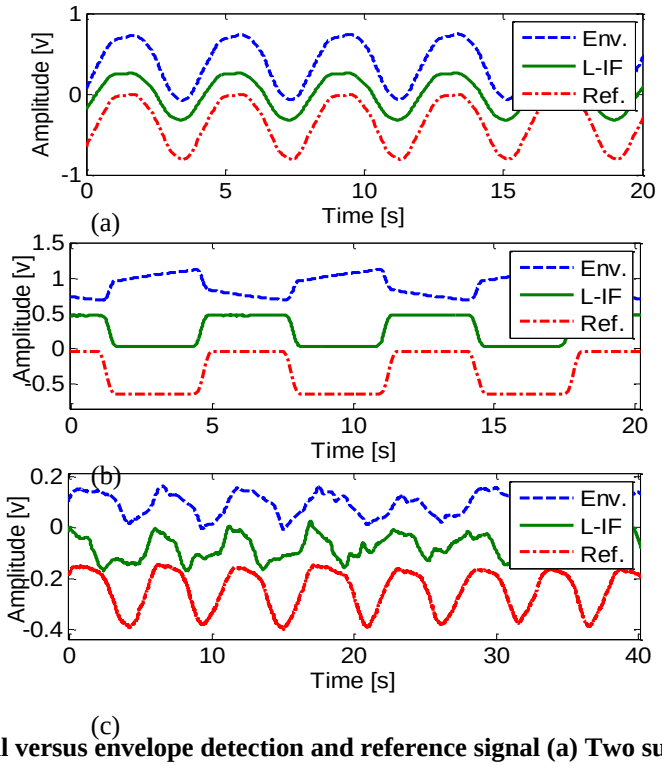

Fig. 5.5 Low-IF signal versus envelope detection and reference signal (a) Two superimposed complex motions; (b) Trapezoidal motion; (c) Respiration signal.

To further investigate the position sensitivity of the receiver to absolute distance or initial position between the target and antenna, a quadrature receiver is employed with a continuous-wave local oscillator. Fig. 5.6(a) shows the in-phase channel of the quadrature receiver that is clearly in the null point. Therefore, the envelope of the signal has a double frequency content problem associated with single-channel receivers. However, the low-IF

signal does not suffer from this issue. Fig. 5.6(b) shows the quadrature output of the receiver which is in the optimum point and is in agreement with the reference and low-IF signals.

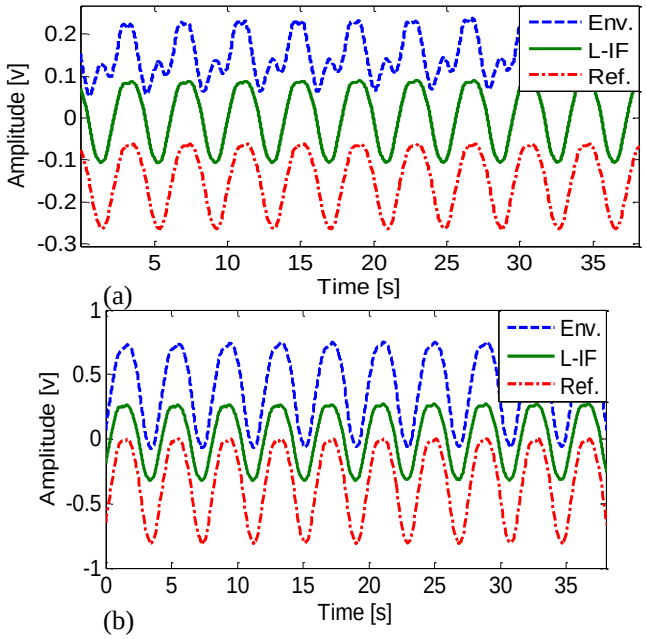

Fig. 5.6 Low-IF signal versus envelope detection and reference signal (a) Null point; the envelope detection method suffers from position sensitivity (b) Optimum point;

Effects of different PRFs are also investigated. Fig. 5.7 shows various PRFs from 10 Hz to 100 Hz for both complex and trapezoidal signals. Because the bandwidth of these signals are limited, and PRFs are high enough, changing pulse repetition frequency has negligible effects. The advantage of using lower PRFs is to alleviate the hardware requirements for higher sampling rates.

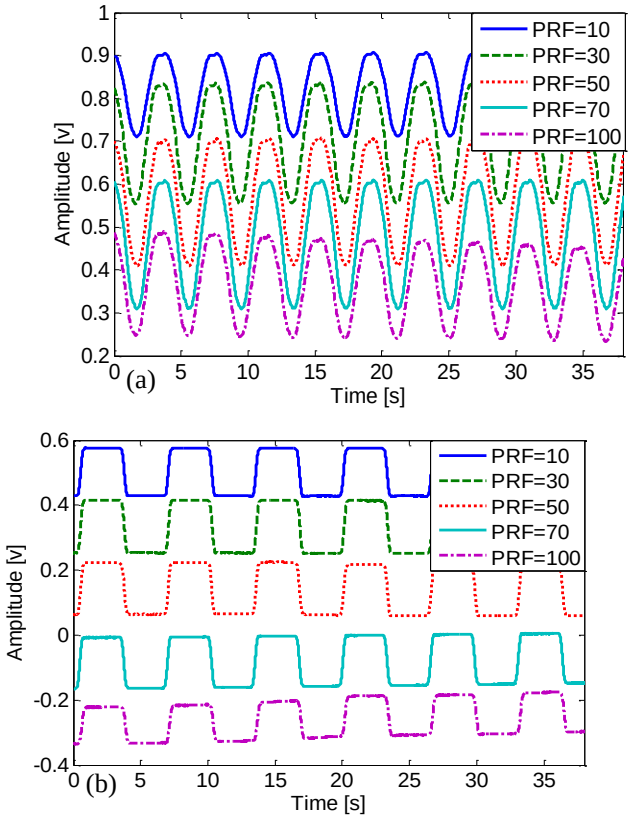

Fig. 5.7 Changing pulse repetition frequency from 10 Hz to 100 Hz, (a) Low-IF signals for complex motion; (b) Trapezoidal motion.

Fig. 5.8(a) shows the received signal spectrum in baseband after amplification and filtering for trapezoidal movement with PRF = 10 Hz. As expected, the Doppler frequency should be repeated around the PRF. The first five harmonics are isolated by different band-pass filters and demodulated accordingly. Fig. 5.8(b) shows the demodulated signals for the aforementioned harmonics. Higher harmonics have lower amplitudes, due to less energy that they carry, but the full spectrum is recoverable even at higher harmonics.

Finally, a different architecture is also employed with a pulsed local oscillator. In previous experiments, only the transmitted signal has been modulated by pulse trains. However, in the new architecture, the receiver local oscillator is also modulated. Fig. 5.9

shows the modified architecture. After processing the received baseband signals for both architectures with exact same conditions, the outputs are shown in Fig. 5.10. The pulsed LO receiver clearly has a weaker signal as opposed to continuous-wave LO.

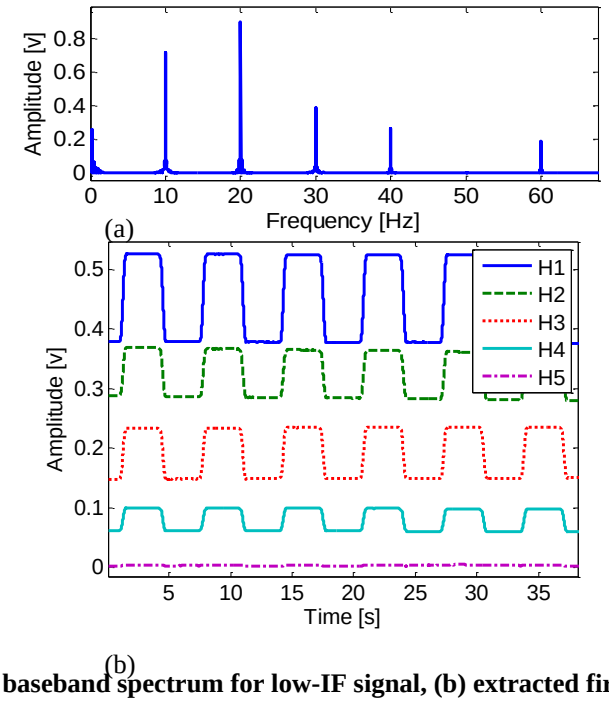

Fig. 5.8 (a) Received baseband spectrum for low-IF signal, (b) extracted first five harmonics of the signal

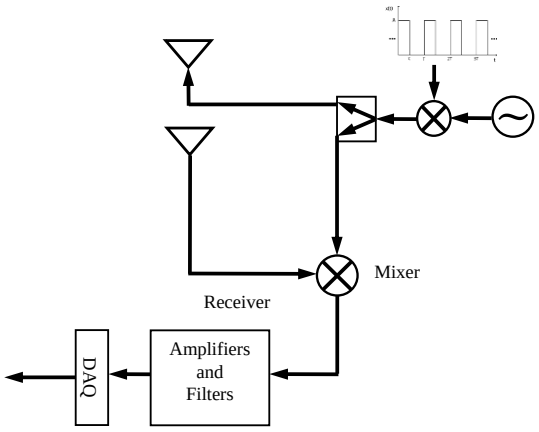

Fig. 5.9 Block diagram of a single-channel Doppler radar system with pulsed LO. Same modulated signal is fed to the receiver.

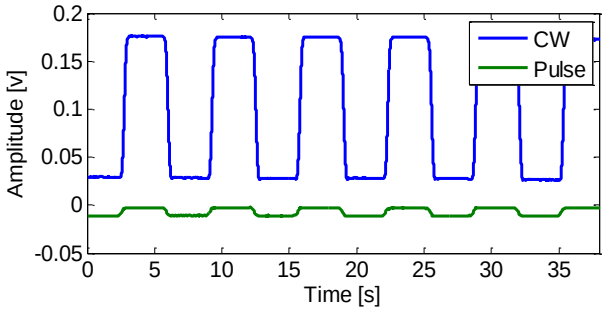

Fig. 5.10 Continuous-wave and pulsed local oscillator signals

5.4 Discussion

Benefits of a single-channel low-IF demodulated pulse Doppler radar are discussed in this chapter. It was demonstrated that pulse radar for physiological signal monitoring can take advantage of a heterodyne architecture and keep the simple design of a homodyne receiver. Various pulse repetition frequencies, harmonics, signal shapes, and system architectures are employed. Since the spectrum of the received signal is examined as opposed to amplitude modulation in time domain, benefits of a quadrature receiver can be achieved with a simple single-channel system.

6. SIGNAL ESTIMATION FOR SUBJECT DETECTION

True presence detection through passive infrared and ultrasonic sensors has been proven to be inefficient [103], and there is a need to integrate another sensing mode for the purpose of occupancy detection. Different methods of occupancy detection have been investigated in the literature. [104] reported video-based human occupancy sensing, using web cameras and image processing algorithms to detect occupants, but it raises serious privacy issues. In [105], a particulate matter sensor is used to infer the local movement of occupants in a corridor by sensing the resuspension of coarse particles. It can only detect local movement and needs calibration. [ ] presents an occupancy detector that exploits a fluorescent lamp's own stray electric fields as an excitation source for a capacitive sensing occupancy detector. However, the range is limited.

Radar has been used for perimeter intrusion detection systems [106], see through the wall [107], gait characterization [108], and indoor positioning [109]. Detection of human subjects using Doppler radar based on heart signals was proposed in [92]. In this chapter the feasibility of a Doppler radar occupancy sensor will be explored by detecting respiratory and heart signals. A significant challenge for wide adoption of this sensor is to demonstrate reliable system performance at low power and low cost. The performance of

a Doppler radar occupancy monitoring system is compared with conventional occupancy sensors, and it is demonstrated that Doppler has superior performance over traditional sensors.

Doppler radar occupancy sensor not only can detect subjects, but also can estimate the direction of arrival and can isolate subjects spatially. Various considerations in the design and use of efficient occupancy sensors will be described, along with the benefits that can be obtained through intelligent systems.

6.1 Occupancy Sensing

Occupancy sensors have been used for a variety of applications over the last three decades. While initially developed to control lighting in commercial buildings, primarily for security, the use of occupancy sensors steadily extended to the control of heating, ventilation, air conditioning (HVAC), and other presence-related loads and demands in commercial and residential spaces [110, 111].

The main advantage of using occupancy sensors is conservation of energy through the automated shutdown of loads no longer needed when a space is unoccupied. With a nearly 50% projected increase in global energy use by 2035, most of it from fossil fuels, energy efficiency and energy conservation are becoming increasingly important. In the US, residential and commercial users account for 42% of total energy consumption [112]. In residential areas, about 30% of electricity is used for lighting and HVAC systems. In commercial buildings, they account for over 50% of electricity consumption, and in hotels they can represent up to 80% of the utility bill [113]. [ ]**Error! Reference source not found.** shows a breakdown of electrical energy usage in commercial office buildings [114].

Research has shown that occupancy detectors can save up to 80% of energy used for lighting and HVAC systems, also resulting in significant financial savings [115]. This is particularly relevant to tourism, as energy consumption in hotels is significantly higher than in residential and even commercial buildings.

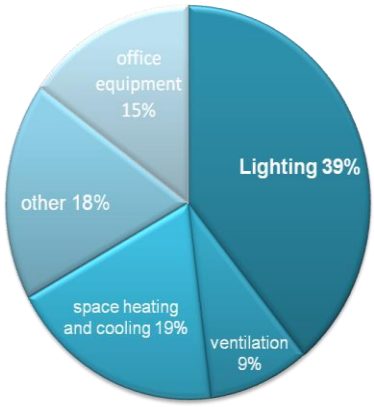

Fig. 6.1 Electrical energy usage in commercial office buildings

Occupancy detection can be divided into two categories: occupancy sensors and vacancy sensors. Occupancy sensors trigger lighting or other loads automatically based on human presence. In the case of vacancy sensors, a user manually turns lights on, and the vacancy sensor turns them off when the sensors can no longer detect activity within a specified area. These sensors are suitable for areas such as restrooms and stairwells. Sensors usually allow the customer to set time delays (usually 10 to 15 minutes) between the lack of activity and turning off the lights. Short time delays can result in higher energy saving, but may result in unwanted switching (false alarm) or may lower the life-span of a load due to frequent on-off switching. Longer time delays avoid numerous on-off cycles, especially in areas where occupants come and go more frequently. It can also allow for short periods where occupant movements are very small, such as typing on a keyboard. Research has shown that the time delay of the sensor should vary according to

the activity level of the occupant [110]. More energy savings is possible if the sensor can adjust the time delay based on occupant's behavior.

Occupancy sensors are usually mounted on ceilings or walls. Depending on the space, single or multiple sensors may be needed to cover all areas. For instance, in a small office, one sensor may provide sufficient coverage, while in a large warehouse, numerous sensors may be needed to detect movement with required accuracy. Range and coverage can also differ from one manufacturer to another.

False-positive events occur when a sensor detects motion while there are no occupants in the monitored area, resulting in a waste of energy. On the other hand, false-negative events occur when people occupy a space, but the sensor does not detect their presence and eventually leaves the occupants in the dark. This results in an unpleasant experience for users, and negatively influences user compliance. It is equally important that the sensor prevents false negative and positive events.

6.1.1 Common Occupancy Sensors

There are two common types of occupancy sensors used for building automation systems: Passive Infrared (PIR) and Ultrasonic sensors.

6.1.1.1 Infrared Sensor

Passive infrared (PIR) sensing is the most commonly used technology in this field. PIR sensors can detect the heat pattern change from people occupying a space. A pyroelectric detector located behind a lens detects heat sources and generates a temporary voltage. The detector responds to optical energy in the infrared region. It can sense the infrared

energy change emitted from different sources such as people and walls. When a person passes through the detection zone of the sensor, it modulates the infrared energy across the detector resulting in a small electrical signal. The signal is then amplified and compared with a set threshold. If it exceeds the threshold, occupancy is detected and the lights would be turned on. A sample output signal of a PIR sensor is illustrated in Fig. 6.2.

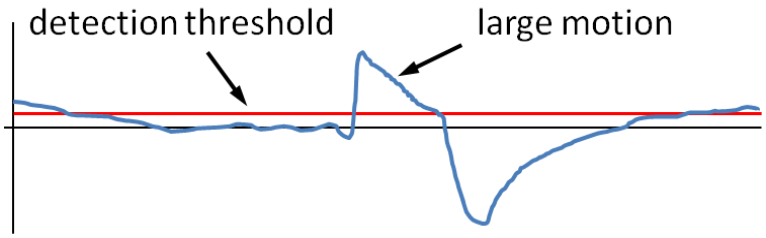

Fig. 6.2 Output of a PIR detector when large motion is sensed. Occupancy is detected when the signal surpass the threshold.

While large motion or locomotion, such as walking, can far exceed the threshold, fine motion like writing, typing, and turning the page of a book may not surpass the threshold. The received signal is not only affected by the motion signature, but also by the noise and interference present. The total noise is a combination of interference sources in a space and the thermal noise of the circuit itself. Fig. 6.3 illustrates noise and interference affecting the sensor performance.

One major shortcoming for conventional PIR detectors is a high rate of false negatives. They work well in detecting large body motion like walking and running; however, these sensors have problems detecting smaller motion such as occupants working at a desk or watching TV.

The sensitivity setting of these devices is critical for their performance. If the sensitivity is set too high, noise and interference can trigger the sensor, and generate a false positive, which means it turns lights on when a space is still unoccupied.

Unnecessary lighting wastes energy. If the sensitivity is set too low, the sensor is not capable of detecting smaller motion, and it may turn off the lights while occupants are still in the monitored space. The challenge here is distinguishing the difference between background noise and actual motion.

PIR sensors require line-of-sight; therefore, they cannot see around objects. These sensors are best suited for areas with little or no obstruction, such as meeting rooms and private offices.

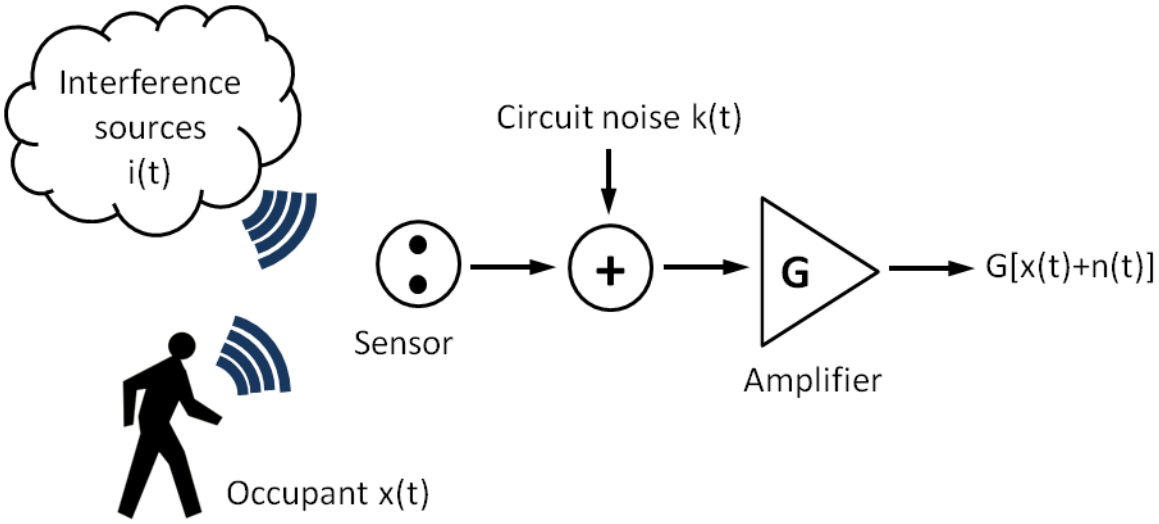

Fig. 6.3 Detector performance is affected by interference from the space, i(t), and circuit noise, k(t). The n(t) term is a combination of thermal noise in the circuit and interferences from other sources in the space.

6.1.1.2 Ultrasonic Sensor

Ultrasonic sensors emit an inaudible high-frequency sound wave in the range of 25-40 kHz. Motion within the area changes the reflected ultrasound wave's frequency. The frequency of the backscattered signal from the objects and people is measured in the sensor in order to detect motion. In contrast to PIR sensors, these sensors are not limited to line-of-sight, and can see around objects as long as the surfaces are hard enough to reflect sound waves with enough energy to be detected by the sensor.

Since these sensors are not line-of-sight limited, they are capable of detecting all types of motion even when movement is behind an obstacle. These sensors work best in indoor spaces, in large areas containing obstacles, or unusually shaped areas such as large conference rooms, offices, and bathrooms.

Ultrasonic sensors are more expensive than PIR sensors. In addition, the false alarm rate is higher in this type of sensor, and because they generate sound waves they can interfere with hearing aids, other sensors, and certain animals with ultrasonic hearing ability.

6.1.1.3 Dual Technology/Hybrid

Hybrid sensors use both PIR and ultrasonic sensors in their design. The ultrasonic sensors are sensitive to small movement, while the PIR sensors are better suited for large body motion. Hybrid sensors have the advantages of both sensors, and provide maximum reliability and coverage while minimizes false alarms. Due to its design these sensors are suitable for a wide range of applications. However, the cost of a typical hybrid sensor is $100 or more, which is higher than PIR and ultrasonic sensors individually, and these sensors require more adjustments. Hybrid sensors are best suited for large open spaces, and for areas with unusual occupancy patterns [114].

6.2 Doppler Radar Occupancy Sensors

The advent of integrated low-power microprocessor/RF-transceivers provides a new platform for combination of sensing, processing and communications [34] which make Doppler radar technology feasible for occupancy monitoring applications and can form

the core of a wireless smart sensor network for applications such as “smart building” systems.

A significant drawback of currently available occupancy sensors is the high rate of false alarms and failure to detect stationary subjects [115]; thus the sensor effectively becomes a motion sensor, not a presence sensor [116]. The detection of human cardiopulmonary motion with Doppler radar could provide a promising approach to overcome the problems of false trigger and “dead spots” in conventional sensors. Radar sensors measure uniquely modulated backscattered electromagnetic signals rather than IR or ultrasonic signals, and can overcome the usual limitations associated with occupancy sensors to make true presence detection feasible.

To improve radar receiver performance and overcome limitations in single-channel receivers, a quadrature receiver architecture is widely used. If a quadrature receiver is used, the I and Q channels in the baseband need to be combined for optimal phase detection. There are linear and nonlinear methods to combine baseband channels, which are referred to as demodulation methods [15, 31].

Nonlinear demodulation is based on the fact that the I and Q channels form a circular arc in the complex plane. If the radius of this circular arc can be estimated, the phase can be extracted from the arc information. Since this method uses a nonlinear arctangent function on baseband signals for deriving phase it is also called arctangent demodulation. The major advantage of this method is the ability to estimate actual displacement in addition to motion repetition rate.

6.2.1 System architecture

The block diagram of a quadrature Doppler radar is shown in Fig. 6.4. A splitter is

used to split the signal source into the transmitter antenna and local oscillator. The local oscillator signal is then split again into two paths with a 90° phase difference. The transmitting antenna sends a 2.4 GHz signal into the space and the receiving antenna listens for the backscattered signals from the objects in the space. Transmitted power is 7 dBm at the antenna port.

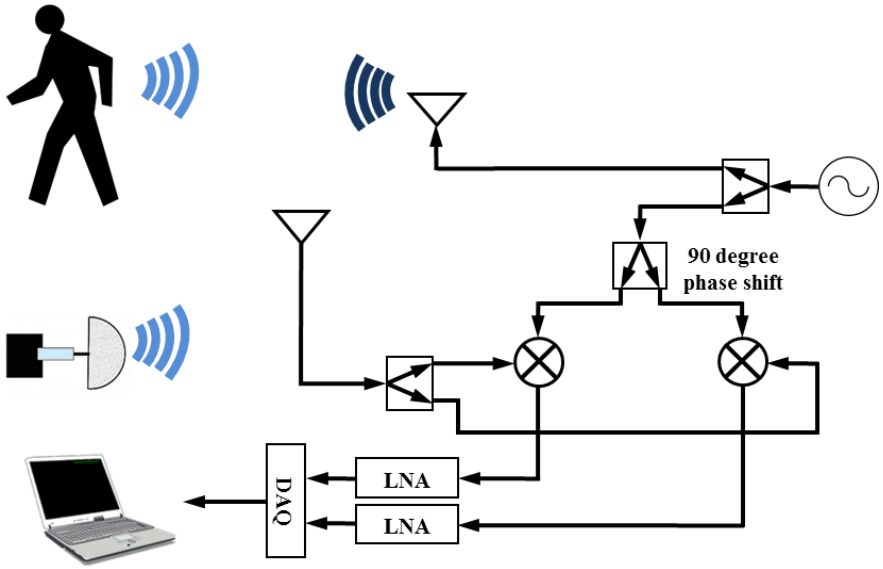

Fig. 6.4 Block diagram of a quadrature Doppler radar system. The LO signal is divided by a two-way, 90° power splitter to get two orthonormal baseband signals (I and Q).

The received signal is down-converted with a mixer. After down-conversion, the baseband signals are filtered and amplified with a low noise amplifier. The data is then recorded by a data acquisition device. Several parameters, such as transmitting power, antenna characteristics, and oscillator phase noise determine the radar operating range.

Transmitted power	7 dBm
Power Dissipation	115 mW
Antenna Characteristics	60° E-plane beamwidth, 8 dBi gain
Operating frequency	2.4 GHz
Receiver type	Homodyne Qudrature receiver

Table 3.1 Transceiver characteristics.

6.2.2 Experimental Results

A 2.4 GHz homodyne Doppler quadrature receiver with off-the-shelf coaxial

components has been employed for detecting presence. Table 3.1 summarizes the radar specifications. For discriminating presence over an empty room, a short time window is used to slide through the time-domain data. The window length N is determined experimentally based on the responsiveness of the occupancy detector. For a windowed signal with the length N, the average of the squared signal is calculated [11]:

$$Ave(t) = \frac{[B_{c1}(t)^2 + B_{c2}(t)^2 + ... + B_{cN}(t)^2]}{N} \tag{6.11}$$

where $Ave(t)$ is the moving average output, and $B_c(t)$ is the combined output of I and Q. The window length in this experiment is 5s with 0.5s steps. The sliding window and average calculations are repeated over the entire data set. The experiment was conducted by recording data for 12 minutes. The following is the order of the different levels of activity that was measured: periodic movement of a mechanical object, empty room, human subject in stationary position (respiration and heart only), walking in different directions, and high intensity activity like running. Fig. 6.5(a) shows the results of the experiment. A mechanical target was used in this test to represent periodic motion in a space such as fans that can interfere with sensors and cause false alarms.

At the beginning of the test the only movement was the periodic motion of the mechanical target. The target frequency was 1 Hz with 1 mm amplitude. The amplitude of the periodic motion was selected this small to be closer to heart and respiration range, thus making it harder to discriminate.

The mechanical target and human subject for the stationary position were both one meter away from the antennas. During walking and high intensity activities, the antenna was 1.5 meters from the subject. The mechanical target's motion was sinusoidal, with a frequency of 1 Hz and amplitude of approximately 1 mm.

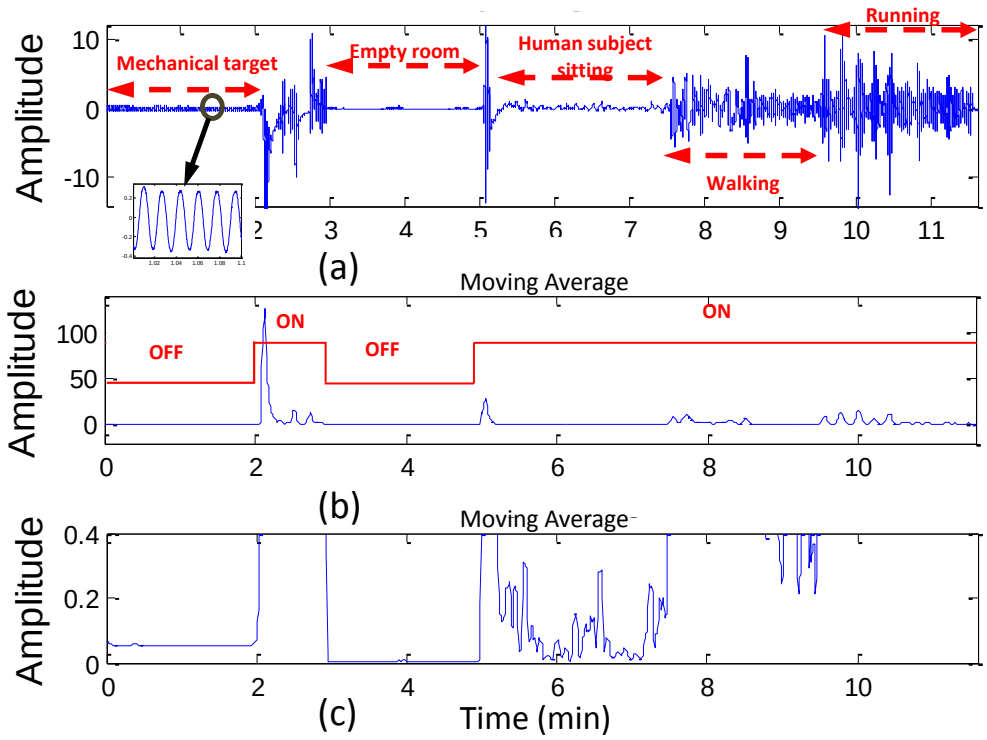

Fig. 6.5 (a) Twelve minute activity measurement: mechanical object periodic movement, empty room, human subject in stationary position (respiration and heart only), walking in different directions, and high intensity activity. (b) Moving average output, the rectangular line shows detected activity over no motion. (c) A zoom in of the y axis is also shown.

The Fig. 6.5(a) subset illustrates a zoom-in of periodic motion. The spikes between 2 to 3 minute range took place due to changing the setup and removing the target. Between 3 to 5 minutes, the empty room with no motion is recorded. By the end of the fifth minute, the human subject entered the room and sat on a chair one meter away from the antenna with no motion for about two minutes. Finger pulse and piezoelectric sensors are attached to the subject as a reference for the Doppler sensor. Then, after removing the sensors, the subject began walking in different directions and doing high intensity activities until the end of the experiment. The outputs of the moving average and activity detection are depicted in Fig. 6.5(b). If an activity is detected in the environment, then the sensor's output would become one, which is illustrated by "ON". Otherwise, there is no motion and the lights and other occupant-related loads would be turned off. The spikes due to

changing the setup and walking are easily recognizable in the moving average output. However, by zooming into the y axis (Fig. 6.5(c)), different occupancy levels are more pronounced. Periodic motion has a constant level at about 0.05; an empty room is very close to zero. The human subject at a stationary position has a changing pattern due to respiration, which is manually discriminated over no motion and periodic motion by different thresholds for the output level and width of the spikes. If the moving average output is larger than the empty room's level, smaller than locomotion threshold, and does not have a constant level like periodic motion, then true human presence can be detected by identifying presence of respiratory and heart signals.

The input signal is filtered by means of analog filters between 0.03 Hz - 30 Hz with a 6 dB/oct rolloff. This simplifies the digital preprocessing for respiration and heart signal detection. A portion of the input signal (Fig. 6.5(a)) between the 6th and 7th minute, when subject is at rest, is illustrated in more detail in Fig. 6.6. Fig. 6.6(a) illustrates the Doppler radar respiration signal and reference chest belt. To detect the heart signal, it is isolated from the combined heart and respiration signals with a sharp band pass filter with 0.6 to 3 Hz cutoff frequencies to attenuate respiration signal and remove out-of-band noise.

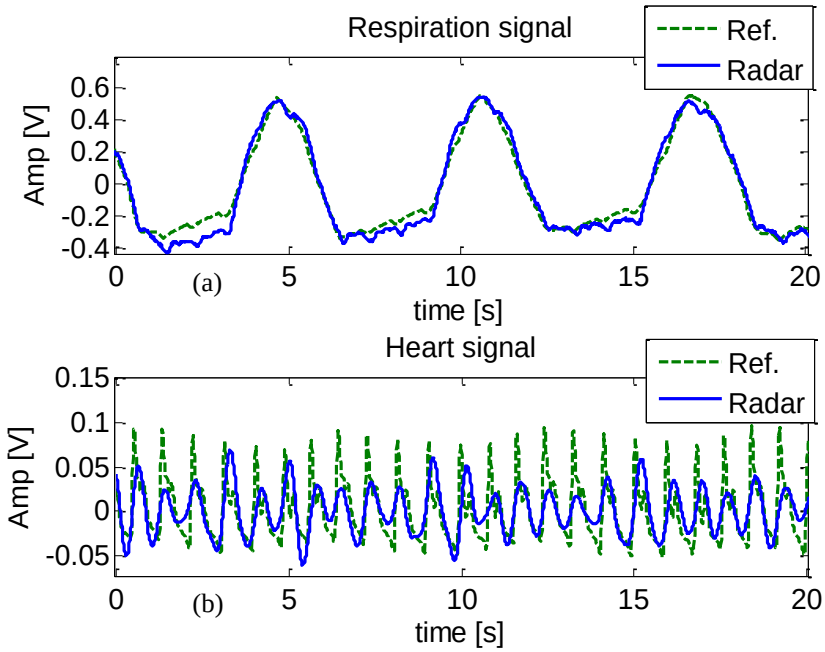

Fig. 6.6 (a) A portion of the signal containing piezo-electric chest belt which was used as a reference and radar signal are shown; (b) the extracted heart signal compared to a finger pulse reference.

Fig. 6.6(b) shows extracted the heart signal versus the finger pulse reference. The next step would be extracting heart rate and observing heart rate variability.

6.2.3 Rate Calculations for Doppler Radar Occupancy Sensor

A windowed FFT is performed for each of the signals in Fig. 6.6 in order to obtain the rate variation with time. A Kaiser window of 8 seconds is used and moved by 0.5 second steps over data. An exponential filter is employed to smooth the output rate.

Fig. 6.7 shows calculated heart rate from the occupancy sensor when the subject is at rest. The average heart rate for the period of two minutes was 70.4 beats per minute. The mean difference between the reference heart rate and the Doppler heart rate was 0.03 bpm, the standard deviation of the difference was 0.6 bpm, and the root mean square error of the difference was 0.6 bpm.

Once a respiration-like pattern is sensed by looking at respiratory rate, the subject

presence can be identified over other periodic motions. Even if the subject has a very constant periodic respiration, true human presence can be detected due to heart rate variability by investigating the heart signal.

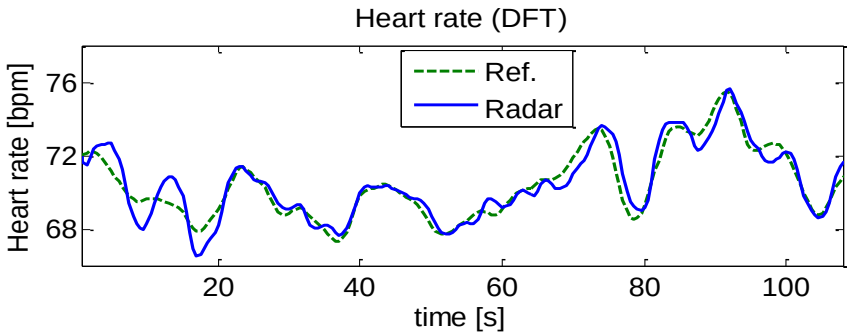

Fig. 6.7 Heart rate from radar and finger pulse reference.

6.3 Performance Comparison between Doppler Radar and Conventional Occupancy Sensors

As previously shown, Doppler radar seems to be reliable for detecting stationary presence. The most widely used occupancy sensors are PIR and ultrasonic sensors. In this section, motion detection limits of a hybrid infrared and ultrasonic sensor are investigated and compared to continuous-wave Doppler radar sensor. The sensors were tested with a human subject and mechanical targets. Testing included major and minor human motion such as hand waving at a distance of two meters from the sensor, and also sitting in a chair while writing. To further explore the sensing capabilities of the hybrid sensor, human subjects wore multiple layers of clothing and the same tests were repeated.

6.3.1 System Setup

The block diagram of the system used for the measurements is shown in Fig. 6.8. The HP E4433B signal generator is used as the signal source for the continuous-wave radar.

The transmit power is 7dBm at 2.4 GHz frequency. A Minicircuits ZFSC-2-2500 splitter is used to split the signal between transmitter and receiver. The Antenna Specialist (ASPPT2988) with 8 dBi gain and 60° E-plane beamwidth is used in both transmitter and receiver sides. The received signal is down-converted with Minicircuits ZFM4212 mixers. Baseband signals are amplified and filtered with Stanford research low-noise amplifiers Model SR-560.

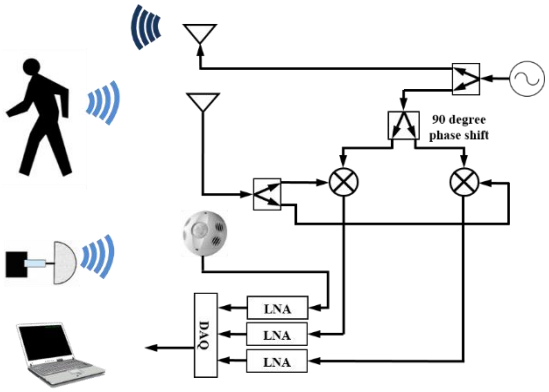

Fig. 6.8 Block diagram of the system; Doppler radar in conjunction with hybrid occupancy sensor.

The Leviton OSC10-M0W multi-technology hybrid occupancy sensor is used as a common occupancy sensor, which is equipped with both infrared and ultrasonic sensors. Fig. 6.9 illustrates the sensor without the cover. The signal processing algorithm of the commercial hybrid sensor was bypassed, and other outputs from the infrared and ultrasonic sensor were used to collect measurements. An output, which produces a short narrow pulse, correlated to the sensor detecting a movement by the test subject. Sensitivity controls for the ultrasonic and infrared sensors were also available at a range from 0-100%. After low-pass filtering with a cutoff frequency of 100 Hz to avoid aliasing, the pulses were recorded via an A/D converter with a 500 Hz sampling rate.

Fig. 6.9 Leviton OSC10-M0W multi-technology hybrid occupancy sensor

6.3.2 Experimental Results

Mechanical motion was tested using a mechanical target at a distance of 1 meter, an oscillation frequency of 0.3 Hz and a 2 cm range of motion. As seen in Fig. 6.10, only radar was able to detect the motion. The ultrasonic and infrared sensors were unable to detect any motions.

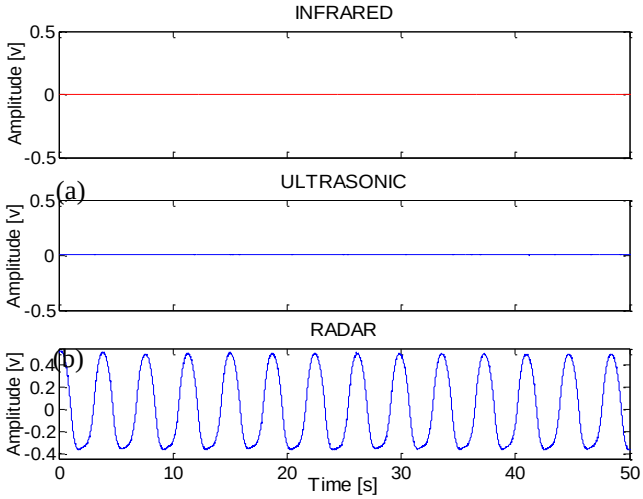

Fig. 6.10 Mechanical target oscillating in a perpendicular direction relative to the sensor.

At a distance of 2 meters from the sensing apparatus, major and fine motion tests were completed using human subjects. The major motion test consisted of waving arms

laterally for 20 seconds, remaining still for 10 seconds and then pushing arms toward the sensor for 20 seconds. This motion test was carried out for all sensitivity combinations of ultrasound and infrared. The test subject wore multiple layers of clothing to test another variable at all sensitivities. A comparison between high-sensitivity tests with and without multiple layers of clothing is illustrated in Fig. 6.11.

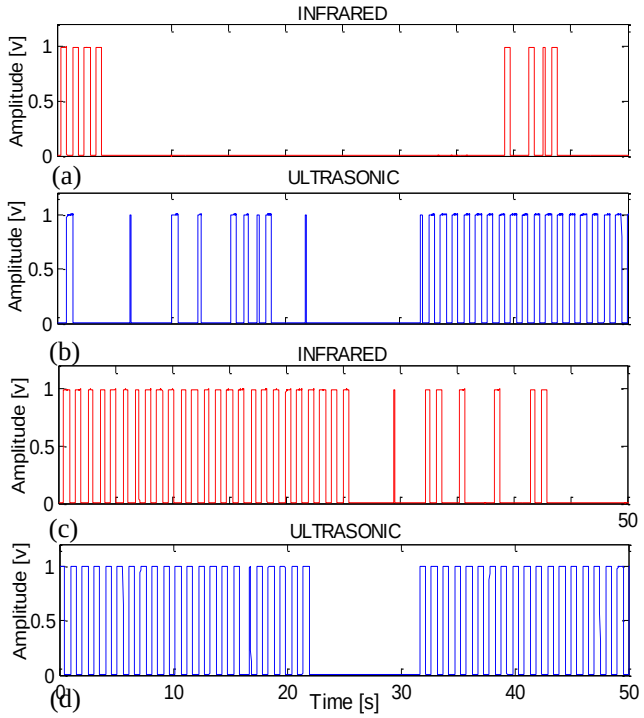

Fig. 6.11 (a) , (b) Human subject major motion wearing three layers of clothing. Sensitivity of Infrared and ultrasonic set to 100%; (c), (d) Human subject major motion wearing one layer of clothing. Sensitivity of Infrared and ultrasonic set to 100%.

There is decreased sensitivity to movement when a subject is wearing multiple layers of clothing and differences are more prominent with lateral movement. The addition of multiple layers of clothing has a non-trivial effect on the sensing capabilities of the hybrid sensor even at high sensitivity settings. They also show that the infrared sensor is more sensitive to lateral motion than pushing movement.

Fine motion tests included writing while sitting in a chair at a distance of 2 meters for

50 seconds. Fig. 6.12 compares the sensor outputs of the Doppler radar and hybrid sensor. Doppler radar was able to detect minor movement throughout the test while infrared detected movement when the subject increased range of motion. The ultrasonic sensor was not able to detect any minor motion from writing. Doppler radar outperforms the hybrid sensor in all tests and could be used to differentiate between mechanical and human targets.

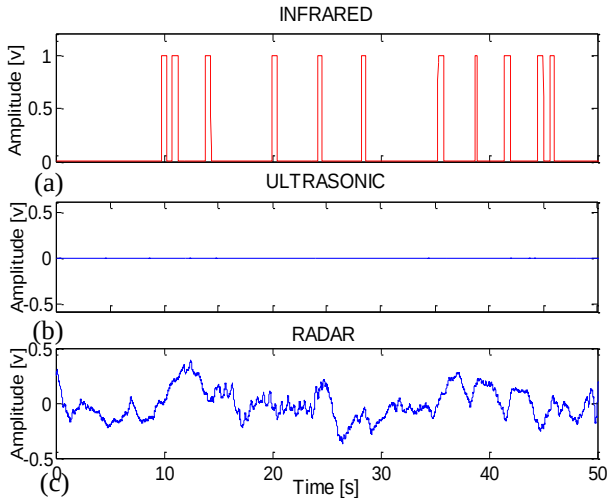

Fig. 6.12 Human subject fine motion, sitting in a chair writing while wearing one layer of clothing. Sensitivity of infrared and ultrasonic set to 100%.

6.4 Multiple subject detection

True presence detection based on vital signs is feasible using radar technology as discussed in this chapter [12]. When there is more than one person in a space, it is difficult to distinguish individual subjects. However, it has been demonstrated that Doppler radar has the ability to isolate subjects in single or multiple antenna systems [92]. In other words, the sensor is not only capable of detecting people, but can also count individuals and isolate them based on different cardiovascular signatures.

In a single-antenna system, based on expected different spectral signatures of individual cardiovascular related motion, it is possible to separate individual signals in

the frequency domain [92]. In a multiple antenna system (SIMO or MIMO), even if individual cardiovascular signatures are very similar, it is possible to distinguish different subjects based on angle of arrival and cancelling motion artifacts [54]. Signal processing techniques such as Blind Source Separation (BSS) has been employed in single and multiple antenna systems to discriminate subjects and clutter [117]. Estimating the direction of arrival (DOA) can help separate subjects spatially in a multi-antenna environment. Common algorithms for finding DOA are multiple signal classification (MUSIC) and estimation of signal parameters using rotational invariance techniques (ESPIRIT) [118]. DOA can be estimated from the phase difference of backscattered signals at the receiving antennas [119].

An experimental quadrature Doppler radar is designed for detecting DOA information of a moving target. Custom designed patch antennas, and off-the-shelf elements are used to make a low-cost system achievable. In this design one transmitting antenna and four receiving antennas are employed for extracting direction information. An RF switch is used to effectively multiplex eight different quadrature channels into two channels in order to reduce hardware complexities. This approach is feasible due to the slow changing nature of physiological signals. The de-multiplexing can be done online in software after digitizing the signals. The MUSIC algorithm is then applied to the baseband signals and the direction of arrival is calculated. Feasibility is demonstrated for a single mechanical target, two mechanical targets and a human subject breathing in front of the radar in separate experiments. Due to the more compact, low cost and simple nature of the design, the path is paved for applications in multiple human subjects monitoring, monitoring of multiple body parts of the same human subject, and reduction

of unwanted background moving clutter. This is the first application of DOA estimation in vital signs monitoring that is based on a simple low-cost RF time-multiplex system.

6.4.1 Time-domain Multiplexing of RF Signals

Fig. 6.13 shows the concept of multiplexing several antennas' RF output into one RF received signal ready for demodulation using the IQ demodulator. By using an RF switch and sharing the received RF path, only one IQ demodulator and a subsequent set of baseband amplifiers are needed to down-convert the multiplexed RF signal into baseband. This will simplify the RF path and reduce the number of components needed. The number of baseband channels to be acquired is now only two (I and Q) instead of eight.

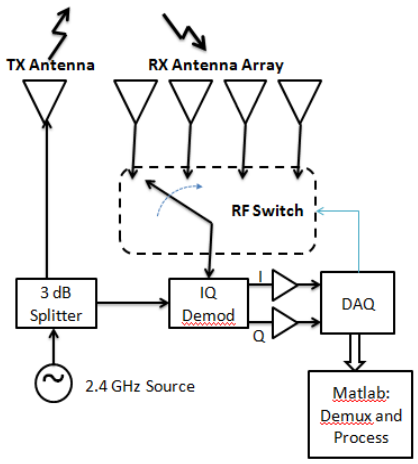

Fig. 6.13 The functional block diagram of the proposed multi antenna system showing transmit and receive antennas, RF switch, demodulator, baseband amplifiers and DAQ.

The RF multiplexing is possible due to the limited bandwidth of the physiological signals (typically within DC - 2 Hz). Since each of the RF channels has various received carrier levels, they will cause their own DC offsets in the baseband. The outputs of the IQ demodulator will have a DC offset that is dependent on the channel that is selected by the

RF switch, hence baseband signal must be DC coupled. In the meantime, there will be switch transients involved that can be eliminated by carefully selecting the sampling rate, switch rate and the de-multiplexing method. The bandwidth of the baseband amplifiers must be large enough to allow passing of all switch transients so that de-multiplexing can be done seamlessly.

6.4.2 Experimental Setup

The RF front end was designed and fabricated on a FR4 board with a thickness of 60 mm. Fig. 6.14 depicts the board with the components assembled on it. A Hittite HMC241LP3 RF switch was used for multiplexing the RF signals. A Skyworks SKY37009 RF demodulator was used. A 2x2 microstrip patch array was implemented for receiving, and a single patch was used for transmitting the RF signal. The receiver antenna elements were separated by 6.125 cm, which is half of the free space wavelength at the frequency of operation. A Murata LDB21 balun and a Minicircuits RPS-2-30 power splitter were used. An HP E4433B signal generator was employed as an RF source, operating at 2.4 GHz and an output power of 6 dBm. Two SRS560 low-noise amplifiers were used to amplify the baseband I and Q signals. The demodulator generates differential IF outputs. IP and IN outputs are respectively connected to the A and B inputs of the SRS amplifiers. The amplifier is set to amplify the A-B signal with a voltage gain of 200.

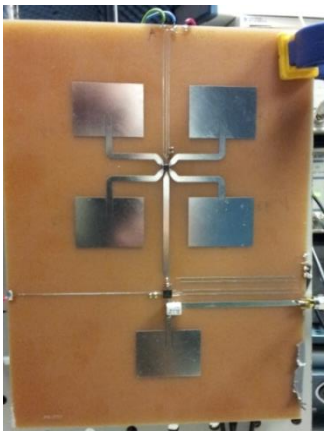

Fig. 6.14 Assembled RF board showing the 2x2 RX antenna array, TX antenna, RF switch, demodulator, balun and power divider.

The signals are DC coupled and low-pass filtered. An 18-bit NI USB-6281 DAQ was used for acquiring the amplified IQ baseband signals and also generating the switch control commands. A mechanical target, consisting of an aluminum wrapped hemisphere with a diameter of 9 cm, and moving with a frequency of 0.3 Hz and a displacement of 1 cm is used as a target in the first experiment. In the second experiment, two mechanical targets are located at different angles from the antenna board. In the third experiment, a human subject is seated in front of the radar. The geometry and position of the target(s) relative to the antenna array is depicted in Fig. 6.15. The DAQ sample rate is 10 kSPS and the switching frequency is 400 Hz. Effectively, 25 samples are generated for each I and Q channel during each switch state.

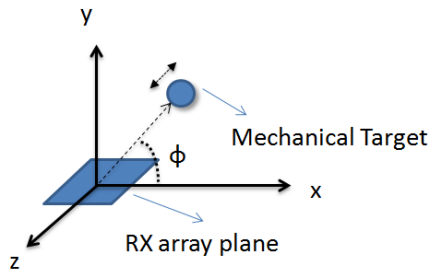

Fig. 6.15 The geometry and relative location of the antenna array from the moving mechanical target. A similar geometry will describe the two targets or a human subject. Φ is the angle of arrival that we are interested in.

6.4.3 Measurement Results

Since the state of the RF switch is known, given that it is controlled by the DAQ device, the IQ channels can be de-multiplexed by calculating the mean value of the 25 samples acquired within each switch state while excluding 3 border samples. This will reduce the effective baseband sample rate to 100 SPS, which is still adequate for these application purposes.

The received data will take the form of:

$$\boldsymbol{x}[k] = [x_1 \ldots . x_N] \tag{6.1}$$

where $x_n = x_{in} + jx_{qn}$ is the complex baseband signal comprised of I and Q channels. N=4 is the number of de-multiplexed IQ channels. k=1…K is the total number of samples acquired. According to the Multiple Signal Classification (MUSIC) algorithm described in [120] pseudo spectrum is calculated. MUSIC, which was originally developed for calculating the frequency spectrum of a signal, estimates the frequency content of a signal using an eigen-space method. With slight modifications, the same concept can be used for processing signals coming from an array. The peaks of the pseudo spectrum are the DOA (or in this case Angle of Arrival - AoA) for the subject(s) in each experiment. Fig. 6.16 shows the amplitude of the pseudo spectrum for experiment 1, where a single mechanical target is oscillating at a 129° azimuth angle from the antenna array. In Fig. 6.17, the time-domain respiration waveform of the human subject obtained from the radar is plotted. The respiration rate is 19 br/min. The human subject is seated at a 121° angle from the radar. A summary of the experiment setups and results is tabulated in Table 3.2.

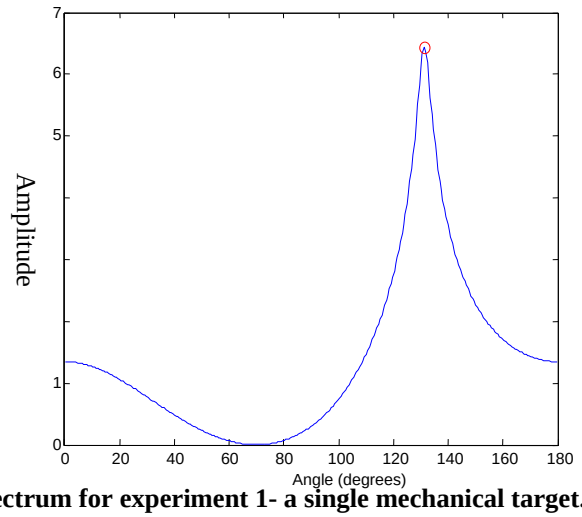

Fig. 6.16 The pseudo spectrum for experiment 1- a single mechanical target. The AOA is the location of the peak of the plot.

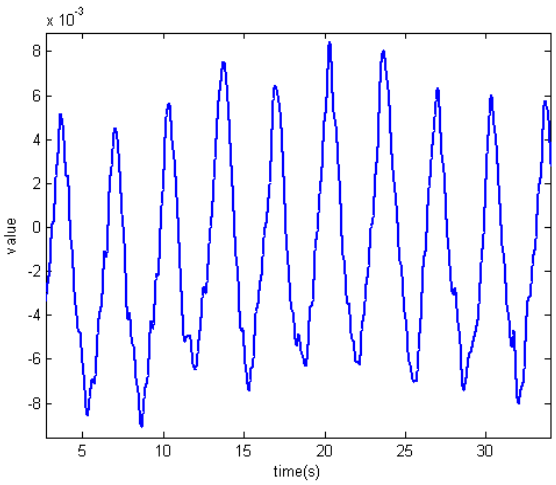

Fig. 6.17 Time-domain respiration waveform obtained from the radar for the human subject breathing at 19 breaths per minute detected at a 121° angle from the antenna.

As tabulated in Table 3.2, the angle of arrival for various setups are calculated and also measured. However, the accuracy of the measurements must be considered. The relative angle of the target from the antenna array was measured using a cotton string and a protractor. This method has its own obvious limitations. On the other hand, the simple MUSIC algorithm used for calculating the angle of arrival assumes no mutual coupling between antenna elements. Also, a simple array factor formulation is assumed, which is

different from the actual pattern of the array.

Experiment	Subject(s)	Range	Measured Angle	Calculated Angle
1	1 Mechanical target	15.5”	129	131.2
2	2 Mechanical targets	31”,37”	54, 131	51.6, 128.9
3	1 Human subject	46”	121	118.0

Table 3.2 Summary of experiments and results

Finally, electrical distance of the targets from the antenna suggests that the targets are not exactly in the far field of the antenna, while most angle of arrival estimation methods assume far field operation within the formulation of the problem. Given the above imperfections of the setup, the proposed setup seems to operate satisfactorily as a proof of concept. Incorporating mutual antenna coupling and using methods for near field angle of arrival estimation will improve accuracy and performance.

6.4.4 Discussion

Occupancy sensors can play a major role in reducing electricity consumption. These sensors can save up to 80% of energy used for lighting and HVAC systems in buildings, which also results in significant financial savings. Major drawbacks of currently available sensors include high rates of false alarms and failure to detect stationary subjects. These sensors are effectively motion sensors, and not true human presence sensors. The detection of human cardiopulmonary motion with Doppler radar could provide a promising approach to overcome the problems of false trigger and “dead spots” in conventional occupancy sensors. True presence can be detected using radar sensors which discern motion associated with respiration and heartbeat from non-human periodic

motion which could otherwise trigger false positives. Such sensors can prevent false negatives by detecting heart and respiration rates and patterns in the case of stationary human subjects. The most significant challenge remaining for wide adoption of radar occupancy sensors will be an effective demonstration of reliable system performance achieved with low-power and low-cost systems.

The mechanism of occupancy sensing through infrared and ultrasonic has inherent weaknesses that are investigated with different tests. Infrared responded well to parallel motion waving and could detect some fine motion greater than a foot in range. Ultrasonic was particularly sensitive to perpendicular motion and lost sensitivity to parallel motion when the subject wore multiple layers of clothing. Infrared's detection of subjects wearing layers of clothing was suboptimal. Doppler radar clearly has superior sensing capabilities, but the power consumption can be an issue for standalone battery-powered sensors. Combining infrared and ultrasonic capabilities together with Doppler radar could be an energy efficient option for occupancy sensing. Doppler radar could be used when infrared or ultrasonic motion sensors do not detect movement. This is especially important when it comes to detecting minor motions or stationary human subjects in a room.

A simple and low cost time-multiplexing DOA Doppler radar system was also demonstrated for physiological monitoring of vital signs. It was shown that the output of such a system has enough accuracy to resolve the angle of arrival (and possibly direction of arrival) of multiple targets or human subjects' vital signs. The accuracy can be increased by using more precise models of the antenna array and the near field effects. Such a compact and low-cost front end can be used for occupancy detection and vital

signs monitoring of multiple subjects and cancellation of unwanted background motion. This technology has the potential to bring occupancy sensors to a whole new level.

7. CONCLUSION AND FUTURE WORK

Doppler radar physiological monitoring provides a promising tool for monitoring heart and respiration signals without contact and through clothing. This technology can have numerous applications, such as sleep monitoring, home healthcare, baby monitoring, burn-injury victims, post-surgery monitoring, tumor tracking, search and rescue applications, see through the wall, gait characterization, indoor positioning, and occupancy detection. Although the technology has been around for a few decades, most of the advancements have been achieved during the past 10 years. The first integrated vital sign monitor was fabricated in 2002, and paved the way for portable vital sign monitors.

Although there was significant progress during the past decade, there are still potential applications that have yet to be tried and challenges needs to be addressed. Some of the challenges are DC offset, coupling issues, position sensitivity, amplitude and phase imbalance, and noise. In this dissertation, aforementioned distortions are explored and novel solutions to address these distortions are introduced and signal estimation methods are proposed to improve sensor's performance.

Channel imbalance is one of the distortion sources in quadrature receivers. To avoid the

position sensitivity issue, quadrature architecture employed. However, one additional path in the receiver architecture typically causes amplitude and phase imbalance between the in-phase and quadrature output of the receiver. A systematic study of Doppler radar channel imbalance effects was presented. Parametric simulations and experiments are performed to investigate the effects of amplitude imbalance, phase imbalance, and initial phase on Doppler radar-obtained pattern, displacement, and rate estimation. Arctangent demodulation with center estimation is used to estimate the displacement. Radius adjustment was also explored to demonstrate how displacement accuracy is affected by radius estimation errors. It is demonstrated that amplitude imbalances of 2 dB or phase imbalances of 32° cause 20 % displacement error, and that displacement error is sensitive to initial phase. Furthermore, it is shown that heart rate errors as high as 25 % can result for amplitude and phase imbalances of 2 dB and 60° respectively. Experimental data obtained using a high precision mechanical target is in close agreement with the simulation results.

A System-on-Chip based Doppler radar monitor was proposed. The radio is developed using an off-the-shelf low-power RF CC2530 SoC chip by Texas Instruments. In order to save power, intermittent transmission at 2.4 GHz is employed rather than continuous-wave transmission. The transmitted data are packets of information instead of a single-tone sinusoidal signal. Although the data content is not extracted, and only the amplitude modulation on data was in our interest, it demonstrated the possibility for using readily available RF sources in the space, such as WiFi, regardless of information content being transmitted. Digital signal processing techniques have been employed to deal with narrow pulses, non-uniform distribution and jitter in pulses. Frequency-domain analysis is also

introduced as an alternative method for signal demodulation and rate extraction.

Although direct conversion transceivers are the first choice for Doppler radar physiological sensing, there are limitations associated with this type of architecture. DC offset is one of major problems that saturate the baseband amplifiers and reduces the dynamic range of the receiver. The common method to avoid the DC offset is AC coupling. While AC coupling removes the DC offset efficiently, it introduces large settling time and signal distortion in baseband. The use of direct conversion-pulsed Doppler radar was explored to overcome this issue. Performance of CW and pulse radar was compared using a mechanical target movement which simulated respiratory motion. The results demonstrate that while AC coupling distorts CW radar output, it has a negligible effect on pulse radar output.

Single-channel receivers are simple but null and optimum position issue is a major problem for this type of receiver. CW Low-IF seems to overcome this issue, but coherent reception is essential for extracting phase information, and this adds to the complexity of the receiver. A pulse low-IF Doppler radar single-channel receiver is investigated for extracting physiological signals. This architecture can take advantage of quadrature receiver benefits without having the complexity and issues of such a receiver. In addition to that, the same LO is used for both the transmitter and receiver, and coherent LO generation is not necessary anymore. This architecture is suitable for detecting low-frequency physiological signals, since it eliminates DC offset and coupling issues, while lowering noise floor. By increasing signal-to-noise ratio, a longer range can be covered with the same transmit power, as well as reduced power consumption. A mechanical target with different motion patterns and a human subject are investigated for proof of

concept and spectrum preservation illustration. Various pulse repetition frequencies and different harmonic extractions are also explored. This is the first reported use of low-IF demodulation for pulse transceiver architecture for Doppler radar physiological sensing.

One of the novel applications of a vital sign monitor explored in this dissertation is occupancy sensing. The feasibility of true human presence detection is explored to overcome the limitations of common occupancy detectors. The current commercially available detectors are more of a motion sensor than a presence detector, and they suffer from high rates of false alarm and failure to detect stationary subjects. An existing cost-effective off-the-shelf System-on-Chip CC2530 RF transceiver is used for developing the radio. Different levels of activity, such as periodic non-human motion, like a fan, a human subject resting, walking, and doing high intensity activity are estimated by processing sensor signals. Heart and respiratory signals are extracted in order to improve stationary subject detection. By investigating the heart rate variability, the ground truth of the human presence is detected.

In addition to single subject detection, multiple subject detection in a single-input multiple-output system with novel receiver architecture that reduces the hardware complexity are also examined. The system is capable of isolating the individuals and counts the number occupants. An experimental quadrature Doppler radar has been designed for detecting the direction of arrival information of a moving target. Custom designed patch antennas, and off-the-shelf elements are used to make a low-cost system achievable. One transmitting antenna and four receiving antennas are employed for extracting direction information. The system is capable of measuring the angle of arrival of two subjects with a 3° error.

7.1 Future Work

In this work, several hardware and software techniques are proposed to pave the way for wide adaption of vital sign monitors and bring it one step closer to its commercial feasibility. However, there is still a lot of room for improvement. Some of the interesting areas that have been identified during this research are:

Different rate estimation methods are employed in this dissertation. Spectral subtraction and low-IF spectrum analysis methods are introduced for extracting the desired information. Time-frequency representations can provide a powerful tool for the analysis of time-series signals. They can give an insight into the complex signals, consisting of several components. Especially in the case of Doppler radar, these analyses could be very beneficial. Many time-frequency (TF) transforms such as: Short Time Fourier Transform (STFT), Wavelet Transform, and Wigner-Ville distribution methods can fail to capture key short-range characteristics of the signals. Synchrosqueezing transform is a consistent and invertible time-frequency analysis tool that can identify and extract oscillating components (of time-varying frequency and amplitude) from non-uniformly sampled and noisy signals. It will be very interesting to apply this method to complex Doppler radar signals. For packet radar and pulse radar, the oscillating frequencies related to Doppler shift may be extracted directly without any further processing. In addition, heart and respiration signals may be identified and extracted with higher resolution and less filtering stages.

Novel application of Doppler radar vital sign monitor as an occupancy sensor is investigated in this dissertation. A System-On-Chip RF transceiver is employed to

develop the radio. However, the processing was done offline using a computer. For a more portable and practical version of the device, the processing can be done real time locally by the SoC. Different levels of activity have been identified manually and various features of Doppler radar signal for different types of activity were explored. It would be very beneficial if a classification algorithm would be developed that can autonomously classify activity level based on the extracted features of the signal. Stand-alone and single-input multiple-output occupancy detectors were explored for occupancy detection and direction of arrival estimation. It will be very interesting to access a network of sensors and using multiple-input multiple-output technologies. It could be tested in a real setting such as an office or an apartment.

Principle component analysis for linear demodulation and arctangent demodulation for nonlinear demodulation are used throughout this work. There are pros and cons associated with each method. However, limitations and accuracies of these methods still need investigation. The main advantages of nonlinear demodulation over linear is the ability to measure absolute displacement. However, this method seems more susceptible to noise than the linear method. A thorough analysis and performance comparison between these methods and the demodulation outcome can be studied by changing key factors such as arc length, coupling, noise level, initial position, and demodulation stage, can help develop a better understanding of the limitations and benefits of these methods and choosing the best technique for any given problem.

8. REFERENCES

[1] O. Steichen, G. Grateau, and E. Bouvard, "Respiratory rate: the neglected vital sign," *Med J Aust*, vol. 189, pp. 531-2, Nov 3 2008.

[2] W. Massagram, V. M. Lubecke, A. Host-Madsen, and O. Boric-Lubecke, "Assessment of heart rate variability and respiratory sinus arrhythmia via Doppler radar," *Microwave Theory and Techniques, IEEE Transactions on*, vol. 57, pp. 2542-2549, 2009.

[3] C. NHLBI Fact Book, "4, Disease Statistics, NHLBI, NIH," *Available at: ww w. nhlbi. nih. gov/about/factbook/chapter4. htm*, 2012.

[4] C. Li, J. Lin, and Y. Xiao, "Robust overnight monitoring of human vital signs by a non-contact respiration and heartbeat detector," in *Engineering in Medicine and Biology Society, 2006. EMBS'06. 28th Annual International Conference of the IEEE*, 2006, pp. 2235-2238.

[5] A. Singh, M. Baboli, X. Gao, E. Yavari, B. Padasdao, B. Soll, *et al.*, "Considerations for integration of a physiological radar monitoring system with gold standard clinical sleep monitoring systems," in *Engineering in Medicine and Biology Society (EMBC), 2013 35th Annual International Conference of the IEEE*, 2013, pp. 2120-2123.

[6] O. Boric-Lubecke, X. Gao, E. Yavari, M. Baboli, A. Singh, and V. M. Lubecke, "E-healthcare: Remote monitoring, privacy, and security," in *Microwave Symposium (IMS), 2014 IEEE MTT-S International*, 2014, pp. 1-3.

[7] O. Boric-Lubeke and V. M. Lubecke, "Wireless house calls: using communications technology for health care and monitoring," *Microwave Magazine, IEEE,* vol. 3, pp. 43-48, 2002.

[8] N. Hafner, I. Mostafanezhad, V. M. Lubecke, O. Boric-Lubecke, and A. Host-Madsen, "Non-contact cardiopulmonary sensing with a baby monitor," in *Conference proceedings:... Annual International Conference of the IEEE Engineering in Medicine and Biology Society. IEEE Engineering in Medicine and Biology Society. Conference*, 2006, pp. 2300-2302.

[9] C. Li, C. Gu, R. Li, and S. B. Jiang, "Radar motion sensing for accurate tumor tracking in radiation therapy," in *Wireless and Microwave Technology Conference (WAMICON), 2011 IEEE 12th Annual*, 2011, pp. 1-6.

[10] V. M. Lubecke, O. Boric-Lubecke, A. Host-Madsen, and A. E. Fathy, "Through-the-wall radar life detection and monitoring," in *Microwave Symposium, 2007. IEEE/MTT-S International*, 2007, pp. 769-772.

[11] E. Yavari, H. Jou, V. Lubecke, and O. Boric-Lubecke, "Doppler radar sensor for occupancy monitoring," in *Biomedical Wireless Technologies, Networks, and Sensing Systems (BioWireleSS), 2013 IEEE Topical Conference on*, 2013, pp. 139-141.

[12] E. Yavari, C. Song, V. Lubecke, and O. Boric-Lubecke, "Is There Anybody in There?: Intelligent Radar Occupancy Sensors," *Microwave Magazine, IEEE*, vol. 15, pp. 57-64, 2014.

[13] J. C. Lin, "Noninvasive microwave measurement of respiration," *Proceedings of the IEEE,* vol. 63, pp. 1530-1530, 1975.

[14] J. C. Lin, J. Kiernicki, M. Kiernicki, and P. B. Wollschlaeger, "Microwave apexcardiography," *Microwave Theory and Techniques, IEEE Transactions on*, vol. 27, pp. 618-620, 1979.

[15] A. D. Droitcour, G. T. A. Kovacs, and S. U. D. o. E. Engineering, *Non-contact Measurement of Heart and Respiration Rates with a Single-chip Microwave Doppler Radar*: Stanford University, 2006.

[16] W. Massagram, *A Study of Feasibility in Long-term Cardiopulmonary Monitoring Via Doppler Radar*: University of Hawai'i at Manoa, 2008.

[17] B.-K. Park, *Cardiopulmonary monitoring using Doppler radar*: University of Hawaii at Manoa, 2007.

[18] A. Singh, X. Gao, E. Yavari, M. Zakrzewski, X. H. Cao, V. M. Lubecke, *et al.*, "Data-based quadrature imbalance compensation for a CW Doppler radar system," *Microwave Theory and Techniques, IEEE Transactions on*, vol. 61, pp. 1718-1724, 2013.

[19] E. Yavari, V. Lubecke, and O. Boric-Lubecke, "AC/DC coupling effects on CW and pulse transmission modes in Doppler radar physiological monitoring system," in *Biomedical Wireless Technologies, Networks, and Sensing Systems (BioWireleSS), 2012 IEEE Topical Conference on*, 2012, pp. 25-28.

[20] M. Zakrzewski, A. Singh, E. Yavari, X. Gao, O. Boric-Lubecke, J. Vanhala, *et al.*, "Quadrature Imbalance Compensation With Ellipse-Fitting Methods for Microwave Radar Physiological Sensing," 2014.

[21] W. K. Saunders, "CW and FM radar," *Radar Handbook*, pp. 16-21, 1990.

[22] M. I. Skolnik, *Introduction to radar systems*, 3rd ed. Boston: McGraw Hill, 2001.

[23] S. Kingsley and S. Quegan, *Understanding radar systems*: The Institution of Engineering and Technology, 1999.

[24] R. Adla, N. Al-Holou, M. Murad, and Y. A. Bazzi, "Automotive collision avoidance methodologies Sensor-based and ITS-based," in *Computer Systems and Applications (AICCSA), 2013 ACS International Conference on*, 2013, pp. 1-8.

[25] M. I. Skolnik, "Introduction to radar," *Radar Handbook*, p. 2, 1962.

[26] C. Li, *Doppler phase modulation effect for non-contact accurate measurement of vital signs and other periodic movements-from theory to CMOS system on chip integrations*: University of Florida, 2009.

[27] I. Mostafanezhad, *NOISE REDUCTION TECHNIQUES FOR WIRELESS LIFE SIGNS MONITORING DEVICES*: University of Hawaii at Manoa, 2010.

[28] J. MC Budge and M. Burt, "Range correlation effects on phase and amplitude noise," in *Southeastcon'93, Proceedings., IEEE*, 1993, p. 5 p.

[29] E. L. Christensen, S. N. Madsen, and N. Skou, "Review of the homodyne technique for coherent radar," in *Radar Conference, 1990., Record of the IEEE 1990 International*, 1990, pp. 159-163.

[30] B.-K. Park, S. Yamada, O. Boric-Lubecke, and V. Lubecke, "Single-channel receiver limitations in Doppler radar measurements of periodic motion," in *Radio and Wireless Symposium, 2006 IEEE,* 2006, pp. 99-102.

[31] B.-K. Park, O. Boric-Lubecke, and V. M. Lubecke, "Arctangent demodulation with DC offset compensation in quadrature Doppler radar receiver systems," *Microwave Theory and Techniques, IEEE Transactions on,* vol. 55, pp. 1073-1079, 2007.

[32] C. Li and J. Lin, "Complex signal demodulation and random body movement cancellation techniques for non-contact vital sign detection," in *Microwave Symposium Digest, 2008 IEEE MTT-S International*, 2008, pp. 567-570.

[33] A. M. Vergara, O. Boric-Lubecke, and V. M. Lubecke, "DC information preservation for cardiopulmonary monitor utilizing CW doppler radar," in *Engineering in Medicine and Biology Society, 2008. EMBS 2008. 30th Annual International Conference of the IEEE*, 2008, pp. 1246-1249.

[34] A. D. Droitcour, O. Boric-Lubecke, V. M. Lubecke, J. Lin, and G. T. Kovacs, "Range correlation and I/Q performance benefits in single-chip silicon Doppler radars for noncontact cardiopulmonary monitoring," *Microwave Theory and Techniques, IEEE Transactions on,* vol. 52, pp. 838-848, 2004.

[35] X. Zhao, C. Song, V. Lubecke, and O. Boric-Lubecke, "DC coupled Doppler radar physiological monitor," in *Engineering in Medicine and Biology Society, EMBC, 2011 Annual International Conference of the IEEE,* 2011, pp. 1909-1912.

[36] A. M. Vergara and V. M. Lubecke, "Data acquisition system for Doppler radar vital-sign monitor," in *Conference proceedings:... Annual International Conference of the IEEE Engineering in Medicine and Biology Society. IEEE Engineering in Medicine and Biology Society. Conference*, 2006, pp. 2269-2272.

[37] S. Mirabbasi and K. Martin, "Classical and modern receiver architectures," *Communications Magazine, IEEE,* vol. 38, pp. 132-139, 2000.

[38] H. Vermarien and E. Van Vollenhoven, "The recording of heart vibrations: a problem of vibration measurement on soft tissue," *Medical and Biological Engineering and Computing*, vol. 22, pp. 168-178, 1984.

[39] E. Yavari, C. Song, V. Lubecke, and O. Boric-Lubecke, "System-on-Chip based Doppler radar occupancy sensor," in *Engineering in Medicine and Biology Society, EMBC, 2011 Annual International Conference of the IEEE*, 2011, pp. 1913-1916.

[40] E. Yavari, B. Padasdao, V. Lubecke, and O. Boric-Lubecke, "Packet radar spectrum recovery for physiological signals," in *Engineering in Medicine and Biology Society (EMBC), 2013 35th Annual International Conference of the IEEE*, 2013, pp. 1760-1763.

[41] Y. Xiao, J. Lin, O. Boric-Lubecke, and V. M. Lubecke, "Frequency-tuning technique for remote detection of heartbeat and respiration using low-power double-sideband transmission in the Ka-band," *Microwave Theory and Techniques, IEEE Transactions on*, vol. 54, pp. 2023-2032, 2006.

[42] I. Jolliffe, *Principal component analysis*: Wiley Online Library, 2005.

[43] B.-K. Park, S. Yamada, and V. Lubecke, "Measurement method for imbalance factors in direct-conversion quadrature radar systems," *Microwave and Wireless Components Letters, IEEE*, vol. 17, pp. 403-405, 2007.

[44] A. Høst-Madsen, N. Petrochilos, O. Boric-Lubecke, V. M. Lubecke, B.-K. Park, and Q. Zhou, "Signal processing methods for Doppler radar heart rate monitoring," in *Signal Processing Techniques for Knowledge Extraction and Information Fusion*, ed: Springer, 2008, pp. 121-140.

[45] F. R. Gilliam III, J. P. Singh, C. M. Mullin, M. McGuire, and K. J. Chase, "Prognostic value of heart rate variability footprint and standard deviation of average 5-minute intrinsic RR intervals for mortality in cardiac resynchronization therapy patients," *Journal of electrocardiology*, vol. 40, pp. 336-342, 2007.

[46] M. Hilton, R. Bates, K. Godfrey, M. Chappell, and R. Cayton, "Evaluation of frequency and time-frequency spectral analysis of heart rate variability as a diagnostic marker of the sleep apnoea syndrome," *Medical & biological engineering & computing*, vol. 37, pp. 760-769, 1999.

[47] E. Jovanov, A. O'Donnell Lords, D. Raskovic, P. G. Cox, R. Adhami, and F. Andrasik, "Stress monitoring using a distributed wireless intelligent sensor

system," *Engineering in Medicine and Biology Magazine, IEEE,* vol. 22, pp. 49-55, 2003.

[48] M. Malik, J. T. Bigger, A. J. Camm, R. E. Kleiger, A. Malliani, A. J. Moss, *et al.*, "Heart rate variability standards of measurement, physiological interpretation, and clinical use," *European heart journal,* vol. 17, pp. 354-381, 1996.

[49] R. N. Bracewell and R. Bracewell, *The Fourier transform and its applications* vol. 31999: McGraw-Hill New York, 1986.

[50] B. Lohman, O. Boric-Lubecke, V. Lubecke, P. Ong, and M. Sondhi, "A digital signal processor for Doppler radar sensing of vital signs," *Engineering in Medicine and Biology Magazine, IEEE,* vol. 21, pp. 161-164, 2002.

[51] M. M. Sondhi, "New methods of pitch extraction," *Audio and Electroacoustics, IEEE Transactions on,* vol. 16, pp. 262-266, 1968.

[52] A. A. Abidi, "Direct-conversion radio transceivers for digital communications," *Solid-State Circuits, IEEE Journal of,* vol. 30, pp. 1399-1410, 1995.

[53] B. Razavi, "Design considerations for direct-conversion receivers," *Circuits and Systems II: Analog and Digital Signal Processing, IEEE Transactions on,* vol. 44, pp. 428-435, 1997.

[54] R. Fletcher and J. Han, "Low-cost differential front-end for Doppler radar vital sign monitoring," in *Microwave Symposium Digest, 2009. MTT'09. IEEE MTT-S International*, 2009, pp. 1325-1328.

[55] A. D. Droitcour, O. Boric-Lubecke, V. M. Lubecke, and L. Jenshan, "0.25 /spl mu/m CMOS and BiCMOS single-chip direct-conversion Doppler radars for remote sensing of vital signs," in *Solid-State Circuits Conference, 2002. Digest of Technical Papers. ISSCC. 2002 IEEE International*, 2002, pp. 348-349 vol.1.

[56] X. Yu, C. Li, and J. Lin, "Two-dimensional noncontact vital sign detection using Doppler radar array approach," in *Microwave Symposium Digest (MTT), 2011 IEEE MTT-S International*, 2011, pp. 1-4.

[57] C. Li and J. Lin, "Random body movement cancellation in Doppler radar vital sign detection," *Microwave Theory and Techniques, IEEE Transactions on,* vol. 56, pp. 3143-3152, 2008.

[58] Y. Xiao, J. Lin, O. Boric-Lubecke, and V. M. Lubecke, "A Ka-band low power Doppler radar system for remote detection of cardiopulmonary motion," in *Engineering in Medicine and Biology Society, 2005. IEEE-EMBS 2005. 27th Annual International Conference of the*, 2006, pp. 7151-7154.

[59] O. Boric-Lubecke, V. M. Lubecke, A. Host-Madsen, D. Samardzija, and K. Cheung, "Doppler radar sensing of multiple subjects in single and multiple antenna systems," in *Telecommunications in Modern Satellite, Cable and Broadcasting Services, 2005. 7th International Conference on*, 2005, pp. 7-11.

[60] A. Vergara, N. Petrochilos, O. Boric-Lubecke, A. Host-Madsen, and V. Lubecke, "Blind source separation of human body motion using direct conversion Doppler radar," in *Microwave Symposium Digest, 2008 IEEE MTT-S International*, 2008, pp. 1321-1324.

[61] D. Samardzija, B.-K. Park, O. Boric-Lubecke, V. Lubecke, A. Host-Madsen, and T. Sizer, "Experimental evaluation of multiple antenna techniques for remote sensing of physiological motion," in *Microwave Symposium, 2007. IEEE/MTT-S International*, 2007, pp. 1735-1738.

[62] A. Singh, "Subject isolation and non stationary clutter rejection using RF Backscatter--tag radar," UNIVERSITY OF HAWAI'I AT MANOA, 2012.

[63] Y. Xiao, C. Li, and J. Lin, "Accuracy of a low-power Ka-band non-contact heartbeat detector measured from four sides of a human body," in *Microwave Symposium Digest, 2006. IEEE MTT-S International*, 2006, pp. 1576-1579.

[64] I. Mostafanezhad, O. Boric-Lubecke, and V. Lubecke, "A coherent low IF receiver architecture for Doppler radar motion detector used in life signs monitoring," in *Radio and Wireless Symposium (RWS), 2010 IEEE*, 2010, pp. 571-574.

[65] I. Mostafanezhad and O. Boric-Lubecke, "An RF based analog linear demodulator," *Microwave and Wireless Components Letters, IEEE*, vol. 21, pp. 392-394, 2011.

[66] I. Mostafanezhad, O. Boric-Lubecke, V. Lubecke, and D. Mandic, "Application of empirical mode decomposition in removing fidgeting interference in Doppler radar life signs monitoring devices," in *Engineering in Medicine and Biology*

Society, 2009. EMBC 2009. Annual International Conference of the IEEE, 2009, pp. 340-343.

[67] I. Mostafanezhad, E. Yavari, O. Boric-Lubecke, V. M. Lubecke, and D. P. Mandic, "Cancellation of unwanted doppler radar sensor motion using empirical mode decomposition," *IEEE SENSORS JOURNAL*, vol. 13, p. 1897, 2013.

[68] N. Hafner, J. C. Drazen, and V. M. Lubecke, "Fish heart rate monitoring by body-contact Doppler radar," *Sensors Journal, IEEE*, vol. 13, pp. 408-414, 2013.

[69] A. Singh, N. Hafner, V. Lubecke, and M. Butler, "A data efficient method for characterization of chameleon tongue motion using Doppler radar," in *Engineering in Medicine and Biology Society (EMBC), 2012 Annual International Conference of the IEEE*, 2012, pp. 574-577.

[70] A. Singh, S. S. Lee, M. Butler, and V. Lubecke, "Activity monitoring and motion classification of the lizard Chamaeleo Jacksonii using multiple Doppler radars," in *Engineering in Medicine and Biology Society (EMBC), 2012 Annual International Conference of the IEEE*, 2012, pp. 4525-4528.

[71] G. Assmann, P. Cullen, T. Evers, D. Petzinna, and H. Schulte, "Importance of arterial pulse pressure as a predictor of coronary heart disease risk in PROCAM," *European heart journal*, vol. 26, pp. 2120-2126, 2005.

[72] J. F. Fieselmann, M. S. Hendryx, C. M. Helms, and D. S. Wakefield, "Respiratory rate predicts cardiopulmonary arrest for internal medicine inpatients," *Journal of general internal medicine*, vol. 8, pp. 354-360, 1993.

[73] C. Gu, G. Wang, Y. Li, T. Inoue, and C. Li, "A Hybrid Radar-Camera Sensing System With Phase Compensation for Random Body Movement Cancellation in Doppler Vital Sign Detection," 2013.

[74] C. Li, V. M. Lubecke, O. Boric-Lubecke, and J. Lin, "A review on recent advances in Doppler radar sensors for noncontact healthcare monitoring," *Microwave Theory and Techniques, IEEE Transactions on*, vol. 61, pp. 2046-2060, 2013.

[75] P.-H. Wu, J.-K. Jau, C.-J. Li, T.-S. Horng, and P. Hsu, "Phase-and Self-Injection-Locked Radar for Detecting Vital Signs with Efficient Elimination of DC Offsets

and Null Points," *Microwave Theory and Techniques, IEEE Transactions on,* vol. 61, pp. 685-695, 2013.

[76] Y. Yan, C. Li, and J. Lin, "Effects of I/Q mismatch on measurement of periodic movement using a Doppler radar sensor," in *Radio and Wireless Symposium (RWS), 2010 IEEE,* 2010, pp. 196-199.

[77] J. Wang, X. Wang, Z. Zhu, J. Huangfu, C. Li, and L. Ran, "1-D microwave imaging of human cardiac motion: An ab-initio investigation," *Microwave Theory and Techniques, IEEE Transactions on,* vol. 61, pp. 2101-2107, 2013.

[78] S. H. Chang, H. S. Chung, and K. Kim, "Impact of quadrature imbalance in optical coherent QPSK receiver," *Photonics Technology Letters, IEEE,* vol. 21, pp. 709-711, 2009.

[79] R. Umstattd, "Operating and evaluating quadrature modulators for personal communication systems," *Nat. Semicond., Santa Clara, CA, USA, Appl. Note,* vol. 899, 1993.

[80] M. Valkama, M. Renfors, and V. Koivunen, "Advanced methods for I/Q imbalance compensation in communication receivers," *Signal Processing, IEEE Transactions on,* vol. 49, pp. 2335-2344, 2001.

[81] J. E. Kiriazi, O. Boric-Lubecke, and V. M. Lubecke, "Dual-frequency technique for assessment of cardiopulmonary effective RCS and displacement," *Sensors Journal, IEEE,* vol. 12, pp. 574-582, 2012.

[82] D. R. Morgan and M. G. Zierdt, "Novel signal processing techniques for Doppler radar cardiopulmonary sensing," *Signal Processing,* vol. 89, pp. 45-66, 2009.

[83] M. Zakrzewski, H. Raittinen, and J. Vanhala, "Comparison of center estimation algorithms for heart and respiration monitoring with microwave Doppler radar," *Sensors Journal, IEEE,* vol. 12, pp. 627-634, 2012.

[84] X. Gao, A. Singh, E. Yavari, V. Lubecke, and O. Boric-Lubecke, "Non-contact displacement estimation using Doppler radar," in *Engineering in Medicine and Biology Society (EMBC), 2012 Annual International Conference of the IEEE,* 2012, pp. 1602-1605.

[85] N. Chernov and H. Ma, "Least squares fitting of quadratic curves and surfaces," *Computer Vision,* pp. 285-302, 2011.

[86] C. R. Rojas, P. Zetterberg, and P. Handel, "Transceiver inphase/quadrature imbalance, ellipse fitting, and the universal software radio peripheral," *Instrumentation and Measurement, IEEE Transactions on,* vol. 60, pp. 3629-3639, 2011.

[87] N. Chernov and C. Lesort, "Least squares fitting of circles," *Journal of Mathematical Imaging and Vision,* vol. 23, pp. 239-252, 2005.

[88] Z. Zhang, "Parameter estimation techniques: A tutorial with application to conic fitting," *Image and vision Computing,* vol. 15, pp. 59-76, 1997.

[89] G. Strang, "Introduction to linear algebra," *Cambridge Publication,* 2003.

[90] R. R. Fletcher and S. Kulkarni, "Clip-on wireless wearable microwave sensor for ambulatory cardiac monitoring," in *Engineering in Medicine and Biology Society (EMBC), 2010 Annual International Conference of the IEEE*, 2010, pp. 365-369.

[91] L. Lu, C. Li, and D. Y. Lie, "Experimental demonstration of noncontact pulse wave velocity monitoring using multiple Doppler radar sensors," in *Engineering in Medicine and Biology Society (EMBC), 2010 Annual International Conference of the IEEE*, 2010, pp. 5010-5013.

[92] Q. Zhou, J. Liu, A. Host-Madsen, O. Boric-Lubecke, and V. Lubecke, "Detection of multiple heartbeats using Doppler radar," in *Acoustics, Speech and Signal Processing, 2006. ICASSP 2006 Proceedings. 2006 IEEE International Conference on*, 2006, pp. II-II.

[93] R. Wilson, "" The Great Debate: SOC vs. SIP," *EE Times,* vol. 3, 2005.

[94] T. Instruments, "CC253x System-on-chip Solution for 2.4 GHz IEEE 802.15. 4 and Zigbee Applications User's Guid," ed.

[95] Single-axis series: Smart solutions for 1-axi applications Galil [Online]. Available: http://www.galilmc.com/catalog/cat3310.pdf

[96] Y. Denda, T. Nishiura, H. Kawahara, and T. Irino, "Speech recognition with wavelet spectral subtraction in real noisy environment," in *Signal Processing, 2004. Proceedings. ICSP'04. 2004 7th International Conference on*, 2004, pp. 638-641.

[97] *Kai Spot*. Available: http://kaimedical.com/en2/products.php

[98] I. Mostafanezhad, O. Boric-Lubecke, V. Lubecke, and A. Host-Madsen, "Cancellation of unwanted motion in a handheld Doppler radar used for non-contact life sign monitoring," in *Microwave Symposium Digest, 2008 IEEE MTT-S International*, 2008, pp. 1171-1174.

[99] D. Zhu, X. Dong, and W. Lin, "Pulse compression with very low sidelobes in a spaceborne weather radar," in *Geoscience and Remote Sensing Symposium, 2008. IGARSS 2008. IEEE International*, 2008, pp. V-252-V-255.

[100] S. Yamada, O. Boric-Lubecke, and V. M. Lubecke, "Cancellation techniques for LO leakage and dc offset in direct conversion systems," in *Microwave Symposium Digest, 2008 IEEE MTT-S International*, 2008, pp. 1191-1194.

[101] I. Mostafanezhad and O. Boric-Lubecke, "Benefits of Coherent Low-IF for Vital Signs Monitoring Using Doppler Radar," *IEEE Trans. on Microw. Theory Tech.*, Submitted 2014.

[102] E. Yavari and O. Boric-Lubecke, "Low IF demodulation for physiological pulse Doppler radar," in *Microwave Symposium (IMS), 2014 IEEE MTT-S International*, 2014, pp. 1-3.

[103] X. Guo, D. Tiller, G. Henze, and C. Waters, "The performance of occupancy-based lighting control systems: A review," *Lighting Research and Technology*, vol. 42, pp. 415-431, 2010.

[104] A. Alva, K. Shailesh, and S. Tanuja, "Design and implementation of video based occupancy sensing for adaptive lighting applications," in *Emerging Trends in Electrical Engineering and Energy Management (ICETEEEM), 2012 International Conference on*, 2012, pp. 478-482.

[105] K. Weekly, D. Rim, L. Zhang, A. M. Bayen, W. W. Nazaroff, and C. J. Spanos, "Low-cost coarse airborne particulate matter sensing for indoor occupancy detection," in *Automation Science and Engineering (CASE), 2013 IEEE International Conference on*, 2013, pp. 32-37.

[106] W. Butler, P. Poitevin, and J. Bjomholt, "Benefits of wide area intrusion detection systems using FMCW radar," in *Security Technology, 2007 41st Annual IEEE International Carnahan Conference on*, 2007, pp. 176-182.

[107] Y. Yang and A. E. Fathy, "Development and implementation of a real-time see-through-wall radar system based on FPGA," *Geoscience and Remote Sensing, IEEE Transactions on*, vol. 47, pp. 1270-1280, 2009.

[108] T. Yardibi, P. Cuddihy, S. Genc, C. Bufi, M. Skubic, M. Rantz, *et al.*, "Gait characterization via pulse-Doppler radar," in *Pervasive Computing and Communications Workshops (PERCOM Workshops), 2011 IEEE International Conference on*, 2011, pp. 662-667.

[109] M. R. Mahfouz, C. Zhang, B. C. Merkl, M. J. Kuhn, and A. E. Fathy, "Investigation of high-accuracy indoor 3-D positioning using UWB technology," *Microwave Theory and Techniques, IEEE Transactions on*, vol. 56, pp. 1316-1330, 2008.

[110] V. Garg and N. Bansal, "Smart occupancy sensors to reduce energy consumption," *Energy and Buildings*, vol. 32, pp. 81-87, 2000.

[111] H. J. Keller, "30 Years of Passive Infrared Motion Detectors-a Technology Review."

[112] Annual Energy Outlook 2011 with Projections to 2035 [Online]. Available: http://www.eia.gov/forecasts/aeo/pdf/0383er(2011).pdf

[113] Energy Smart Tips for Hotels [Online]. Available: http://smartenergy.arch.uiuc.edu/pdf/Hotel%20Niche%20Market%20Report.pdf

[114] J. P. Steiner. XCT Technology from Lutron: The New Standard in Sensing [Online].

[115] M. Levy and C. Promotions. Low-cost occupancy sensor saves energy [Online]. Available: http://www.atmel.com/dyn/resources/prod_documents/mega88_3_04.pdf

[116] P. Zappi, E. Farella, and L. Benini, "Enhancing the spatial resolution of presence detection in a PIR based wireless surveillance network," in *Advanced Video and Signal Based Surveillance, 2007. AVSS 2007. IEEE Conference on*, 2007, pp. 295-300.

[117] N. Petrochilos, M. Rezk, A. Host-Madsen, V. Lubecke, and O. Boric-Lubecke, "Blind separation of human heartbeats and breathing by the use of a doppler radar

remote sensing," in *Acoustics, Speech and Signal Processing, 2007. ICASSP 2007. IEEE International Conference on*, 2007, pp. I-333-I-336.

[118] K. A. Gotsis, K. Siakavara, and J. N. Sahalos, "On the direction of arrival (DoA) estimation for a switched-beam antenna system using neural networks," *Antennas and Propagation, IEEE Transactions on*, vol. 57, pp. 1399-1411, 2009.

[119] A. Lin and L. Hao, "Doppler and direction-of-arrival (DDOA) radar for multiple-mover sensing," *Aerospace and Electronic Systems, IEEE Transactions on*, vol. 43, pp. 1496-1509, 2007.

[120] S. Chandran, *Advances in Direction-of-arrival Estimation*: Artech House, 2005.